

POLITECNICO DI TORINO

Master's Degree in AUTOMOTIVE ENGINEERING



Master's Degree Thesis

Electrochemical-thermal Analysis of High Capacity Li-ion Pouch Cell for Automotive Applications

Supervisor

Prof. Massimo SANTARELLI

Candidate

Luigi SACCHETTI S263239

October 2020

Abstract

Latest regulatory trends implemented in order to limit emissions combined with research advances in alternative fuels have paved the road toward vehicle electrification. Major original equipment manufacturers (OEMs) have already marketed electric vehicles in large scale but apart from business strategies and policies, the real engineering problems must be addressed. Lithium-ion batteries are a promising technology for energy storage; however, their low energy density and complex electro-chemical nature, compared to fossil fuels, presents additional challenges. Their complex nature and strong temperature dependence during operation must be studied with additional accuracy, capable to predict their behavior. In this research, a pseudo two dimensional (P2D) electro-chemical model, coupled with a 3D thermal energy balance for a recent high capacity NMC pouch cell for automotive applications is developed. The electrochemical model with its temperature dependent parameters is validated at different temperatures and various discharge C-rates to accurately replicate the battery cell operational conditions. The sources of heat are distinguished and characterized via advanced electrochemical-modelling approach, in various battery operations and different thermal boundary conditions. For example, it was determined that the temperature rise during discharge at high C-rates, under natural convection, could result in thermal runaway, if managed incorrectly. Ohmic heat generation of current collectors and cell tabs is investigated and included. Hence, the thermal analysis provides insights on the current and voltage profiles causing the minimum thermal stress on the cell and the location of heat generation spatially and temporally during the battery discharge. Different modelling approximation of the cell are studied starting from the cell fundamental unit. This provides effective design considerations for the battery thermal management system (BTMS) to enhance performance, cycle life and safety of future electrified vehicle energy storage systems.

Dedication

To my family who constantly helps me over time and to my dearest friends....

Acknowledgements

This work represents the peak of my entire academic path and life experience. Thanks to this project, this year has been the greatest game changer of my life, full of emotions, challenges and pride. I cannot say it was easy, especially in the second half of the year. However, this experience made me grow personally and academically, projecting me into the career world. All of this was possible thanks to the collaboration and kindness of the people I met. I am honored to have been part of this program and I sincerely hope to have transmitted my enthusiasm and dedication to the people who I worked with, meeting their expectations. Thanks to FCA, University of Windsor and Politecnico di Torino that made this experience possible.

I would like show my enormous gratitude to my academic advisor at University of Windsor, Dr. Ofelia A. Jianu. First of all for the personal support in all the situations during this year with courses and thesis. Then, for the constant guidance with passion and strength during my thesis development. Thanks to you, I understood the meaning of real academic research in all its aspects: presentations, technical writing and problem solving approaches. I have professionally enriched my skills, being proud of my work and of the possibility to have developed it under your guidance. As part of Dr. Jianu's research team, I would like to express my huge tanks to Gian Favero who helped me with the software simulations as well as with my English writing. I hope I have transmitted some good advice and experience to you and I am looking forward to meet you in Italy one day.

I want to thank my academic advisor at Politecnico di Torino Dr. Massimo Santarelli along with Domenico Ferrero for their help with my project despite the distance.

Many thanks to my FCA US technical advisors from CTC, Dr. Abdulah-Al Mamun and Dr. Yang Liang and the battery research team managed by Dr. Srihari

Gangaraj who gave me the possibility to present my work. Abdulah-Al, You helped me understanding the battery electrochemical and thermal modelling with patience, to accomplish the goals of my project.

I would like to thank Eng. Massimo Buscema, of FCA EMEA from CRF for your help introducing me to the world of battery modelling and constantly helping me technically and personally during this year.

Special thanks to all the academic supervisors of this project, Dr. Giovanni Belingardi, Dr. Maria Pia Cavatorta, from Politecnico who assisted us constantly during the unfortunate situation of the second half of the year. Thanks Dr. Jennifer Johrendt as well as FCA supervisors, Eng. Edoardo Rabino and Eng. Marie Mills for the great opportunity offered to me and their support during the whole program. Thank you Dr. Antonio Mancina for the inspiring tanks that we had during the year.

I would like to acknowledge my committee members, Dr. Balasingam and Dr. Stoilov, for your precious pieces of advice and contributions while reviewing my work.

I would like to enormously thank my beloved family Claudio, Enza and Michele who constantly supported me, especially during the tough lockdown period. The person that I am today is the result of your brilliant work and I hope that I made you proud of me. Thank from my heart to my girlfriend Maddalena who suffered my continuous complaints during this year and encouraged me. I can't wait to see you again. Thanks to my grandparents Rosa, Ermanno with Lo Zio Alberto who always root for me; thanks to Luigi and Angela who protect me from up there.

Thanks to my travel mates Giulio and Filippo, but special thanks to Niccolo', with whom a unique friendship was born, built sharing joys and sorrows far from home. I am very disappointed that the adventure is already over since I enjoyed every instant of it.

Thanks to Mike, Pamela, Marco, Palak, Nupur, Stefano, Paolo, Paschal, Tina, Madie, Matt, Emma, Ryan and Adam for warmly welcoming me to Canada. I am glad for having spent time with you. Zac, Huan, Yhiong thanks for sharing this year of adventures in the DIMD program as well as outside it. I am looking forward to see all of you in Italy to show your beautiful country.

Table of Contents

Declaration of Originality	III
Abstract	IV
Dedication	V
Acknowledgements	VI
List of Tables	XI
List of Figures	XV
List of Abbreviations	XV
Nomenclature	XIX
1 Introduction	1
1.1 Background and Motivation	1
1.1.1 Li-ion Batteries For Automotive Applications	4
1.2 Objective and Contributions	4
1.3 Thesis Outline	7
2 Literature Review	9
2.1 Li-ion Batteries Fundamentals	9
2.2 Reasons for Battery Modelling and Thermal Management	16
2.3 The Output of Battery Modelling: Battery Management and Thermal Management	22
2.4 Battery Modelling Approaches	32
2.4.1 Equivalent Circuit Models (ECM)	33
2.4.2 Electrochemical (EC) Models	35

2.4.3	Thermal and Heat Generation Coupling	38
3	Analytical Model	45
3.1	P2D Electrochemical Model	45
3.1.1	Mass Conservation in Solid Electrode	47
3.1.2	Mass Conservation in Liquid Electrolyte	49
3.1.3	Charge Conservation in Solid Electrode	51
3.1.4	Charge Conservation in Liquid Electrolyte	52
3.1.5	Charge Transfer Reaction and Thermodynamics Connect . . .	53
3.2	3D Distributed Thermal Model	55
3.3	Electrochemical-Thermal (ECT) Coupling	59
4	Parametrization and Model implementation in COMSOL Multiphysics[®]	62
4.1	Cell Materials	63
4.2	Electrode Balancing	63
4.3	Physio-Chemical Properties	67
4.4	Temperature Dependent Properties	68
4.5	Pouch Cell Thermal Parameters Estimation	72
4.6	P2D Electrochemical Modelling Details in COMSOL Multiphysics [®] .	75
4.7	Thermal Model Implementation and Details in COMSOL Multiphysics [®]	79
4.8	Coupling Strategy in COMSOL Multiphysics [®]	83
5	EC Model Validation and Results Discussion	86
6	ECT Model Application Results Analysis and Discussion	91
6.1	Single Layer Results and Full 3D ECT Model Comparison	91
6.2	Complete Cell Models Results	96
6.2.1	Case A: Nominal Discharge C-rate and Natural Convection . .	98
6.2.2	Case B: Fast Discharge C-rate and Natural Convection	99
6.2.3	Case C: Nominal Discharge C-rate and Forced Convection . .	101
6.2.4	Case D: Fast Discharge C-rate and Forced Convection	105
6.3	Overall Comparison and BTMS Recommendations	107
7	Concluding Remarks and Future Work	119
7.1	Summary and Conclusions	119
7.2	Future Work	121

Bibliography	137
Appendix A Required Parameters For The COMSOL Multiphysics®	
Electrochemical-thermal Model	138
A.1 Model Global Parameters	138
A.2 Local Variables of <i>Component one</i>	144
A.3 Local Variables of <i>Component two</i>	146
Vita Auctoris	148

List of Tables

4.1	Thermal Properties of Different Layers	74
4.2	Pouch Cell Thermal Properties	74
5.1	EC model voltage maximum percentage errors	89
5.2	EC model voltage RMSEs	89
6.1	ECT models integral of volumetric heat sources comparison	93
A.1	Model Parameters	138
A.2	Local Variables of <i>Component one</i>	145
A.3	Local Variables of <i>Component two</i>	146

List of Figures

1.1	Volumetric energy density of transport fuels	2
1.2	Ragone plot of specific power density vs. specific energy density of various electrochemical energy storage devices. Source: [1]	3
1.3	Panasonic NCR18650B cylindrical battery cell. Source: [2]	5
1.4	Panasonic prismatic Li-ion battery for PHEVs. Source: [3]	5
1.5	A123 Systems pouch cell. Source: [4]	5
1.6	Scheme of Tesla Model S 85 battery pack. Source: [5]	6
2.1	Architecture of a typical Li-ion battery cell. Source [6]	10
2.2	Jellyroll disposition for various formats of Lithium battery cells: cylindrical [a], coin [b], prismatic [c], pouch [d]. Source: [7]	11
2.3	LCO crystalline structure. Source: [8]	12
2.4	LCO web diagram. Source: [8]	12
2.5	LMO spinel crystalline structure. Source: [8]	12
2.6	LMO web diagram. Source: [8]	12
2.7	LFP olivine crystalline structure. Source: [9]	13
2.8	LFP web diagram. Source: [8]	13
2.9	NMC crystalline structure. Source: [10]	13
2.10	NMC web diagram. Source: [8]	13
2.11	Graphite crystalline structure and SEI. Source: [11]	14
2.12	LTO crystalline structure. Source: [12]	15
2.13	LTO web diagram. Source: [8]	15
2.14	Optimal temperature range for Li-ion batteries. Source: [13]	22
2.15	Summary of temperature ranges for Li-ion Batteries. Source: [14]	22
2.16	Centralized battery management system structure. Source: [14]	24
2.17	Distributed battery management system structure. Source: [14]	24
2.18	PCM enhanced battery pack. Source: [15]	27
2.19	Toyota Prius battery pack forced air cooling system. Source: [16]	28

2.20	Airflow in a battery pack: a)Series airflow b)Parallel airflow. Source: [17]	28
2.21	Liquid refrigerant cooling system and coolant cooling system. Source: [18]	30
2.22	Tesla Model S battery pack tear-down. Source: [19]	31
2.23	GM Volt inter-cell battery cooling plate. Source: [20]	31
2.24	Heat pipe working scheme. Source: [21]	31
2.25	Heat pipe application for HEV battery pack cooling. Source: [22] . .	31
2.26	Multi-scale physics and micro-macroscopic modelling approach applied into a lithium-ion battery. Source: [23]	33
2.27	Conceptual approach to Li-ion battery thermal analysis	33
2.28	Li-ion battery common models scale comparison. Source: [24]	33
2.29	ECM against EC models comparison	36
2.30	P2D model dimensions. Source: [25]	37
2.31	Model domain scheme: a) P2D model, b) SP model. Source: [26] . .	38
2.32	Electrochemical-thermal coupling scheme. Source [27]	41
2.33	2D charge balance model scheme. Source: [28]	42
2.34	One of proposed electrochemical-thermal coupling possibilities. Source: [29]	43
3.1	P2D electrochemical model geometry scheme, adapted from [30] . . .	46
3.2	Coupling scheme and enabling quantities between the modeling dimensions	61
4.1	Electrode balancing equilibrium voltage curves for the cell under study	65
4.2	SOL of electrodes during discharge for the cell under study	65
4.3	Entropy coefficients of electrodes	72
4.4	Cell multidimensional scheme. Adapted from [31]	76
4.5	<i>Component one</i> model builder and geometry in COMSOL Multiphysics®	78
4.6	EC boundary conditions for the 1D cell model in COMSOL Multiphysics®	79
4.7	<i>Component two</i> model builder and geometry in COMSOL Multiphysics®	80
4.8	3D model of the fundamental unit geometry in COMSOL®	81
4.9	3D model of the complete cell with average heat strategy in COMSOL®	81
4.10	3D complete cell model with all the layers repetition in COMSOL Multiphysics®: a) Scale=100 on y axis b) No scale	82

5.1	Isothermal cell voltage during constant current discharge at different C-rates	87
5.2	Isothermal cell SOC during constant current discharge at different C-rates	88
6.1	Full 3D ECT model of one layer in COMSOL [®] with Scale=100 on y axis	92
6.2	Domains heat sources comparison over time under nominal current and $h = 7 [W/(m^2K)]$	92
6.3	Full 3D model current streamlines in the cell	95
6.4	Full 3D model uneven Ohmic heat generation in the positive CC domain	95
6.5	Heat sources characterization over time under nominal current and $h = 7 [W/(m^2K)]$	96
6.6	Domains heat sources and classification over time under fast discharge and $h = 7 [W/(m^2K)]$	97
6.7	Temperature sensors positioning in the cell geometry	97
6.8	Temperature sensors readings through discharge at nominal C-rate and $h = 7 [W/(m^2K)]$	98
6.9	Layered cell model tab top view	100
6.10	Central plane temperature distribution, in the cell with average heat source, during discharge at nominal C-rate and $h = 7 [W/(m^2K)]$. .	101
6.11	Central plane temperature distribution, in the cell with repeated layers, during discharge at nominal C-rate and $h = 7 [W/(m^2K)]$	102
6.12	Surface temperature distribution, in the cell with average heat source, under discharge at nominal C-rate and $h = 7 [W/(m^2K)]$	103
6.13	Surface temperature distribution, in the cell with repeated layers, under discharge at nominal C-rate and $h = 7 [W/(m^2K)]$	104
6.14	Temperature sensors readings through fast discharge and $h = 7 [W/(m^2K)]$	105
6.15	Central plane temperature distribution, in the cell with average heat source, during fast discharge and $h = 7 [W/(m^2K)]$	106
6.16	Central plane temperature distribution, in the cell with repeated layers, during fast discharge and $h = 7 [W/(m^2K)]$	107
6.17	Surface temperature distribution, in the cell with average heat source, under fast discharge and $h = 7 [W/(m^2K)]$	108
6.18	Surface temperature distribution, in the cell with repeated layers, under fast discharge and $h = 7 [W/(m^2K)]$	109

6.19	Temperature sensors readings through discharge at nominal C-rate and $h = 25 [W/(m^2K)]$	110
6.20	Central plane temperature distribution, in the cell with average heat source, during discharge at nominal C-rate and $h = 25 [W/(m^2K)]$. .	111
6.21	Central plane temperature distribution, in the cell with repeated layers, during discharge at nominal C-rate and $h = 25 [W/(m^2K)]$	112
6.22	Surface temperature distribution, in the cell with average heat source, under discharge at nominal C-rate and $h = 25 [W/(m^2K)]$	113
6.23	Surface temperature distribution, in the cell with repeated layers, under discharge at nominal C-rate and $h = 25 [W/(m^2K)]$	114
6.24	Temperature sensors readings through fast discharge and $h = 25 [W/(m^2K)]$	114
6.25	Central plane temperature distribution, in the cell with average heat source, during fast discharge and $h = 25 [W/(m^2K)]$	115
6.26	Central plane temperature distribution, in the cell with repeated layers, during fast discharge and $h = 25 [W/(m^2K)]$	116
6.27	Surface temperature distribution, in the cell with average heat source, under fast discharge and $h = 25 [W/(m^2K)]$	117
6.28	Surface temperature distribution, in the cell with repeated layers, under fast discharge and $h = 25 [W/(m^2K)]$	118
6.29	Average cell temperature comparison between the four cases and two models	118

Abbreviations

BEV Battery Electric Vehicle. 2, 4, 11, 17, 19, 22, 25, 28, 30, 35

BMS Battery Management System. 22–24, 34

BTMS Battery Thermal Management System. IV, IX, 3, 6, 7, 19, 21, 22, 25, 28, 34, 38, 86, 107, 110, 113, 120, 121

CAN Controller Area Network. 22

CNT Carbon Nano-tubes. 26

DFN Doyle, Fuller and Newman Model, synonym of P2D. 36, 45, 77

EC Electrochemical. VIII, IX, XI, XIII, 32, 35, 36, 42, 63, 70, 77, 79, 85, 86, 89, 93

ECM Equivalent Circuit Model. VIII, XIII, 32–37

ECT Electrochemical-Thermal. IX, XI, XIV, 7, 8, 16, 59, 76, 80, 86, 91–93, 95, 119, 121

ECU Electronic Control Unit. 23

EMC Ethyl Methyl Carbonate. 47, 63, 70

ESP Extended Single Particle Model. 37

EV Electric Vehicle. 30, 108, 121, 125, 127, 131

FCA Fiat Chrysler Automobiles. VI

FEA Finite Element Analysis. 5, 41, 62

FLT First Law of Thermodynamics. 40

GITT Galvanostatic Intermittent Titration Technique. 67

HEV Hybrid Electric Vehicle. XIII, 4, 11, 17, 19, 22, 23, 25, 28–31, 125, 127, 131

HVAC Heating Ventilation and Air Conditioning. 32

ICE Internal Combustion Engine. 1

ISP Improved Single Particle Model. 37

KMC Kinetic Monte Carlo. 33

LCO Lithium Cobalt Oxide. XII, 10–12, 17, 43

LFP Lithium Iron Phosphate. XII, 4, 5, 11, 13, 20, 43

LMO Lithium Manganese Oxide. 10, 43

LTO Lithium Titanate Oxide. 14

NCA Nickel Cobalt Aluminum. 12, 43, 44

Ni-Mh Nickel Metal-hydride. 28

NMC Nickel Cobalt Manganese. IV, XII, 5, 6, 11–13, 21, 44, 47, 58, 62–64, 67, 71, 74, 90, 119, 121, 135, 136

OCP Open Circuit Potential, synonym of OCV. 10, 40, 53, 60, 67, 71, 120

OCV Open Circuit Voltage. 1, 34, 63–65, 67

ODE Ordinary Differential Equation. 35

OEM Original Equipment Manufacturer. IV, 4, 7, 16, 19, 21, 62, 86, 119

P2D Pseudo-two-dimensional Model. IV, IX, XIII, 5, 7, 35–38, 40, 42–46, 56, 59, 62, 67, 75–77, 89–91, 93, 119

PC Propylene Carbonate. 63, 70

PCB Printed Circuit Board. 22, 24

PCM Phase Change Material. 26, 27

PDAE Partial Derivative Differential Algebraic Equation. 37

PDE Partial Derivative Differential Equation. 35, 47

PHEV Plug-in Hybrid Electric Vehicle. XII, 5, 18, 30, 123, 129

PNGV Partnership for New Generation of Vehicles. 34

PP Porous Electrode with Polynomial Approximation Model. 38

PSD Particle Size Distribution. 90

PTC Positive Temperature Control. 32

RC Resistance Capacitance. 34

RMSE Root Mean Square Error. XI, 87–89, 120

SEI Solid Electrolyte Interphase. XII, 13–15, 17, 18, 20, 33, 41, 64, 66, 90, 135

SOC State of Charge. XIV, 2, 17, 18, 20, 23–25, 34, 40, 64, 69, 77, 79, 86, 88–90, 120, 122, 141, 145

SOH State of Health. 23

SOL State of Lithiation. XIII, 64–66

SP Single Particle Model. XIII, 37, 38

Nomenclature

A_{cell}	$[m^2]$	Cell active material cross-section
$a_{s,i}$	$[1/m]$	Specific surface area per unit volume
b	$[-]$	Bruggeman factor or exponent
c_l	$[mol/m^3]$	Li concentration in liquid phase
c_P	$[mol/m^3]$	Li concentration in reaction products
$C_{p,cell}$	$[J/(kgK)]$	Cell heat capacity
$C_{p,neg}$	$[J/(kgK)]$	Negative electrode heat capacity
$C_{p,neg,cc}$	$[J/(kgK)]$	Negative current collector heat capacity
$C_{p,pos}$	$[J/(kgK)]$	Positive electrode heat capacity
$C_{p,pos,cc}$	$[J/(kgK)]$	Positive current collector heat capacity

Continued on next page

$C_{p,sep}$	$[J/(kgK)]$	Separator electrode heat capacity
c_R	$[mol/m^3]$	Li concentration in reaction reactants
c_{ref}	$[mol/m^3]$	Li reference concentration
$c_{s,i}$	$[mol/m^3]$	Li concentration in solid phase
$c_{s,max,i}$	$[mol/m^3]$	Maximum Li concentration in solid phase
$c_{s,0,i}$	$[mol/m^3]$	Initial Li concentration in solid phase
$D_{l,0}$	$[m^2/s]$	Li liquid phase diffusion coefficient at reference temperature
D_l	$[m^2/s]$	Electrolyte diffusivity
$D_{s,0,i}$	$[m^2/s]$	Li solid phase diffusion coefficient at reference temperature
$D_{s,i}$	$[m^2/s]$	Li solid phase diffusion coefficient
$E_{act,i}$	$[J/mol]$	Specific parameter activation energy
$E_{cell,exp}$	$[V]$	Experimental cell equilibrium voltage

Continued on next page

$E_{cell,model}$	[V]	Modeled cell equilibrium voltage
$E_{eq,i}$	[V]	Electrode equilibrium voltage
F	[C/mol]	Faraday constant
f_{excess}	[—]	Initial Li lost capacity
f_i	[—]	Mean molar activity coefficient
f_{loss}	[—]	Excess Li capacity
G	[J]	Gibbs energy
H	[J]	Enthalpy
h	[W/(m ² · K)]	Heat transfer coefficient
h_{tab}	[m]	Tab height
$\Delta H_{\alpha\beta}$	[J]	Equivalent phase change enthalpy
i_a	[A/m ²]	Anodic current density
i_{app}	[A]	Total cell applied current
i_c	[A/m ²]	Cathodic current density
i_l	[A/m ²]	Liquid phase current density
$i_{s,i}$	[A/m ²]	Solid phase current density
j_i	[mol/m ² · s]	Pore wall mass flux

Continued on next page

$K_{0,i}$	$[m/s]$	Reaction rate constant at reference temperature
K_a K_{neg}	$[m/s]$	Anodic reaction rate constant
k_B	$[J/K]$	Boltzmann constant
K_c K_{pos}	$[m/s]$	Cathodic reaction rate constant
k_{cell}	$[W/m \cdot K]$	Cell thermal conductivity
$k_{cell,\parallel}$	$[W/m \cdot K]$	In-plane cell thermal conductivity
$k_{cell,\perp}$	$[W/m \cdot K]$	Through-plane cell thermal conductivity
k_{neg}	$[W/m \cdot K]$	Negative electrode thermal conductivity
$k_{neg,cc}$	$[W/m \cdot K]$	Negative current collector thermal conductivity
k_{pos}	$[W/m \cdot K]$	Positive electrode thermal conductivity
$k_{pos,cc}$	$[W/m \cdot K]$	Positive current collector thermal conductivity
k_{sep}	$[W/m \cdot K]$	Separator thermal conductivity
l	$[m]$	Characteristic dimension
L_{cell}	$[m]$	Fundamental unit cell thickness

L_{neg}	$[m]$	Negative electrode thickness
$L_{neg,cc}$	$[m]$	Negative current collector thickness
L_{pos}	$[m]$	Positive electrode thickness
$L_{pos,cc}$	$[m]$	Positive current collector thickness
L_{sep}	$[m]$	Separator thickness
n	$[-]$	Number of electrons
N	$[-]$	Number of particles
P	$[Pa]$	Pressure
$Q_{actual,i}$	$[Ah]$	Actual electrode capacity
Q_{cell}	$[Ah]$	Cell capacity
Q_{cond}	$[w/m^3]$	Conduction volumetric heat
Q_{conv}	$[w/m^3]$	Convection volumetric heat
$Q_{Li,i}$	$[Ah]$	Hosted capacity in electrode material
Q_{mix}	$[w/m^3]$	Mixing volumetric heat
$Q_{Ohmic,tab}$	$[w/m^3]$	Tab Ohmic volumetric heat
Q_{irr}	$[w/m^3]$	Irreversible volumetric heat
Q_{rev}	$[w/m^3]$	Reversible volumetric heat
Q_{tot}	$[Ah]$	Total cell hosted capacity

Continued on next page

R	$[J/mol \cdot K]$	Universal gas constant
$r_{p,i}$	$[m]$	Particle radius
$R_{connbar}$	$[\Omega]$	Connecting bar resistance
$R_{c,tab,neg}$	$[\Omega]$	Negative internal tab contact resistance
$R_{c,tab,pos}$	$[\Omega]$	Positive internal tab contact resistance
$R_{c,tab}$	$[\Omega]$	External tab contact resistance
$R_{tab,neg}$	$[\Omega]$	Negative internal tab resistance
$R_{tab,pos}$	$[\Omega]$	Positive internal tab resistance
R_{tab}	$[\Omega]$	External tab resistance
S	$[J/K]$	Entropy
SOL_i	$[-]$	State of Lithiation
t	$[s]$	Time
t_i	$[-]$	Li-ion transference number
T	$[K]$	Absolute temperature
V	$[m^3]$	Thermodynamics volume
V_{cell}	$[V]$	Cell voltage
V_{exp}	$[V]$	Experimental voltage
$V_0 \ E_i$	$[V]$	Equilibrium voltage

Continued on next page

$V_{ol,cc,i}$	$[m^3]$	Current collector volume
$V_{ol,tab,neg}$	$[m^3]$	Negative internal tab volume
$V_{ol,tab,pos}$	$[m^3]$	Positive internal tab volume
$V_{ol,tab}$	$[m^3]$	External tab volume
V_{sim}	$[V]$	Simulated voltage
$Y_{Li,i}$	$[-]$	Dimensionless hosted capacity in electrode material
$Y_{Li,tot}$	$[-]$	Total dimensionless cell hosted capacity
W	$[J]$	Thermodynamic work
w_{tab}	$[m]$	Tab length
Greek letters:		
α_a	$[-]$	Anodic charge transfer coefficient
α_c	$[-]$	Cathodic charge transfer coefficient
$\epsilon_{l,i}$	$[-]$	Liquid phase volume fraction (porosity)
$\epsilon_{l,sep}$	$[-]$	Liquid phase separator volume fraction (porosity)
$\epsilon_{s,i}$	$[-]$	Solid phase volume fraction

Continued on next page

η_{solv}	$[kg/(m \cdot s)]$	Solvent viscosity
η	$[V]$	Overpotential
$\dot{\eta}_{\alpha\beta}$	$[-]$	Moving boundary interface
μ	$[V]$	Chemical potential
Π_i	$[V]$	Peltier coefficient
ϕ_l	$[V]$	Liquid phase potential
ϕ_s	$[V]$	Solid phase potential
ψ	$[-]$	Generic temperature dependent parameter at actual temperature
ψ_{ref}	$[-]$	Temperature dependent parameter at reference temperature
ρ_{cell}	$[kg/m^3]$	Cell density
ρ_{neg}	$[kg/m^3]$	Negative electrode density
$\rho_{neg,cc}$	$[kg/m^3]$	Negative current collector density
ρ_{pos}	$[kg/m^3]$	Positive electrode density
$\rho_{pos,cc}$	$[kg/m^3]$	Positive current collector density
ρ_{sep}	$[kg/m^3]$	Separator density
$\rho_{tab,i}$	$[S/m]$	Tab material density

Continued on next page

$\sigma_{s,i}$	$[kg/m^3]$	Solid phase electrode (electrical) conductivity
σ_l	$[S/m]$	Liquid phase electrolyte conductivity
Subscripts/superscripts:		
a	Anode	
act	Activation	
α	Phase alpha	
BV	Butler-Volmer	
β	Phase beta	
c	Cathode	
cc	Current collector	
$cond$	Conduction	
$conv$	Convection	
DOD	Depth of discharge	
eff	Effective	
eq	Equilibrium	
exp	Experimental	
$host$	Hosted	
i	If p=pos, n=neg, s=sep	
irr	Irreversible	
l	Liquid	

<i>max</i>	Maximum
<i>mix</i>	Mixing
<i>model</i>	Modeled
<i>neg</i>	Negative
<i>Ohm</i>	Ohmic
<i>p</i>	Particle
<i>P</i>	Products
<i>pos</i>	Positive
<i>pt</i>	Phase transition
<i>R</i>	Reactants
<i>ref</i>	Reference
<i>rev</i>	Reversible
<i>sep</i>	Separator
<i>s</i>	Solid
<i>sim</i>	Simulated
<i>solv</i>	Solvent
<i>tot</i>	Total
<i>V</i>	Volumetric

Chapter 1

Introduction

1.1 Background and Motivation

Latest regulatory trends, pushing to limit pollution mitigation and research of alternative fuels, have paved the road toward the vehicle electrification. However, apart from marketing strategies and policies, the the electric energy production and storage are the real engineering problems to address. The latter concerns on-board storage energy devices, batteries for automotive applications and is the main focus of research. This is not an easy task because the traditional fossil fuels have a volumetric energy density much higher than the lithium-ion (Li-ion) batteries as Figure 1.1 is reporting.

Although electric drive-trains give superior performances with energy conversion efficiencies much higher than the internal combustion engine (ICE) [32], the drawback of a lower energy density is heavily affecting the range of the vehicles. For example, a conventional US class 8 heavy truck is able to run 1930 *km* with one conventional diesel tank of 760 *l* while to cover the same distance, roughly 300.000 18650 Panasonic cylindrical cells in the battery pack are needed, adding 20.000 *kg* to the vehicle. It is true that the thermal power-train will be entirely substituted by small electric motors however, the space can be easily replaced by batteries.

Another key concept in providing power via battery is that the battery is not a charge tank, with capacity measured in *Ah* that represents the amount of electric charge that can be stored or retrieved. Rather, the amount of power is depending on charge and discharge conditions affecting the electrochemical nature of the device:

- C-rate,
- Open circuit voltage (OCV),

- Temperature,
- Cell and local state of charge of the electrodes (SOC).

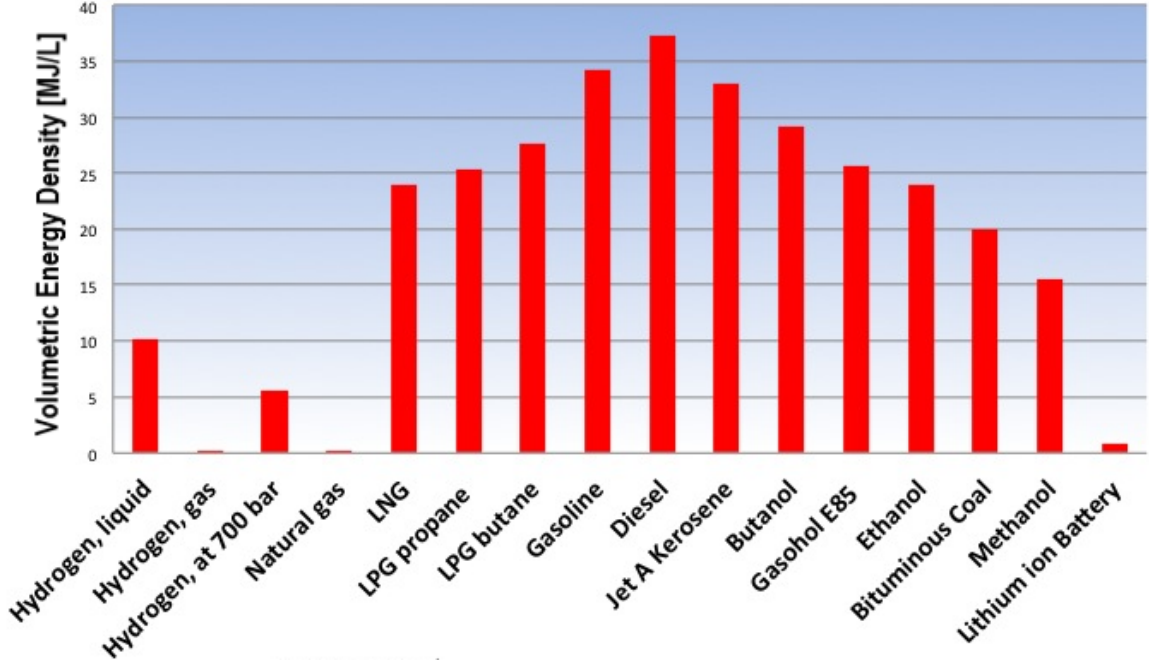


Figure 1.1: Volumetric energy density of transport fuels

Why are Li-ion batteries termed as the most suitable batteries for automotive applications amongst all the battery typologies? As shown by the Ragone plot (Figure 1.2) they have the best energy density available when compared to Ni-Cd, Ni-Mh and Lead-Acid batteries. This results in a higher range for the vehicle with less weight occupied by the battery pack. It must be stated clearly that the distance covered with one complete recharge is the most critical benchmarking parameter from the user's point of view that allows the battery electric vehicles (BEVs) to be comparable to the internal combustion ones [33]. This explains thoroughly why funds and research efforts are invested to study in depth all aspects related to the battery performances. Li-ion batteries have the advantage of offering a small self-discharge rate and no memory effect [14]. Another advantage is a higher open circuit voltage (OCV) compared to the other technologies [34], which combined with packaging characteristics gives smaller fundamental units, called cells, that can be assembled in modular and flexible methods to obtain a complete battery pack that respects design constraints and weight distribution of a typical vehicle [14]. Battery packs concentrate the vehicle weight distribution at wheels level, promising better handling in sudden maneuvers. The higher voltage causes lower losses in the electric energy transmission. However,

all these advanced features come with a cost [35]. For example, [36] reports that for a Renault Zoe with a 52 kWh battery pack, in 2018 the cost per kWh was 160€, hence the total price to buy the battery pack is 8,100€, circa 22.5% of the total cost of the car top version 35,990€. In addition, the cell life and the safety are lower with respect to the competing batteries, because Li-ion batteries are very sensible to external environment conditions, [37, 38, 39]. If the battery parameters are not controlled by a battery thermal management system BTMS, thermal effects can compromise the storage device performances. Starting from capacity fade and self-discharge at high temperature and high rates [23, 40], temperature inhomogeneity causes electrical parameters imbalance, thus leading to uneven aging and utilization of battery cells [14, 41]. In the worst case, when the temperature rises outside the limits, dangerous irreversible and exothermic reactions can start, the battery can emit gas and in the worst case explode. This situation is named thermal runaway [42]. Low temperatures can also cause issues to the Li-ion battery operation [43, 44], as will be further discussed for all these phenomena in Section 2.2.

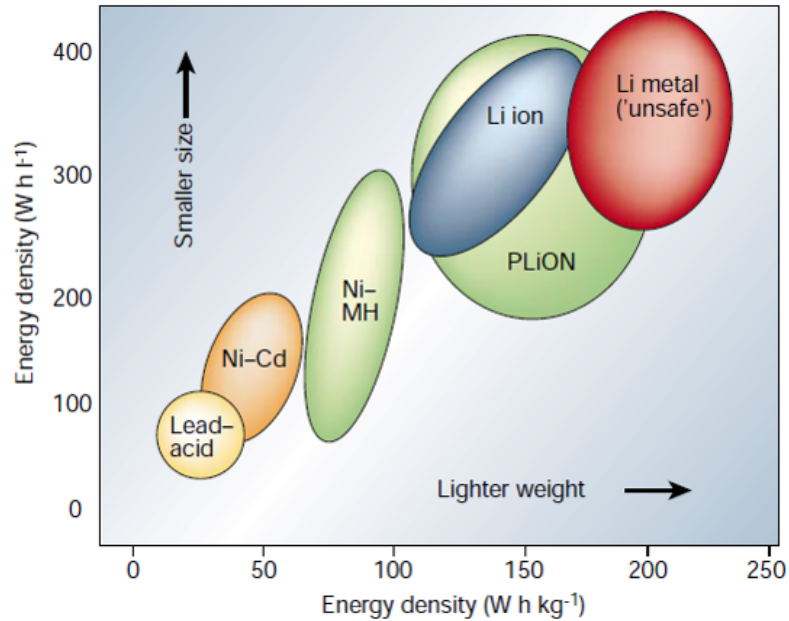


Figure 1.2: Ragone plot of specific power density vs. specific energy density of various electrochemical energy storage devices. Source: [1]

1.1.1 Li-ion Batteries For Automotive Applications

The energy requirements for the propulsion of ground vehicles cannot be satisfied by a single cell, hence many fundamental units precisely connected are required to satisfy the specifications. The single cells are connected in parallel or series in units called modules, and in turn, modules are connected together to give the final battery pack of the vehicle. Designing the connections and the control circuits allows to reach the capacity and energy required by the vehicle. Several original equipment manufacturers (OEMs) are producing different kinds of cells that can differ by geometry, chemistry and output specifications (e.g. capacity, voltage, energy density) [23]. The most common formats are cylindrical (Figure 1.3), prismatic (Figure 1.4), pouch-type (Figure 1.5) and coin size cells. In turn the car manufacturers employ these different cells to develop their battery packs with different strategies and combinations. The most common cell is the cylindrical 18650 (the name is expressing its dimensions $d=18\text{mm}$ $h=65\text{mm}$) that was initially used for HEVs power applications with the exception of Tesla, that used it in combination with a liquid cooled system in a BEV [19].

To give the reader an idea, the first generation of 2012 Tesla Model S has an 85 *kWh* battery pack at 400 – 500V [19]. The cells are cylindrical 18650 NCA Cathode-Carbon/Si anode chemistry. 444 cells (6 groups in series of 74 cells in parallel) gives a battery module. 16 modules in series made up the 7,104 cells battery pack, with a weight of 540 *kg*, Figure 1.6. The battery cost is estimated around 22% of the total car. The Tesla Model S P100D requires 8256 cells to reach a 100 *kWh* battery pack. A different cell, the Panasonic 2170 ($d=21\text{mm}$, $h=70\text{mm}$) is used on the Tesla Model 3, 75 kWh, 478 kg battery pack where only 4,416 cells are needed since this cell has a capacity 4.8Ah instead of 18650's 3 Ah.

1.2 Objective and Contributions

The temperature gradient in a Li-ion battery cell has equal importance, if not more, than the absolute temperature. Thus, this justifies the need for accurate and predictive heat generation models. The majority of automotive thermal studies are focused at pack, [41, 45, 46, 47], or module level, [29, 41, 48] where the thermal variables are easy to detect and control, given the presence of multiple materials and complex structural, electrical and cooling geometries and connections. Less information is available at the single cell level. At this scale, mainly, cylindrical LFP cells were analyzed because higher thermal gradient is expected along the radial dimension. The cylindrical



Figure 1.3: Panasonic NCR18650B cylindrical battery cell. Source: [2]



Figure 1.4: Panasonic prismatic Li-ion battery for PHEVs. Source: [3]



Figure 1.5: A123 Systems pouch cell. Source: [4]

geometry, due its low surface to volume ratio, has a slower heat transport toward the cell boundaries [49]. The presence of a cooling system is even more important in this case. LFP chemistry has dominated the first part of Li-ion cells evolution history due to superior safety, making it the best candidate for general purpose commercial applications. In regard to the automotive world, the research and development in this field has identified NMC chemistry and pouch cells the current state-of-the-art technology. Proven that, each chemistry and battery specific configuration has its unique behavior, in terms of electrochemistry and heat generation, their characterization is heavily required. For example, in [24], the most heat is generated during charge in the negative electrode while in [29, 50] the most critical heat generation is happening during discharge near positive electrode-current collector interface. Most of the batteries under study are of limited capacity, like the ones employed in electronics ranging from $2Ah$ up to $10Ah$ [24, 29, 50, 51], but these are not sufficient for latest trends in automotive power specifications. Only [52], develops a complete thermal electrochemical model for a $53Ah$ pouch NMC cell that is similar to the cell presented in this study.

This thesis has the purpose to develop a P2D model coupled with a 3D thermal energy balance for a high capacity NMC pouch cell for automotive applications. COMSOL Multiphysics[®] v5.5 software environment will be used for the finite element analysis FEA simulations. The presented research project aims to evaluate the heat generation inside a recently developed NMC pouch cell. Sources of heat could be distinguished and characterized due to the advanced electrochemical modelling

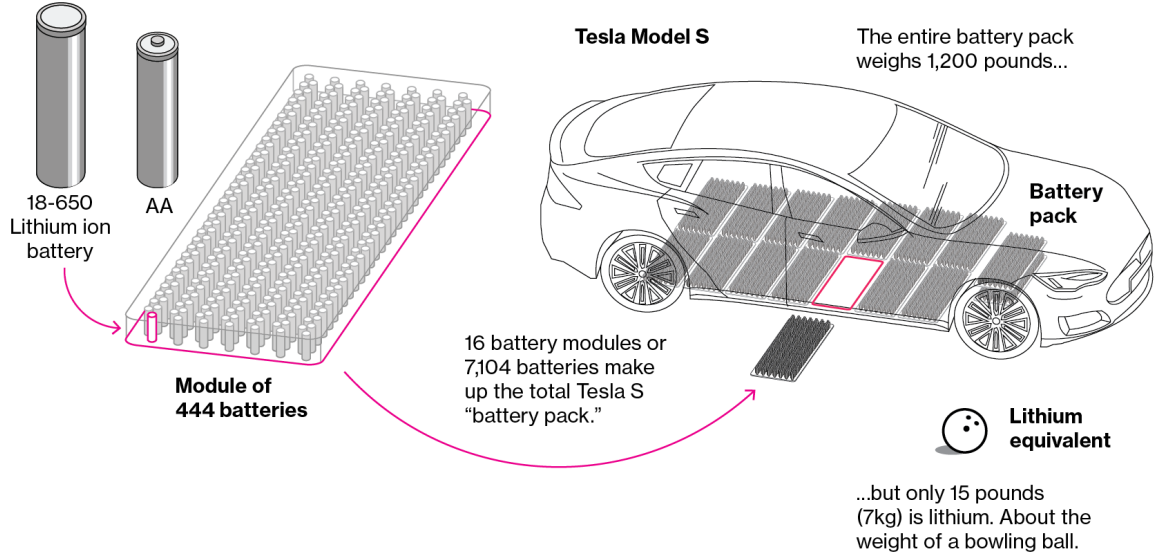


Figure 1.6: Scheme of Tesla Model S 85 battery pack. Source: [5]

approach in various battery operations; for example, during charge and discharge at high C-rates which if not correctly managed could lead to thermal runaway. Pouch cells and in particular, NMC chemistry, are less investigated in literature. The confidentiality of their electrochemical parameters is high between battery manufacturers. Here, a model that joins the deep understanding of electrochemical nature of the battery but with a limited computational burden is developed. With further optimization and testing for a specific battery pack configuration in a vehicle, this tool could be implemented for real time control and estimation in a future BTMS.

In particular, the main objectives are:

- The classification of generated heat sources from the battery electrochemical model and their study under different discharge rates and temperatures. The novel chemistry and high capacity makes this work a useful contribution for the research.
- Develop a simulation tool that embeds the required complexity to understand the electrochemical nature of the battery while allowing fast and accurate computation with respect to a fully 3D thermal and electrochemical model.
- A valuable flexible online engineering tool is obtained making it useful to evaluate design changes. This general objective tool can reduce the need of calibration and experimental characterization.

- The thermal analysis provides insights on what current and voltage profiles are causing the minimum thermal stress on the cell and location of heat that is developed spatially and temporally, allowing an effective design of model-based BTMS control strategy to enhance performance, cycle life and safety.
- Possible improvement of best practices of OEMs to develop advanced cooling systems and BTMS with algorithms presenting high accuracy and low computational burden.

1.3 Thesis Outline

The document is divided in seven chapters where the first one is an introduction to the treated problem while declaring the objectives of this work.

In Chapter 2, firstly, the required battery fundamental notions are explained to the reader. Then it is presented the necessity of joined thermal-electrochemical study of Li-ion battery storage devices, for a complete understanding of their nature. In conclusion, the various possibilities of battery electrical and thermal modelling, to approach this problem, are presented. The state-of-the art solutions are explained both for electrochemical modelling and battery thermal management. These works will be the main references for the analysis presented here.

In Chapter 3, the analytical P2D electrochemical model coupled with a 3D distributed energy balance are explained in their details. All required equations are presented to the reader and a Section 3.3, is dedicated for the models ECT coupling.

Chapter 4 contains the complete description of the Li-ion battery cell under study with fundamental parameters analysis, which are required for the model numerical solution. A specific section is dedicated to the temperature dependent properties, 4.4. In the last part, the model practical implementation details in COMSOL Multiphysics® software are discussed as well as the different simulations to be solved.

The electrochemical model validation against experimental data provided by an OEM, is carried out as a first step in Chapter 5. This allows to test the model under four applied discharge currents and at three temperature values. Temperature dependency is firstly tested here along with its required electrochemical and temperature dependent parameters. Interesting conclusions are drawn for the battery electrochemical-thermal performance and validated also with the available literature.

Chapter 6 includes the final results for the complete electrochemical-thermal model. Simulation results firstly validate the simplified approach presented by the

Author against a fully coupled 3D ECT model for a cell fundamental unit. Heat sources computed by the two models are analyzed and compared. Then two different simulation approaches results are presented, these model the complete cell temperature distribution and temperature rise under different applied currents and thermal boundary conditions.

The conclusion Chapter 7 summarizes all the key findings of these research and expresses the future work requirements.

Chapter 2

Literature Review

2.1 Li-ion Batteries Fundamentals

The fundamental components of a battery cell are the negative electrode and its current collector foil, the separator containing the electrolytic solution, and the positive electrode joined with its positive current collector positioned according to Figure 2.1. Considering a galvanic cell, in most of the cases the negative electrode or anode is made of layered graphitic carbon that coats its copper negative current collector. The positive electrode or cathode has an aluminum foil to collect current and it is covered by an active Li-metal layered oxide. The positive electrode chemistry affects cell performances to a larger extent so its composition can vary by application and it is a constant topic of research and development. The separator is made of plastic polymer (PP or PE) and contains the electrolyte, which is a lithium salt in an organic solvent, and it is often in liquid form. The key feature, enabling the cell operation, comes from the electrolyte. It is an ionic conductor but an electronic insulator; this allows Li-ions to carry the charge inside the battery while electrons are kept outside, carrying the charge through the cables. During the operation, Li-ions travel inside the cell. In discharge situations the ions exit from the layers of graphite in the negative terminal (de-intercalation process) to enter amongst the layer of the positive one (intercalation or insertion process), whereas for charge conditions the operation is inverted.

The assembly of all the components giving a complete cell is termed a jellyroll [7], and it can exist in different formats (Figure 2.2): cylindrical cells Figure 2.2a, coin-type cells Figure 2.2b, prismatic cells Figure 2.2c and the last trend adopted for automotive applications pouch-type cells Figure 2.2d).

The chemistry of electrodes and electrolyte widely affect the performances of bat-

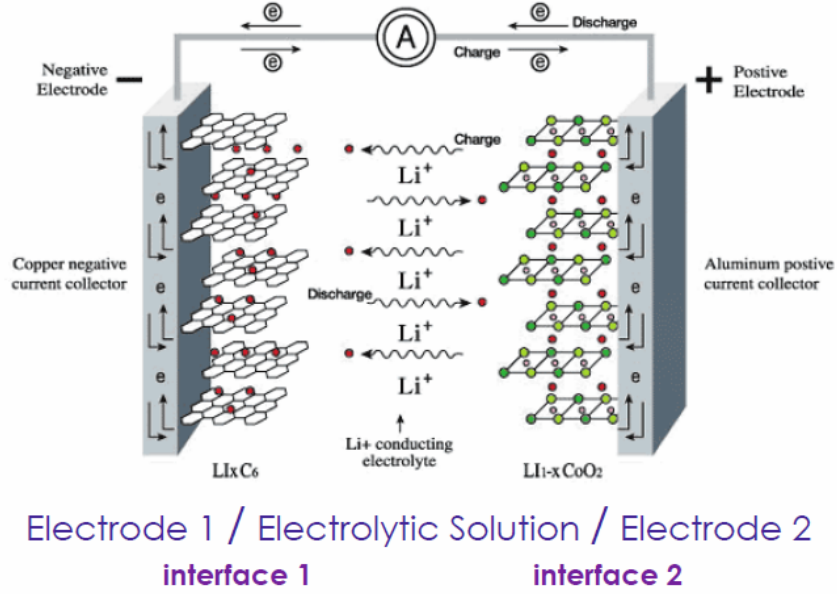


Figure 2.1: Architecture of a typical Li-ion battery cell. Source [6]

tery cells and are constant object of innovation and improvement. The electrode material mixtures have a characteristic open circuit potential (OCP) value for anode and cathode that give the nominal voltage at which the cell operates. The OCP values change with respect to the percentage of Li-ions in the material at a reference temperature and every material has its own characteristic curve. This gives the extremes of voltage where the anode and cathode are operating, which in turns gives the cell voltage. In addition, every composition is characterized by its own specific energy and capacity. Therefore, it is easy to understand why the choice of each material is important to obtain the performance desired by the cell. In this thesis the analysis will be concentrated only on Li-ion batteries since they present superior features as explained previously.

Cathode Materials

The first employed cathode material was the lithium cobalt oxide (LCO) $LiCoO_2$, Figure 2.3 [8]. This is widely employed in consumer electronic devices, offering high specific energy but the specific power and life span are moderate, Figure 2.4, making them unsuitable for automotive applications [53, 34]. The high cobalt cost also reduces their marketability.

The evolution was the lithium manganese oxide (LMO) $LiMn_2O_4$, Figure 2.5, which

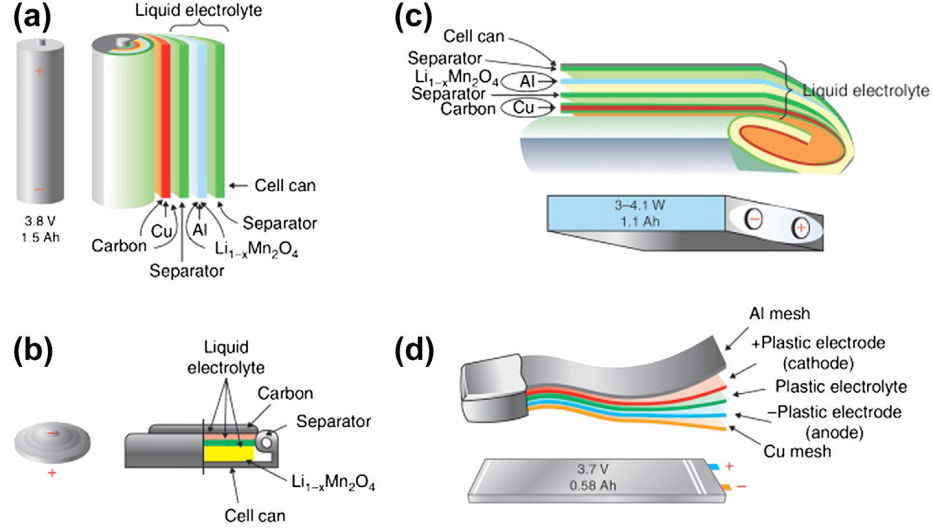


Figure 2.2: Jellyroll disposition for various formats of Lithium battery cells: cylindrical [a], coin [b], prismatic [c], pouch [d]. Source: [7]

has a spinel structure. This 3D isometric crystal structure improves the ion flow resulting in low internal resistance and making fast charging and discharging scenarios possible. The energy performance is increased moderately from LCO chemistry but specific power, safety and life span are improved, Figure 2.6.

A step further was achieved due to the implementation of lithium iron phosphate (LFP) $LiFePO_4$ cathode chemistry, Figure 2.7. As a result of its olivine structure the electrochemical performance is enhanced and the stability provided by the $P-O$ bond prevents the release of O_2 when it is fully charged ending up in less stress in charge conditions. The crucial benefits are enhanced safety, tolerance to misuse, long cycle life and the possibility to sustain a high current rating, Figure 2.8 [8]. The drawbacks are moderate specific energy and elevated self-discharge.

The latest commercially available chemistry is lithium nickel cobalt and manganese (NMC) $LiMnCoO_2$, Figure 2.9, that combines the properties of single elements [53, 34]. Nickel has high specific energy but, being unstable, needs to be coupled with manganese, which stabilizes the mixture while achieving high power due to its spinel structure. This can be seen in Figure 2.10. The proportion between the materials can be varied if a high power or high energy configuration is desired. The former finds its application mainly in hybrid electric vehicles (HEVs) where the electric traction is used mainly for short time but at higher discharge rates. The latter can be a typical case for BEVs in which a high energy configuration is needed to guarantee an acceptable range of the vehicle. $1/3Ni\ 1/3Co\ 1/3Mn\ NMC111$ is the most common

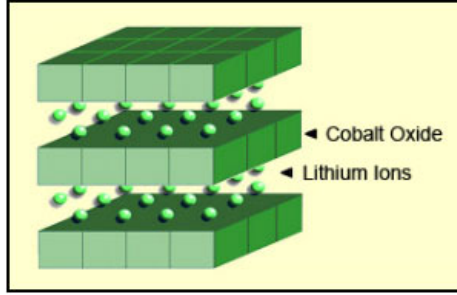


Figure 2.3: LCO crystalline structure. Source: [8]

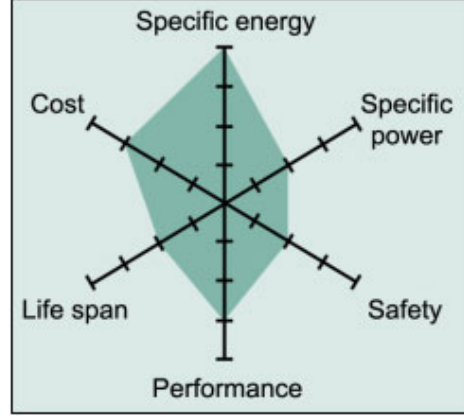


Figure 2.4: LCO web diagram. Source: [8]

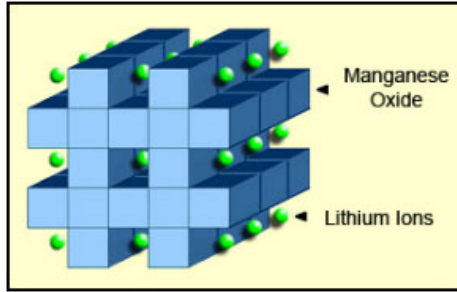


Figure 2.5: LMO spinel crystalline structure. Source: [8]

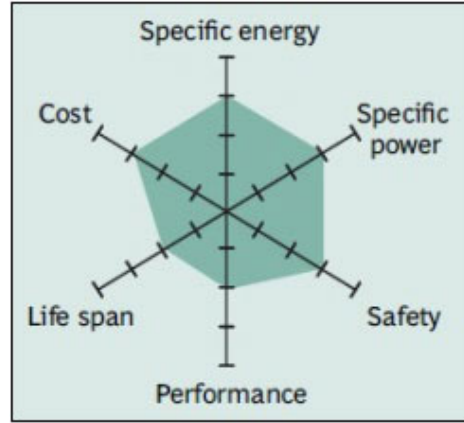


Figure 2.6: LMO web diagram. Source: [8]

configuration that limits the cobalt quantity but others like *NMC532*, *NMC622* and *NMC822* are used by current car manufacturers favoring high energy density [53]. Following the same principle composite electrodes were developed to achieve certain compromises. For example *LMO – NMC* electrodes are combining energy and power densities with higher rate capability and lower cost. This allows the battery manufacturers to tailor the cell composition based on the customer request. Precaution should be taken to avoid an uneven utilization causing uneven aging of the materials. Another alternative is the nickel cobalt aluminum oxide (NCA) $LiNiCoAlO_2$ chemistry which is similar to NMC but with lower cost and safety [53, 34]. This configuration is still used in some electric vehicles.

The research and development for cathode materials has the objective to increase the

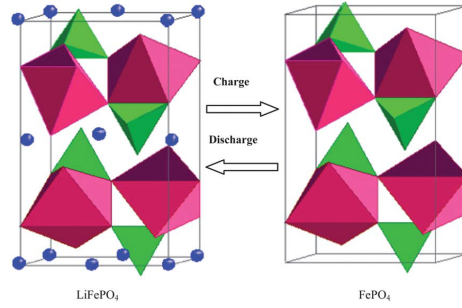


Figure 2.7: LFP olivine crystalline structure. Source: [9]

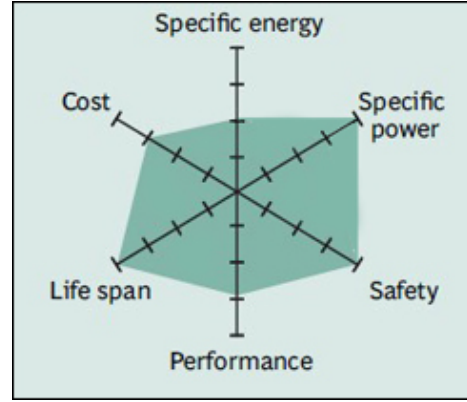


Figure 2.8: LFP web diagram. Source: [8]

voltage and the energy density at which they are currently operating. Lithium anode and sulphur cathode ($\text{Li} - \text{S}$) battery is promising higher energy density with a lower cost however, instability of the compound can cause safety issues reducing the life of the battery along with corrosion effects [33].

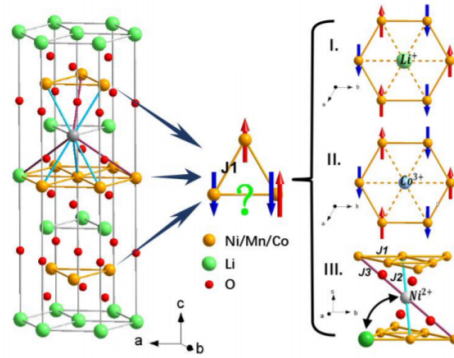


Figure 2.9: NMC crystalline structure. Source: [10]

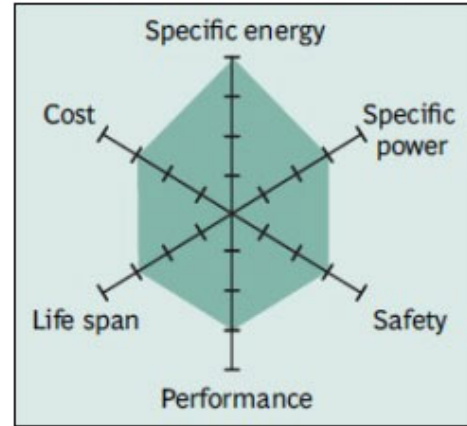


Figure 2.10: NMC web diagram. Source: [8]

Anode Materials

The conventional anode material is graphite LiC_6 and it is one of the most widely used. Li ions can reversibly enter and exit from graphite layers, in a process called intercalation/de-intercalation, as seen in Figure 2.11. The formation of the solid electrolyte interphase (SEI) layer is important to be pointed out. Since the intercalation in graphite occurs at potentials outside the stability window of common electrolytes,

the solvent in it decomposes in a film, the SEI, over the surface of graphite particles in the first charges and discharges of the battery. Some Li is wasted in the SEI formation and the layer is electronically insulating but ionically conductive. The SEI effect can be included in the battery models through film resistance, giving an additional potential drop that can be included in the battery models. As the battery is used the SEI layer grows causing the reduction of the cyclable (Usable) Li inside the battery termed as capacity fade especially at higher temperatures enabling higher electrolyte decomposition and solvent co-intercalation [38, 54]. This phenomenon is taking place mainly on the anode but it affecting the whole cell [54].

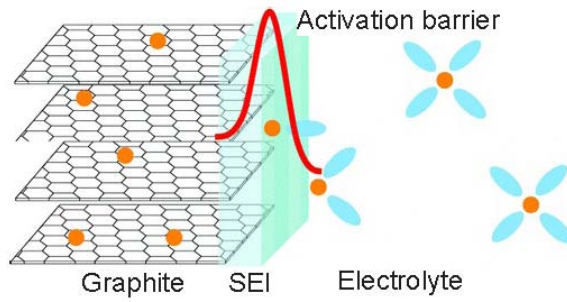


Figure 2.11: Graphite crystalline structure and SEI. Source: [11]

Lithium titanate (LTO), $Li_4Ti_5O_{12}$ is a material used to replace graphite [53, 34]. It has a spinel structure that gives the possibility to fast charge and discharge up to 10C (ten times the rated capacity). In addition, this material is not producing a passive SEI layer and its lower temperature limit is -30°C . This gives to LTO a prolonged cycle life. The main drawbacks that prevent its wide utilization are the high cost and the low specific energy compared to graphite.

The research for future anode materials is evaluating the possibility of exploiting the alloying reaction instead of intercalation, to increase their energy density. The most important factor is that the alloying reaction changes the structure of the host material. The ones compatible with Li in a reversible reaction are tin (Sn) and silicon (Si) providing higher specific energy [53, 55, 56]. The dangerous side is the volume change that the alloying reaction is causing, inducing mechanical stress for the cell and leading to capacity fade in long term. A more feasible composition can be represented by Si-C composites [55], limiting the volume expansion with a carbon matrix containing nanoparticles of Si, keeping the energy density high. The lower volumetric density and the complicated production process are problems that have

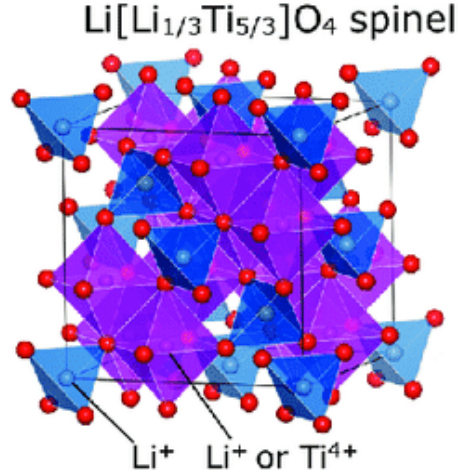


Figure 2.12: LTO crystalline structure. Source: [12]

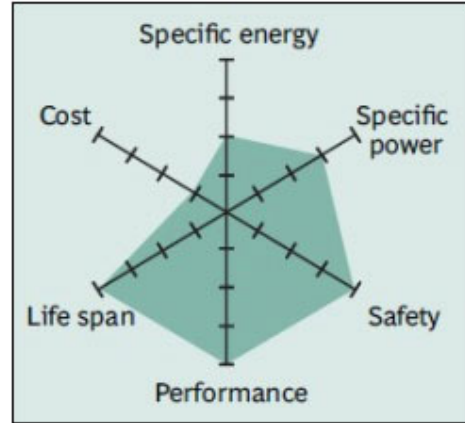


Figure 2.13: LTO web diagram. Source: [8]

still to be addressed [55, 56].

Electrolyte and Separator

The ionic conducting electrolyte is commonly a liquid or gel solution of Li salt, e.g. LiPF_6 , and organic solvents, typically HC-based, and additives. These are often undisclosed but typically it is a mixture of alkyl carbonates (ethylene, dimethyl and ethylmethyl carbonates) [14]. Additives can be used to facilitate the initial SEI formation or to enhance the cell thermal stability [14]. Low voltage tolerance of organic electrolyte and safety issues decomposition in case of contact of HC-liquid and air, have pushed the research toward gel and solid state electrolytes or non-flammable aqueous based electrolyte solutions. Some examples are Perovskites structures, Naiscon like structures or Garnet type structures enabling the cell to work at higher voltage with less safety concerns [57]. Some important challenges have still to be solved such as the increase of grain-boundary resistance due to the solid material [57].

The separator is a thin layer of porous material used to separate the anode from the cathode avoiding an internal short circuit. Usually, it is made by plastic materials PP, PE and their combinations because they can withstand the corrosive hydrocarbons present in the electrolyte. A layered separator can be used to ensure separation of the electrodes at higher temperatures in the order of 100°C [14]. However, ceramic separators are under development to increase the safety of the cell at high temperatures and this material is able to reduce the battery internal resistance [14].

2.2 Reasons for Battery Modelling and Thermal Management

Due to the complex nature of the battery device, it is necessary to study the phenomena and dynamics of the electrochemical reactions happening inside it in depth. The goal is the possibility to forecast its behavior, especially in case of automotive applications where safety, performance, and durability are crucial for customer satisfaction. Performance is mainly expressed in the vehicle range and possibility of fast charge and discharge the battery. Durability is reflected in terms of battery cycle life. Since the assembled cells give the origin to modules and battery packs, problems linked to a single cell can compromise the functioning of the whole battery compartment. Therefore, the necessity to model them correctly is clearly motivated. From thermal point of view, the Li-ion battery behavior must be deeply understood since chemical reactions that generate heat, depending on the electric parameters, are involved. The classical Joule heating phenomena is only one component of the total heat generation from a battery cell [58]. The most advanced thermal models are based on a set of electrochemical reactions laws that explain the working principles of the cell [59]. These models are typically termed as electrochemical-thermal (ECT) battery models and they represent the state of the art of the battery science. A detailed discussion will follow in the next sections.

The lack of knowledge and underestimation of the link between the electrochemical and thermal nature of these energy storage devices can lead to several dangerous issues:

- **Capacity fade/Power loss**

As all components in a car, the guaranteed life that must be ensured by the OEMs to the customers is 10 years [14], but it is not easy if the battery temperature increases because the performance of the battery is reduced [60]. Since individuating all specific degradation reactions is changing chemistry by chemistry, resulting in a complex task, capacity fade is used to describe the general phenomena of Li-ion reduction, in the active battery material [40], thus reducing the amount of available charge with respect to the original battery. The increase of temperature causes the cell internal resistance to rise which in turn produces more heat causing a power loss [61]. The mechanisms of cell degradation are depending upon the cell chemistry [62], as the capacity of the cell appears to degrade independently by the chemistry or rate of discharge when its temper-

ature overcomes $50^{\circ}C$. An example of a specific investigation on the capacity fade mechanism was carried by Ramadass et al. [63], in a Sony 18650 LCO cell. The higher temperature causes the increase of the SEI film on the anode with lithium subtracted mainly by active material from the $LiCoO_2$ cathode [63]. In addition, when batteries are stored, the capacity and power fade are termed as calendar performance loss. However, battery deterioration could still depend by the temperature and initial SOC as presented by Thomas et al. [64], and Smart et al. [39], rising up to 55% lost capacity for temperatures from $55^{\circ}C$ to $70^{\circ}C$.

- **Self-discharge**

The self-discharge rate is limited in Li-ion batteries so it is one of their strengths. For example, in the work of Marcicki and Yang [65], it was evaluated as 1% of the SOC in a $25Ah$ cell. This term is expressed as the drop of cell available capacity without using the cell, in a reversible manner. Also in this case, the specific processes are chemistry dependent. For example, Aurbach [66] points out the tendency of fully charged graphite electrodes to be strong reducing agents and the SEI on their surface not completely passivate them, allowing Li-ions attraction hence lowering the anode potential. Surface species can be dissolved by the increasing temperature favoring the rate of self-discharge. Often, for automotive applications, the rest period of the energy storage is limited so, the self-discharge is not one of the main issues. However, as some authors [62] demonstrated, maintaining the ambient temperature of $60^{\circ}C$ for months can cause a significant capacity decrease.

- **Electrical Cell Imbalance**

Single cells have to be connected in series and parallel to reach capacity (current) and voltage requirements for HEVs and BEVs. In the series connection the weakest cell limits the performance of the entire string. Battery cells with different capacities cause the pack to produce less energy than expected [62], and this is only the immediate effect. Furthermore, charging and discharging the pack can produce severe consequences, especially in Li-ions batteries where side reactions are prone to take place. For example, during discharge, a lower capacity cell can reach the limit voltage faster with the danger of over-discharging. Similarly, during charging there will be the over-charge possibility. The Positive electrode can release oxygen or the negative electrode could experience Li plating [67]. The imbalance is mainly detected as difference of cell SOC [14].

The weakest cell turns out to be also the most used causing uneven aging [14]. The worst cases can end up in a thermal runaway situation. This explains why monitoring the pack only, cannot effectively monitor and prevent this situation in the cells [62]. The series connection requires some sort of balancing circuits. Single cell or reduced groups as the modules must be monitored individually and actively, with the possibility of focusing the intervention. Many cell electrical variables have been proven temperature dependent [62], and so operating at non-uniform temperature will cause additional mismatch. For example, the internal resistance of the battery can vary with temperature. A temperature difference of $5^{\circ}C$ causes a difference up to 40% in the current passing through the cells under the same voltage [68]. An integrated control of battery temperature is fundamental to not cause electrical imbalance. Summing up, the causes of electrical imbalance can be manufacturer tolerances, non-uniform aging, and temperature difference. The last two can be also consequences if the imbalance is not controlled.

• Low Temperature Performance

The Li-ion batteries are sensible to extreme climates. In terms of low temperatures the common threshold is $-10^{\circ}C$ [23, 43], from which energy and power output of the battery are substantially reduced. As the temperature drops below, the capacity of the battery is strongly limited. For example, Nagasubramanian [69] studied the performance of Li-ion 18650 Panasonic cells. He discovered that at $-40^{\circ}C$ the battery is delivering only 5% and 1.25% of energy and power density with respect to the values obtained at $20^{\circ}C$. This has the influence on the vehicle range, a 2012 Nissan Leaf was found having only 63 miles of range at $-10^{\circ}C$ against 163 miles declared for ideal conditions, this is partly explained by the lack of battery cooling/heating system in this model. Other drops of PHEVs range were reported by Shidore and Bohn [70], up to 13% of mileage reduction at $-7^{\circ}C$. The main causes for subzero performance decay are: low ionic conductivity of electrolyte and SEI growth on electrode surface [71, 72], lower solid state Li diffusivity [43, 73], high Li-plating of graphite anode [74], [75] and slow kinetics and transport processes at electrode-electrolyte interface due to an increased charge transfer resistance [23, 43, 73]. Zhang et al. [43] reported that the increase of the charge-transfer resistance is the main contributor of the performance degradation experienced at low temperatures, the resistance increase is also affected by the battery SOC with an inverse pro-

portion. This explains why in cold climates the charging process is more critical than the discharging one. OEMs have developed battery heating strategies to counteract this problem. Due to the Li-ion battery operative temperature range it is fundamental that the BTMS includes both cooling and heating systems.

- **In Cell/Pack Temperature Gradient**

Battery packs are obtained joining single cells in parallel or series connection. Additional components are required, for example bus bars, control electronics, cooling/heating circuits which are built with different materials. These components along with the electrochemical reactions of the batteries generate heat and dissipate it in different manners. This can lead to uneven heat and temperature distribution inside the pack and the battery module [76]. If not managed correctly, the heat can accumulate in inner cells of the pack causing higher temperature. As discussed, the parameters of a single cell are strongly temperature dependent, causing capacity variation between cells. This can lead to electrical imbalance and uneven aging mechanism (capacity fade), affecting the battery's useful life [41]. This could be further emphasized in cases of high applied currents in fast charging/discharging scenarios, single and in cycles [14, 77]. The opposite mechanism can also happen, where abuse conditions create temperature gradients between or inside cells. Since the automotive cells are larger and larger, to satisfy the HEVs and BEVs performance requirements and made of different materials, temperature gradients are favored, inside a single cell [76, 77]. Often the heat generation is not uniform but in some cases, like Wu et al. showed, the heat dissipation from the tab is the most important contribution for the temperature non-uniformity. As an outcome of research tests, the maximum admitted temperature gradient between cells and in the cell must stay below 5°C [78]. It is important to account that the Li-ion battery nature has this thermal-electrochemical coupled behavior, because a temperature gradient causes imbalance in the electrochemical parameters that in turn increases the heat generation. Analyzing the battery cooling solutions of the BTMSs, it is found that some amongst them have the risk to enhance temperature gradient [24, 29]. Some cells formats, enhancing the cell surface area, can improve the tendency of uneven temperature growth inside cells [29]. Concluding the paragraph, it must be clear to the reader that for a correct thermal management of Li-ion batteries the values of temperature gradient has the same importance, if not more, as of the absolute temperature value, to operate the storage in

the optimal performance range. Therefore, they must be jointly monitored and controlled from the cell to pack level.

- **Thermal Runaway**

Thermal runaway describes the condition in which elevated temperature in batteries trigger exothermic irreversible reactions, generating heat, further increasing the temperature and leading to the storage device failure. Mechanical abuse, electrical abuse, thermal abuse and their combinations are its causes [42]. It is by far the most dangerous event if the battery is not thermally managed correctly, its failure modes can be gas emissions, fire and explosion of the battery cells [23]. To reproduce thermal runaway, abuse tests have been developed like oven exposure, short-circuit, overcharge, nail penetration, and crush tests [76]. In this mechanism, there are several reactions triggered at different temperature thresholds, in different sequences. Battery design, chemistry, SOC and abuse conditions affect their occurrence [62, 76]. Several researchers studied a precise example of thermal runaway of a cell triggered by a known cause, and they analyze all the reaction chain that fuels the event [76, 79]. One of first reaction typical of all Li-ion batteries is the SEI interface metastable components which dissolve from 90°C to 120°C [79] and successively at $100 - 130^{\circ}\text{C}$ [76], the exposed negative electrode reacts with the electrolyte in an highly exothermic reaction which further raises the temperature up to 200°C peaks. 130°C is also found a common meltdown temperature of the separator causing a short circuit between the electrodes. Above 200°C the positive electrode decomposes producing oxygen that may react with electrolyte solvent or directly with positive electrode material [76, 79]. Here is where LFP cathodes provide their enhanced safety, withstanding higher temperatures [80]. At these temperatures lithium salt in electrolyte can generate gaseous products that can swell the battery, increasing internal pressure [76]. Al Hallaj et al. [81] in addition, presented that a higher cell SOC can lower the temperature onset of thermal runaway. Conductivity of electrode (electronic) and conductivity of electrolyte (ionic) are often demonstrated to be described by Arrhenius type relations [48], so increasing the temperature more current will be directed in that part of the cell generating more and more Ohmic heat in a positive feedback. Another interesting work done by Kim et al. [82] showed how cells with high surface-to-volume ratio suppressed thermal runaway below 140°C due to the faster ability in transfer heat. The worst possible scenario is by far the cascading thermal runaway where an

individual cell failure induces multiple cells nearby to fail, compromising the whole battery pack. In [83], Cai et al reported for a $4.5Ah$ NMC cell that this phenomenon can be forecast by force signal on the cell surface due to the gas pressure build-up that is preceding the temperature rise, so it is still controllable. Safety pressure releasing vents, shutdown separators, thermal retardants electrolytes and coatings can improve the safety of the Li-ion battery [23, 76]. For these preventive measures to be effective, they have to be coupled with a key component, the battery thermal management system (BTMS), which also incorporates the cooling, a topic that will be discussed in future.

- **Design Considerations**

After discussing all these issues related to this battery typology temperature sensitivity, the importance of electrochemical-thermal modeling of Li-ion battery cells is clear. It allows for their exploitation and for defining optimal charging and discharging curves that cause the minimum stress to the component while achieving the maximum performances.

Some authors and battery OEMs provided the suggested temperature working ranges for Li-ion batteries. Pesaran [84] firstly suggested the suitable range between $25^{\circ}C$ and $40^{\circ}C$ with a maximum difference of $5^{\circ}C$ module to module. Later, he individuated $10^{\circ}C - 35^{\circ}C$ as desired working temperature for safety, life and performance of Li-ion batteries, Figure 2.14. Manufacturers like Panasonic suggest a $0^{\circ}C - 45^{\circ}C$ range for charge and $-10^{\circ}C - 60^{\circ}C$ for discharge [85]. LGchem suggests $0^{\circ}C - 50^{\circ}C$ charging range and $-20^{\circ}C - 75^{\circ}C$ as discharge range. This is a further proof that charging performance is the most critical one. Some authors like Ladrech [86] divide the temperature range into zones where the optimal one lies between $20^{\circ}C$ and $30^{\circ}C$. Figure 2.15 summarizes the temperature ranges into: optimal temperature range; operational temperature range where no reduction in battery life is expected during normal operation; and survival temperature range, where it is known that problems may arise toward thermal runaway or low temperature performance issues. Temperature in a Li-ion battery should be kept below $40^{\circ}C$ and at minimum above $15^{\circ}C$.

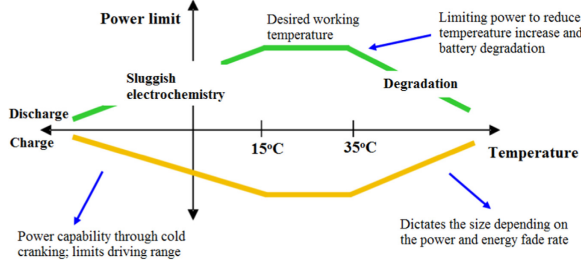


Figure 2.14: Optimal temperature range for Li-ion batteries. Source: [13]

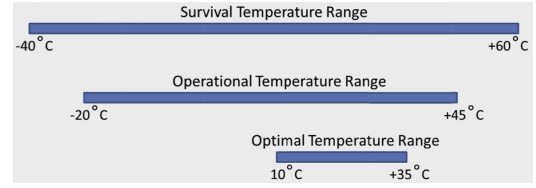


Figure 2.15: Summary of temperature ranges for Li-ion Batteries. Source: [14]

2.3 The Output of Battery Modelling: Battery Management and Thermal Management

Results coming from the battery modelling are used as inputs for the battery management system (BMS) and battery thermal management system (BTMS) which is in charge of controlling the battery pack through the cooling system.

Battery Management System BMS

With the name of battery thermal management system (BTMS), all the principal functions of control of battery cells are included from all aspects, namely battery management system (BMS) and especially the thermal one. The need of some control entity was clearly expressed in the previous section. Automotive batteries present unique challenges compared to their implementation in portable electronics. The discharge is not always constant and with a fixed slow pace, as all automotive components 10 year's life must be guaranteed [14], dealing with harsh conditions and temperatures at which the vehicle is exposed. In addition, not all electric vehicles applications have the same requirements. HEV batteries are subjected to continuous charge and discharge [68] at higher rates up to 10C (battery in power configuration), causing higher temperature rise [14]. BEV batteries are subjected to longer but less intense discharges near 1C (battery energy configuration) ending in less temperature increase.

BMS is made by several components, a master controller with slave components: PCBs (integrated circuits), high power switches (MOSFETS) and sensors arranged in different topographies. An important part is made by software and system control electronics, usually using CANbus or Flex Ray networks which permits detachment, preserving the electronics in a short circuit event [49].

BMS main functions are:

- Protection for over-charging, over-discharging, high temperatures, low temperatures, short circuits and other failure modes. This guarantees safe operation, even taking into account physical damages that can occur to the battery [68],
- Monitor the state of battery and cells: SOC, SOH, maximum voltage and current. From SOC, SOH and temperature T is estimated the current to not overcome the limits in a future time interval, delta time. This enables the management of power sources/sinks. For example, the charge current from regenerative braking or cruising is sent to the battery pack or otherwise is dissipated in a resistor pack (reducing overall HEV efficiency),
- Optimization of performance, as objective, in terms of control charging/discharging while not damaging or reducing life and balancing the charge.

This is necessary since Li-ions batteries offer superior performances but they need tighter control with respect to other battery typologies. Some example of racing applications have no long term BMS since the storage is substituted every race but generally all production application have a BMS [14].

The master controller embeds these tasks:

- Monitor pack voltage and cell control boards voltage,
- Control charge and discharge current,
- Monitor pack temperature, communicate with the cell boards to know their temperature and based on the reading, manage the heating/cooling units,
- Opening/closing contactors (battery to motors, charger to battery) for safety management based on Voltage, Temperature, SOC and SOH,
- Calculate, manage and track SOx functions and interact with vehicle ECU or other master system, reducing current and knowing the range and pack status (remaining capacity, energy).

BMS architecture can be distinguished mainly in centralized or distributed. Centralized BMS, Figure 2.16 , presents one control unit and cell control units in one place with wires going to the periphery. This maximizes the wiring and lowers the

hardware count. Distributed BMS, Figure 2.17, has one master controller and slaves directly mounted on cells or modules. Higher costs for more PCBs is expected but in return for greater functionality and localized control. Hybrid combinations between these two are also possible.

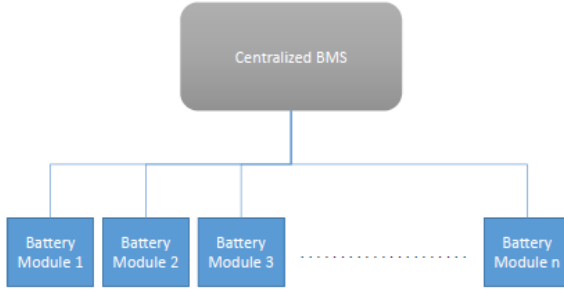


Figure 2.16: Centralized battery management system structure. Source: [14]

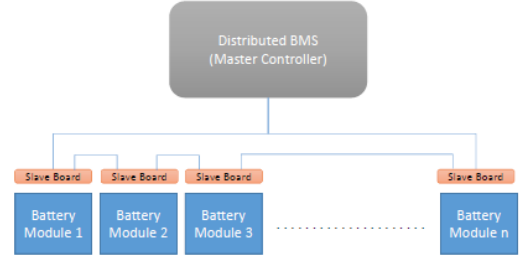


Figure 2.17: Distributed battery management system structure. Source: [14]

The control logic can be programmed, with static limits, that are basically look up tables implemented in the hardware and generally safe. Or, if a dynamic model estimator is employed, the limit values are calculated based on the situation and the battery performance is exploited with greater extent. In the optimal situation a smaller pack with a dynamic control can achieve the same performance of bigger one controlled statically [68].

One of the crucial tasks of this system is charge balancing. This expresses the action of maintaining the cells in the pack at same SOC. It is important so, the weakest cell does not limit the pack, for example, if one single cell discharges more, the remaining charge contained in the others is not used. Moreover, the cell that is more exploited will also experience more aging. The objective is to bring SOC levels close and thus maximize capacity [87]. This function is fundamental because Li-ion cells of the same model are never equal to the others, even from the factory [68]. The charge balancing is specifically referred to cells in a series connection, the ones connected in parallel are automatically balanced and generally considered as single cell. Two main strategies are employed for cell balancing. Passive balancing is used when the cell with highest SOC dissipates energy into heat with a resistor. It is possible to act on multiple cells but not at the same time. Attention must be paid on where to dissipate heat. This intervention takes more time than active system and does not improve the discharge process. The capacity discrepancy will increase over time decreasing the utilization of the cells [49]. Active balancing refers to the action of moving the SOC from the cell in excess to lower one until they are all equal. DC-DC

converters make the balance possible during charge/discharge and rest periods [49]. No energy is wasted but there are higher hardware costs and more space is required to allocate additional electronics on slave boards. Since no proven long term benefit exists for this solution, it is not used [14].

Battery Thermal Management System (BTMS)

Battery modelling, especially from the thermal point of view, is crucial to guarantee performances and safety in all use cases of a vehicle. Another point of emphasis is identifying also what are the parameters influencing the heat generation in the battery (e.g. C-rate, SOC). It is demonstrated that Li-ion batteries have temperature dependent properties, often described by Arrhenius law. For example, the reaction rate can double for each 10°C of temperature rise against the heat dissipation rate, which is increasing only linearly with temperature rise, assuming constant heat transfer coefficient [68]. Results of model predictions are inputs for designing the BTMS, battery thermal management system, that is in charge to control the battery pack through the cooling/heating system.

The main functions are devoted to achieve the objectives explained in the design considerations paragraph [17]:

- Regulate the batteries to operate in the desired temperature range,
- Reduce uneven temperature distribution (in-cell and in-pack) avoiding localized deterioration.

Its contribution is fundamental, especially in large cells, where the aging mechanism is dependent on temperature history of the cells. Usually in the center of the pack the temperature is different from the one on the boundaries. Even if the starting point is identical, over time they will perform and age differently [68]. This prevents even aging, affecting service life availability and safety [49]. Temperature also affects cell balancing, higher temperature provokes high reactions [68]. on the other hand, preheating can be adopted to reduce loss in energy or rate capability at low temperatures [23].

The complete system is made of coolant, heat exchangers, shields, fans, valves, pumps, sensors and a control logic. The selection of heating and cooling solutions can prevent temperature cell-to-cell differences, and also gradients inside the single cells. BEVs battery cooling/heating methods must be considered differently from HEVs ones, which must face higher temperature rise [23]. Each method has its own advantages and disadvantages. Each car manufacturer applies its strategy to achieve

the best compromise in terms of cost, complexity, safety, weight, efficiency and space requirement [49]. Furthermore, a common goal for automotive is to use little energy for operation without affecting cabin comfort [23].

Thermal management solutions are usually classified into internal or external and active or passive. Another main classification is dividing them by the adopted mean. Internal systems are called the ones where heat is directly removed from the source inside the battery, not going to its surface [23]. An example is [88], where phase changing internal cooling, with micro-channels incorporated inside the battery, is used. However, the research is limited, future exploration on the field is promising more temperature uniformity [89]. External type cooling systems can be either passive or active, where a medium is forced through the pack.

Heat Sinks

This is a passive typology of cooling system, rarely used alone. Heat sinks through aluminum or metal pack housings of the battery and it is taken away. It is effective in low discharge rate packs, due to low heat generation. It is also called conductor cooling. Fins or heat spreaders are more effective when they are exposed to air or air is forced over them [14].

Phase Change Materials PCMs

Phase change materials (PCMs) combine large latent heat of fusion with a suitable melting point [23]. Most used materials are based on paraffin wax and graphite to absorb heat coming from the cells, softening from solid toward liquid state, Figure 2.18. Criteria for PCM design were listed by Rao et al. [90]: suitable melting point in the range of battery operating temperature, high latent heat, heat capacity and thermal conductivity, low volume dilatation, no freezing behavior, cost and safety. The melting point is suggested near $40 - 44^{\circ}\text{C}$ [91], or $30 - 50^{\circ}\text{C}$ [92]. This is achieved with the correct chain length of paraffin wax [76]. The optimal melting range is suggested below 45°C to have the maximum allowed temperature near 50°C [23]. Poor thermal conductivity, typical of these materials, limits fast response [23]. The balance of PCM thermal conductivity and cell thermal conductivity is also fundamental for proper temperature distribution. Composite PCMs are the solution, with a wide range of possibilities [76]: insertion of nanoparticles, graphene, carbon nanotubes (CNT), metal matrix, porous materials and high thermal conductivity substances (e.g. aluminum fins on sides [91]). PCM/graphite seems the best choice to direct heat from center to outer zones. The enhanced thermal conductivity decreases the

amount of latent heat that can be stored, so, this trade off must be carefully designed. PCM is proven as an effective uniform cooling method [47] against air cooling, with the advantage of being cost effective since it does not require additional components. However, technical limits are still a problem: the material is limited to a maximum temperature, after which complete melting occurs [62], after that the cooling is inefficient causing additional thermal resistance [23]. Liquid cooling or PCM/heat pipe combination can solve the problem since PCM alone or joined with air cooling are not enough. The material volume expansion is another concern and one of the main drawbacks is the difficulty of using PCMs for battery heating purposes.

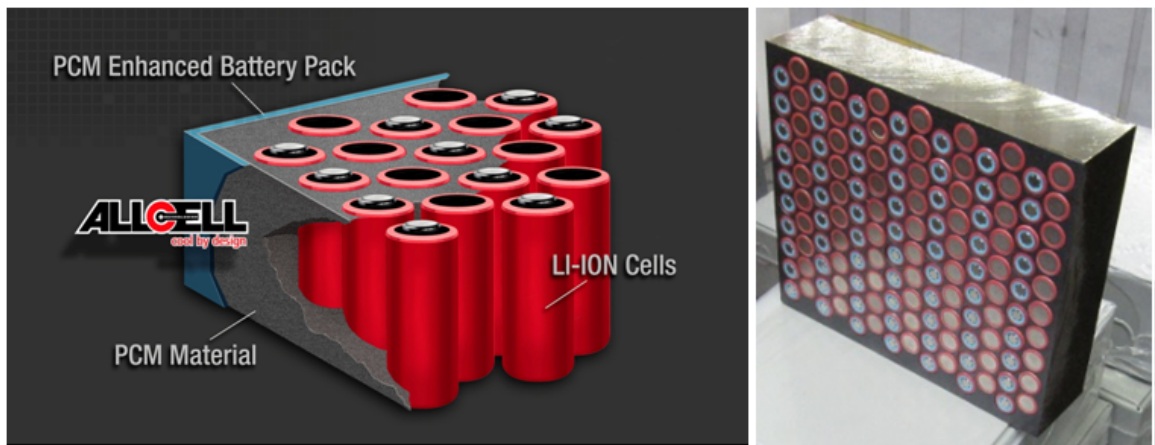


Figure 2.18: PCM enhanced battery pack. Source: [15]

Air Cooling

Air cooling is divided into natural or forced. Forced air cooling is proven to be effective in reducing the maximum temperature but causes higher thermal gradient across the cell and the pack [24, 29, 50]. Air cooling solutions are cheaper, of lower weight and simpler with respect to other strategies but they can be bulky (large space between cells and large ducts [49]) and need proper sealing to work safely. In some cases, the air of passenger compartment is used to cool the battery, filters are necessary to guarantee the maximum safety [49]. In this case it is only possible to cool the battery if passenger cooling is working. This could be a problem, both for cabin comfort and battery management [49]. If ambient air is used, the cooling ability is limited to ambient temperature [14]. Better performances are offered by parallel systems of A/C loops, one for battery and one for the passenger area. This solution needs space and additional weight but no filtering needs [49]. Generally, these systems are not suited for batteries with high energy density, like Li-ion ones.

In fact, an application is found in 2001 Toyota Prius Ni-Mh battery pack, because they have lower and less strict safety requirements. Conditioned air is coming from the cabin, with a parallel air flow scheme, Figure 2.20b. $4 - 8^{\circ}\text{C}$ thermal gradient is obtained across the pack depending on blower speed and ambient temperature [93], but at 0°C up to 11.4°C of thermal gradient are measured [93]. In the end, air is not effective as cooling medium as liquid [14]. When air is going through the pack last cell will experience less cooling, producing more aging [14], especially in a series air flow configuration [68], Figure 2.20a. It is not sufficient in all situations, only in low energy density batteries [76].

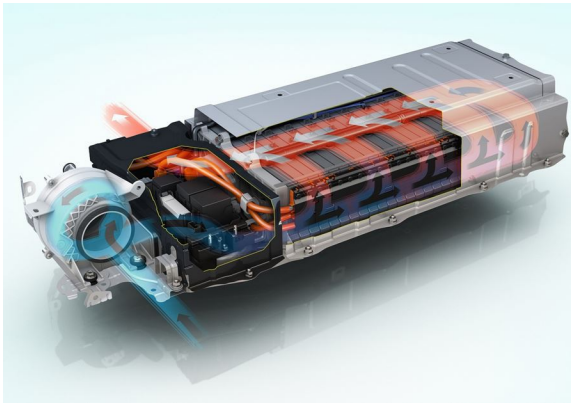


Figure 2.19: Toyota Prius battery pack forced air cooling system. Source: [16]

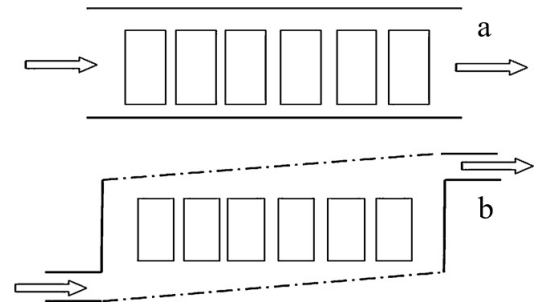


Figure 2.20: Airflow in a battery pack: a)Series airflow b)Parallel air-flow. Source: [17]

Liquid Cooling

Liquid cooling represents the state of the art of BTMS and it is widely employed in current HEVs and BEVs. It is made up of plates, heat exchangers and hoses. It offers a quick response and it has the possibility of heating with engine cooling in HEVs [68]. It has higher efficiency compared to other strategies but it is heavier, more complex and expensive. It is easy to seal since it is a closed environment (can be adopted for external mounted packs [14]).

Common solutions are [14]: cooling plates directly attached to the cells (bottom or side) with fluid inside. Cooling fins, where a main single plate is connected to the cells with a series of fins (heat spreaders). Another possibility is submerging modules in a fluid. One of the best solutions is employing active cooling plates between cells, which achieves homogeneous temperature inside the pack/cell due to higher thermal conductivity and heat capacity, more than three times than air [62]. It is also one of the most expensive possibilities.

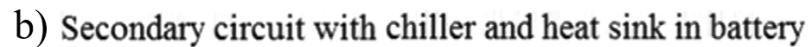
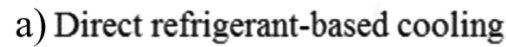
The cooling system can usually adopt as mean the A/C refrigerant circuit or a dedicated cooling circuit:

Cooling with refrigerant is the most compact strategy, Figure 2.21a, the evaporator is directly in the battery, connected in parallel with the main evaporator. It Provides effective cooling, and ducts topology could be optimized for homogeneous temperature distribution. Hydrofluoroether boiling in mini-channels was studied by [94] and [95], and was able to keep the temperature below 40°C at 20C discharge. These systems are effective for pulse discharge and with this solution is easy to differentiate battery and cabin requirements [49]. Refrigerant systems have generally higher cost then coolant ones but lower space requirement since there is no need of chiller and extra loops [23]. The main drawback is the difficulty to implement battery heating [23].

Cooling with coolant is the most flexible solution, Figure 2.21b. It requires a secondary loop. The working fluid is made up by water plus coolant (water-glycol 50-50 mixture as engine coolant), typically working in $15 - 30^{\circ}\text{C}$ range. The chiller connects refrigerant circuit with the secondary cooling circuit. It evaporates the refrigerant drawing heat from the secondary circuit. Other components are: pumps, pipes and the low temperature radiator, which enables battery heating during winter. It also prevents the compressor from working, increasing energy efficiency of cooling system [49]. The circuit is able to manage pulse discharge and battery heating but with higher cost due to increased weight and complexity [23]. Tesla patented cooling system, Figure 2.22, and GM volt cooling system, Figure 2.23, are an example of this solution.

Heat Pipes

This is an innovative cooling method which uses latent heat of vaporization from evaporator to condenser, to transport the working fluid by pressure difference [23], Figure 2.24. Tran et al. [22], compared this low energy cooling device against heat sinks on a HEV Li-ion battery. He presented that the thermal conductivity can be improved up to 30% under natural convection against a common heat sink. Rao et al. applied water heat pipes thermal management strategy to a battery, demonstrating that they are able to keep maximum temperature and temperature distribution under cyclic testing, but only below a certain value of heat generation [96]. However, their feasibility is still under study. The performance is enhanced from simple heat sinks but no performance improvement or cost advantage is making them suitable for automotive applications [14]. The liquid which converts to steam is limited, because above a certain temperature (fluid dependent), all liquid is in vapor form, preventing



the circulation [14].

Low temperature performance is a field where the research is less developed, mainly because consequences are less dangerous than over-temperature. Thermal runaway catastrophic consequences are avoided; however, for an EV low temperature performance could be a problem if totally underestimated [76]. The trend is to use smaller batteries, like HEVs ones that generally need only cooling, since they heat up very quickly [49]. As we grow in power and energy requirements, like in PHEVs or BEVs, not as much intensive cooling is needed; for example only in certain situations as fast charging. In this second case, battery heating is fundamental, since the vehicle autonomy relies only on electric energy storage. Different systems could



Figure 2.22: Tesla Model S battery pack tear-down. Source: [19]

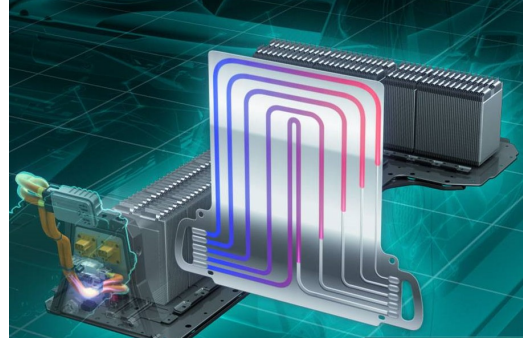


Figure 2.23: GM Volt inter-cell battery cooling plate. Source: [20]

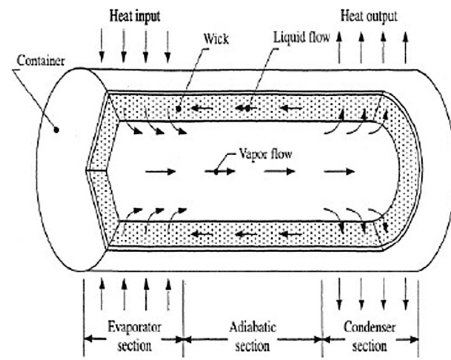


Figure 2.24: Heat pipe working scheme. Source: [21]

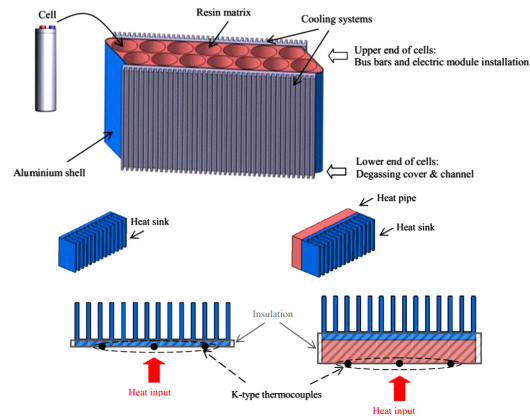


Figure 2.25: Heat pipe application for HEV battery pack cooling. Source: [22]

be implemented based on heating time, power consumption, cost and complexity. The objective is to reach 20°C which is the start of the desired temperature working range. In the worst case where this cannot be guaranteed the vehicle range can be sensibly reduced as presented in the low temperature paragraph. Solutions are generally divided into internal or external power heating methods. One internal strategy is self-heating (or core heating) which uses current pulse profiles to generate heat inside the battery [68]. It is found to be an effective method [97], since the battery internal resistance grows at higher temperature, so the higher heat generation is exploited. Mutual pulse is called when a discharge of a part of the battery pack is exploited to power the other one with cyclic repetition [76]. An example of external power heating method is represented by fossil fuels heating systems, applied mainly in HEV equipped with range extenders or commercial vehicles [49]. Another distinction can

be done if the heating method is direct or indirect. Direct heating could use electric heaters, air heating from main HVAC of the car, from a dedicated unit at battery intake, or directly using the air from passenger compartment. Direct electric heating strategy is one of the most used, it is quick and effective. Thermal foils plus resistors are the main components as example, Nickel foils inside the battery are employed for internal heating [44]. It allows precise temperature control, but it must be safely controlled, especially if no positive temperature control (PTC) strategy is implemented [49]. Direct liquid heating, for the high outlay, is not that much used despite a high heat transfer rate and homogeneous temperature distribution [49]. Indirect heating is used when the elements are heated by adjacent surfaces, through heat pumps or high voltage liquid heating devices. It is less effective than foil heating. Furthermore, preconditioning of the battery pack can happen while the car is still plugged, not affecting the range. In addition, it is important to consider battery heating along with battery compartment insulation for lowering the energy requirements [49].

2.4 Battery Modelling Approaches

A Battery model is a set of mathematical equations that explains with a certain degree of approximation what is the behavior of a studied battery and its performance [23]. There are different degrees of complexity with which, this problem can be addressed, Figure 2.26. Approaching to battery thermal analysis there are two modelling areas that must be covered and interfaced. The first is the actual battery model, explaining the performance of the storage device under observation, which is depending on the detail of the description required, Figure 2.26. Then the second part is the heat sources characterization and energy balance of the cell. They are relying on one another, Figure 2.27, and there are several possibilities for studying and coupling them. Some classifications are coupled, decoupled; empirical or first principle models that will be briefly explained in the following.

Starting with the battery description, Figure 2.28, the first distinction is between empirical (Heuristic) models or equivalent circuit models (ECM) and first-principle or electrochemical (EC) models. The first ones characterize the input/output behavior of the cell exploiting the analogy of electrical circuits [59]. They don't include descriptions of battery physics and they are classic black box models. Their identification comes from the experimental data, which are necessary. Electrochemical models, instead, predict cell behavior starting from their nature with a detailed physical description which includes thermodynamics, kinetics and mass transport [59]. These

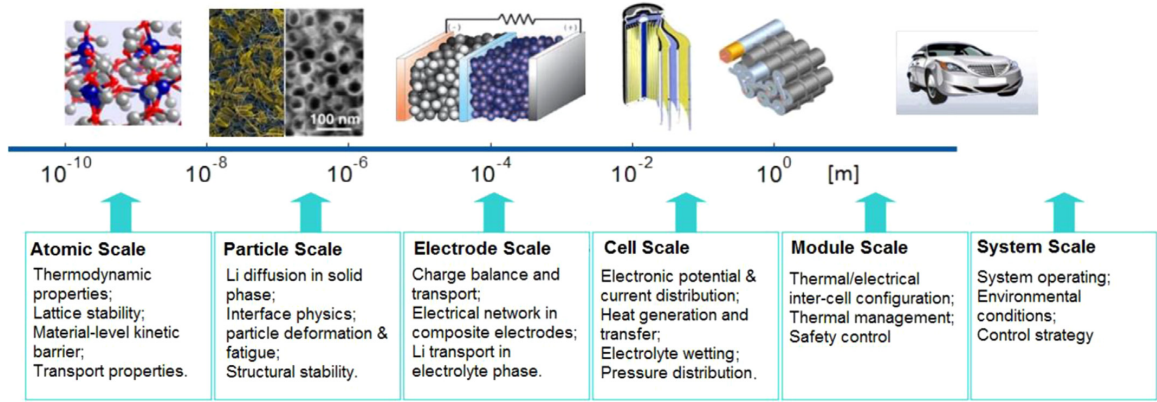


Figure 2.26: Multi-scale physics and micro-macroscopic modelling approach applied into a lithium-ion battery. Source: [23]

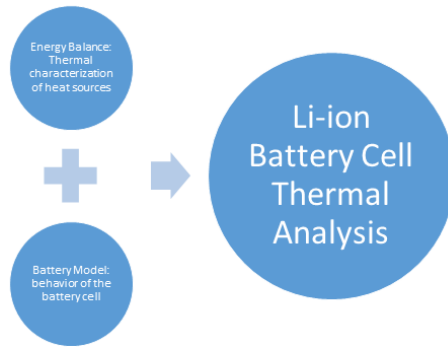


Figure 2.27: Conceptual approach to Li-ion battery thermal analysis

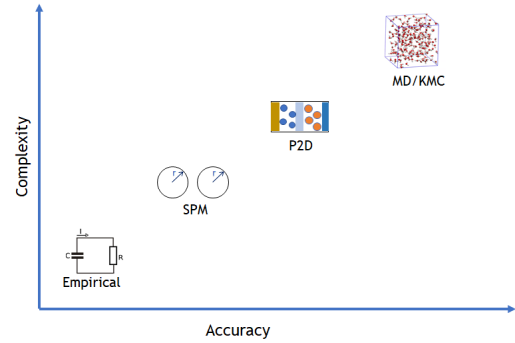


Figure 2.28: Li-ion battery common models scale comparison. Source: [24]

models are very specific and require lots of parameters, coming from the battery chemistry, which are obtained from material properties or by tests and teardowns. The most advanced battery model is the Kinetic Monte Carlo KMC, where variables are describing the molecular dynamics. These advanced techniques are used for specific processes, like the growth of SEI layer in the anode, and for limited time fractions [98, 99].

2.4.1 Equivalent Circuit Models (ECM)

ECMs are the most suitable models to predict battery outputs given the input conditions such as current profile and temperature. The clear aim of these models is not to describe the cell construction but rather to characterize its behavior to obtain

a response of various use scenarios. The electrical analogy is used to model the energy storage, through: resistors, capacitors and voltage sources from the network theory [23]. The majority of actual BMSs and BTMSs, currently implemented in production cars, use different typologies of these models [59]. The models are sufficient to describe the behaviors of large cell battery packs and maintain their operating ranges. The estimation of internal cell states is possible through the available electrical parameters. The balance between complexity and accuracy is satisfied, allowing fast computational speed that allows these models to be easily implemented in microprocessors of control systems for real time results [100, 101].

Various possibilities of these models are:

- Rint model (or Internal Resistance Model),
- Resistance capacitance (RC) model,
- Thevenin model,
- PNGV (Partnership for New Generation of Vehicles).

Rint model assumes the battery as ideal voltage source with a resistance connected in series [102]. The model is the simplest possible but only captures the static behavior of the cell [59]. The dependency of the voltage from the SOC is captured. RC model adds capacitors components on the branches, to have more realistic characterization [102]. It is used for Li-ion batteries and it can capture the dynamic behavior of the cell with additional required parameters. Thevenin model adds a parallel RC loop to the Rint model network [102]. This model is also a dynamic or first order model through the tunable time constant; it accounts the polarization which is the departure of the cell from the equilibrium potential [59]. Adding a capacitor in series to the Thvenin model leads to PNGV model, which is able to describe the change of OCV in time of accumulation of the load current [102]. Nonlinear ECM models were presented, like [103], which captures the magnitude difference of internal resistance during charging and discharging. Parameters of the various models needs to be calibrated. This is the toughest part of these typology of models, since one parameter can be function of several variables (e.g. SOC, C-rate, temperature). This parameter identification procedure needs a great number of tests and the current research is trying to standardize it. One example is the method proposed by Hu et al. [103], based on separate identification of each parameter, by isolating a portion of the voltage response.

In conclusion, these models are intuitive and simple to build. Low computational effort is necessary since they are expressed by lumped parameters in linear ODEs. They allow the needed complexity to express nonlinear behaviors of the batteries. The drawback is the non-standardized, difficult and long calibration procedure. If the model order increases, the parameter identification is in turn more complex. The models are mainly descriptive and they require always the experimental counter-part. The actual electrochemical reactions of the cell are not captured (cell internal dynamics [59]) and this prevents an exhaustive description of some use cases of the vehicle. Some examples are fast charging/discharging and aging mechanism characterization [101]. This limitation prevents the ability to apply design changes and use intensively virtual engineering approaches. The fitted parameters for ECM prevents their utilization in very different situations from the ones where data were collected [101, 104]. Especially in BEVs the battery is the main and only energy source so all the possible effects influencing its life must be characterized from the root causes. These models find their main application in battery management but they are not accurate enough for a lower scale research. Limitation on thermal side where ECM, not accounting reactions, have heat generation reported just as a source. The only possible thermal models that can be coupled are lumped thermal models which are not able to capture the thermal gradient of the cell.

2.4.2 Electrochemical (EC) Models

Electrochemical models (or First Principle models) describe the battery starting from the fundamental physical phenomena. These includes: mass transport (ions diffusion), kinetics (charge transfer reaction at interface) and thermodynamics (heat generation). They use coupled partial differential equations PDEs that can describe three dimensional variable changes. The increased complexity makes necessary to use numerical solution techniques. They are more accurate than ECMs but they are not completely substituting them since they have different applications at the moment. Figure 2.29 sums up the advantages and disadvantages of ECM and EC modelling approaches. The latter one will be deeply analyzed in the following.

Pseudo Two Dimensional Model (P2D)

The first electrochemical studies are done by John Newman characterizing the reactions of electrochemical systems [105]. He deepened its electrochemical studies presenting the concentrated solution theory and after the theory for porous electrodes [106]. From 1991 to 1993, Doyle, Fuller and Newman developed the Pseudo Two

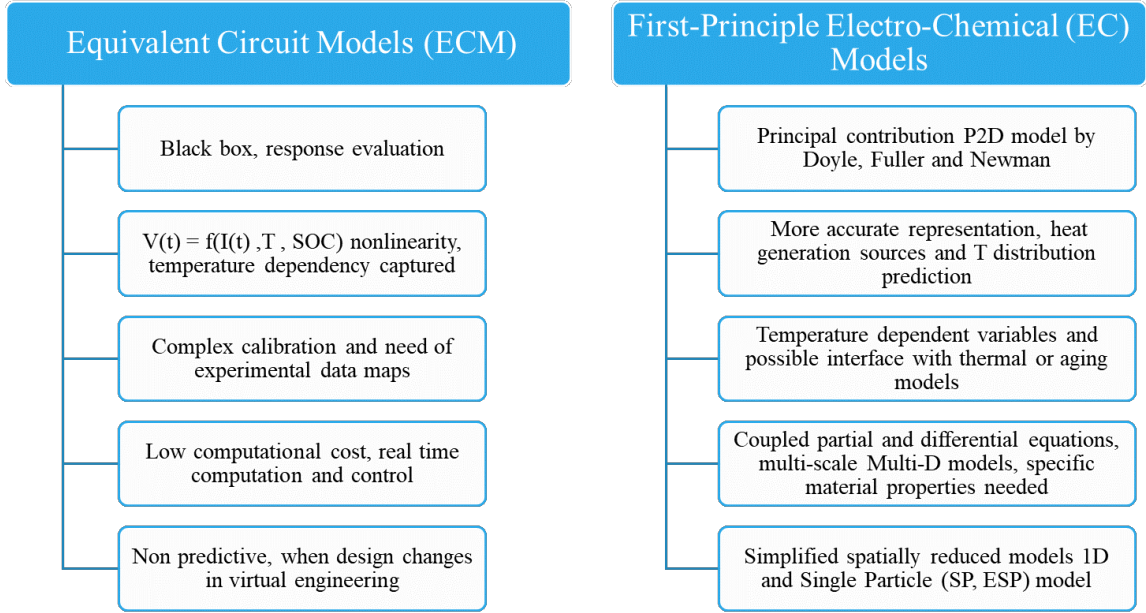


Figure 2.29: ECM against EC models comparison

Dimensional (P2D) electrochemical model for a battery cell [25, 107], Figure 2.30. The model is called also DFN in honor of their developers. Newman itself tested its own model [108]. This is the most used in battery research [104].

This model represents the state-of-the-art for battery electrochemical modeling. Its hypotheses are discussed by other authors over time [109]. The main set equations are still the original ones and every application has its own studies and focus aspects. The main advantage of this model is the accurate description of the battery nature and the high temperature dependency that can be achieved, through its properties. Arrhenius law is one of the possibilities to mathematically describe it. For this reason, the model is typically used for thermal analysis. Since it allows the heat sources characterization once developed to be used for different situations. An additional strength is the possibility to interface it with aging models [109], and the possibility to fully observe its internal states [101]. Its structure can be applied to different cell chemistries and materials. It is worth to say that, starting from the baseline theoretical model, and adapting it to a specific battery chemistry, is not a straightforward activity. It requires deep knowledge of electrochemical parameters and fine-tuning, so lot of recent studies are focused on that. The model and its hypotheses will be explained in the next chapter into detail because this work adopts it.

The P2D model is expressed by nonlinear coupled partial differential and algebraic

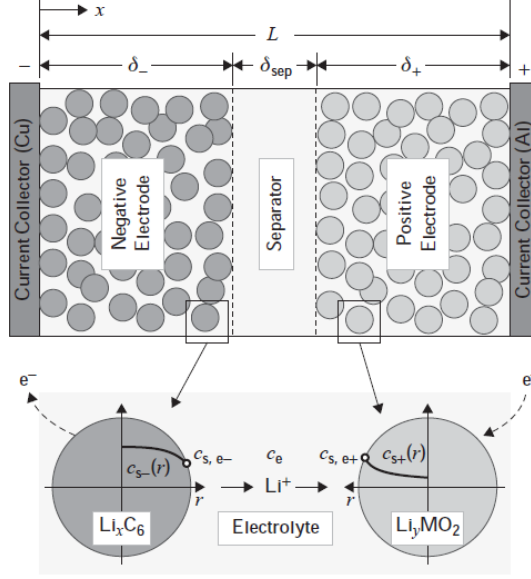


Figure 2.30: P2D model dimensions. Source: [25]

equations PDAEs that needs numerical solution. They are multiscale models and spatially dependent, increasing the mathematical complexity. Generally, they are not suitable for real time applications [101]. Reduced order models, derived from it, are also proposed to lower the computational requirements.

Single Particle (SP) Model

The single particle model (SP) developed by White et al. [26, 110] was firstly adopted for Ni-Mh batteries and then also for Li-ion ones. This reduces the complexity of the P2D model. The solid particles of the electrode are reduced to a single one embedding all the active material, Figure 2.31. This is based on the assumption of uniform electrode utilization which makes the current density only function of time and not also of the thickness. Faster computation makes this model suitable for control and states estimation. This model has some limitations beyond low rates and thin electrodes [111]. They provide more information on internal states with more accurate estimates than simple ECM [101].

Extended Single Particle (ESP) Model

The evolution of the SP model is the extended single particle (ESP) model [112], or improved single particle (ISP) model [113]. The addition is the non-uniform reaction distribution effect and electrolyte concentration and potential distribution which were missing in the SP model [112]. The approximation of concentration profile inside

the particle is polynomial [112] as well as the same for electrolyte and potential distribution inside electrodes [113]. In this way the pore wall flux is captured and this model shows good agreement at high charge/discharge rates (error less than 1% [112, 113]) with reduced simulation times with respect to the P2D one. This is a suitable real time simulation tool that tries to meet the performances of the P2D model, while maintaining the possibility to be implemented in BTMS microprocessors.

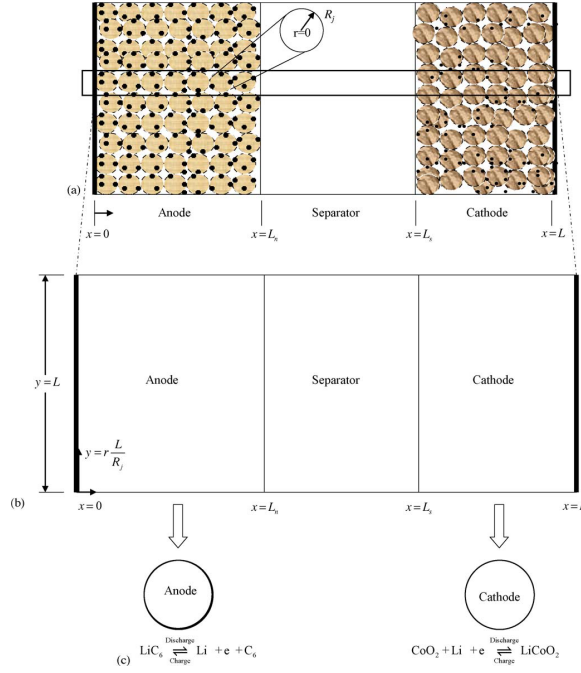


Figure 2.31: Model domain scheme: a) P2D model, b) SP model. Source: [26]

Porous Electrode with Polynomial Approximation (PP) Model

The porous electrode model with polynomial approximation PP, is a reduced order model originating from the P2D model. A parabolic profile approximates the concentration within each electrode spherical particles. It approximates well the P2D model for rates higher than $1C$ [26].

2.4.3 Thermal and Heat Generation Coupling

The thermal aspect was firstly expressed as energy balance in a standalone model of the cell (so called decoupled models). Later, the fundamental need to link it with the battery model was reached, through the electrochemical heat sources and thermal dependent battery variables, to achieve the complete view on Li-ion battery thermal behavior (coupled models).

The first cell global energy balance was developed from the First Law of Thermodynamics by D. Bernardi, E. Pawlikowski and J. Newman [58] in 1985. One of the main hypotheses was that the temperature was independent of the position across the cell (i.e. assumed uniform). The different heat sources from the battery were classified by their nature with a nomenclature which is commonly used until today:

1. **Enthalpy of Reaction** which includes:

- *Polarization Heat*: given by the cell over-potential $(V_{rev} - V)I$ expressing all the main irreversibilities:
 - Ohmic losses,
 - charge transfer over-potential,
 - mass-transfer limitations,
 - electrode over-potential.
- *Entropic Heat*: which is the heat generated by reversible cell operation (entropy change).

The first term is also termed as irreversible heat; as it is caused by the deviation from equilibrium potential, by the effects of the passage of current through the cell electrode-electrolyte pairs (activation over-potential). Reversible heat generation is an alternative name of the second contribution which captures the dependence of the open-circuit potentials with cell temperature (through the Gibbs relations 3.26). Ohmic losses are present both in the solid phase (electrodes) and liquid phase (electrolyte).

- 2. **Enthalpy of Mixing**: which contains heat effects associated with generation, (current passing through the battery during operation), or relaxation, (current stopped), of concentration gradients of Li-ions in the electrolyte. Mixing effects can produce heating or cooling in the battery depending on the specific application.
- 3. **Phase Change heat effects**: if one of the electrodes changes phase during operation.
- 4. Heating effects based on **cell heat capacity changes** with concentration and phase changes. Practically these effects are negligible since the heat capacity has minimum changes during operation.

This energy balance model was coupled with the P2D model, after its development, firstly in [114], to predict the cell temperature. The heat generation from the cell was averaged. The main drawback of this model is that energy balance applies only to the entire cell as a lumped entity; it cannot predict where the heat is generated, inside the cell. The hypothesis of temperature uniformity is motivated by the small Biot (Bi) number of the battery cell. This hypothesis will be studied by other researchers. Botte et al. [115], stated the necessity to model a complete secondary lithium cell including material and energy balance, simultaneously, in more than one dimension, to understand thoroughly complex phenomena like thermal runaway. Due to the complexity of the system, until that moment, the researchers were foreseeing the importance of electro-thermal coupling, but at that time the instruments to handle this multidimensional problem were not enough.

In 1997 Rao and Newman [116], relate heat generation with local variables of a battery cell, like reaction rates, and local OCP against SOC as temperature changes, stating the importance of these local parameters for heat generation. After, Gu and Wang [27] with their work developed another model from FLT capable to demonstrate that temperature-dependent physio-chemical properties, such as the diffusion coefficient, exchange current density and ionic conductivity of the electrolyte, are needed to couple the thermal model with the multi-phase mass transport and electrochemical kinetic model, Figure 2.32. Arrhenius dependence law is adopted and through the activation energy magnitude, is tuned the relative sensitivity of the cell parameter to temperature.

Later models, like proposed by Song and Evans [117], include local heat generation terms and they proved to be accurate including all features of isothermal models. Srinivasan and Wang [118], proved with a 2D coupled local thermal electrochemical study on large aspect ratio cells, that heat generation error, with a uniform temperature hypothesis (lumped thermal model), could be up to 15% at high C-rates. They also specified, that one of the causes could be the importance of considering the reversible heat contribution, at all C-rates, which was neglected in most of the previous analysis. Reversible heat can change sign (due to the nature of the dU/dT against SOC curves), but the overall heat generation is exothermic. Lumped thermal models results in overestimation or underestimation of cell temperature, with different extent, depending on the C-rate. This demonstrates the strong coupled electrochemical-thermal behavior of Li-ion batteries. Some hypotheses included in the first energy balances, like using lumped thermal models, or assuming that heat generation rates, estimated under a particular case, can be used for other situations

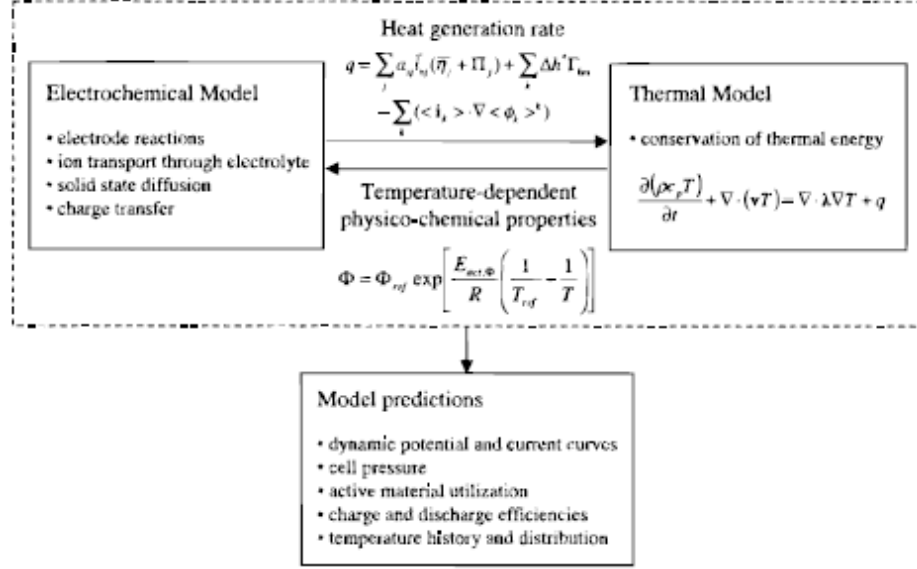


Figure 2.32: Electrochemical-thermal coupling scheme. Source [27]

are weak. Thus, decoupled thermal models with experimental characterization of heat generation sources are not investigated here.

The complexity of the models increased during the years as advanced multiphysics finite element analysis (FEA) software were available. Models are extended in dimension and complexity. For example, Fang et al. [30], include in their research the contact resistance of the current collectors as well as the SEI layer resistance. These resistances cause additional joule heating especially at high C-rates and mainly in the positive electrode.

A simplified modelling approach is to employ the 2D charge balance for the cell, Figure 2.33, coming from the several publications of Kim et al. [28, 37, 119, 120, 121, 122]. These proposed models, due to their hypotheses, are able, with low computational effort, to predict the 2D potential and current distribution of thin batteries (in thin and prismatic pouch cells, the thickness direction is considered uniform for potential and current distribution). They offer the possibility to be coupled to energy balance equations, giving the temperature distribution of the Li-ion battery, with good agreement of the experimental data. Reference [28], points out the importance of considering the battery tabs for non-uniform temperature distribution. Reference [77], employs the same model proving again that the most important effect is the heating effect of the tab rather than the non-uniform heat generation of battery active material. The major limit of this approach is the impossibility to link the heat generation causes to the battery electrochemical nature. In the best case, a sensitiv-

ity analysis on the macroscopic battery thermal parameters could be done, in [77], the in-plane thermal conductivity have been found to have the largest sensitivity in affecting the temperature variation.

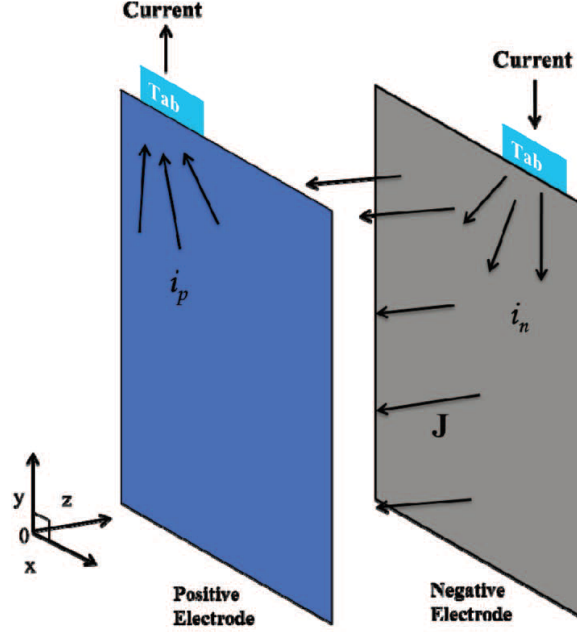


Figure 2.33: 2D charge balance model scheme. Source: [28]

Multi-dimensional electrochemical models are mostly used for research purposes. The most complicated are the 3D electrochemical-thermal models like [31]. These models provide the possibility to exploit local physio-chemical variables and gradients of current and potential in space or time. These results are hard to achieve with experimental or simplified models. This level of complexity comes at high computational cost which is not always required for thermal studies but more useful to study specific phenomena regarding the electrochemical nature. The time required to solve these models prevents them to be used for real time estimation applications.

The complexity of full 3D electrochemical-thermal models is usually reduced. The most adopted approach is to couple the 1D or P2D electrochemical model with a 3D thermal balance. The thermal balance can be lumped, or better, distributed which captures the temperature gradient of the cell. The EC model provides the heat generation sources to the energy balance, which solves the temperature distribution of the battery cell. The temperature information, for that time instant, is fed back to the electrochemistry solver to update the temperature dependent variables during the simulation time, Figure 2.34. This simplified approach maintains the possibility

of classifying the heat generation sources and linking them with their electrochemical cause.

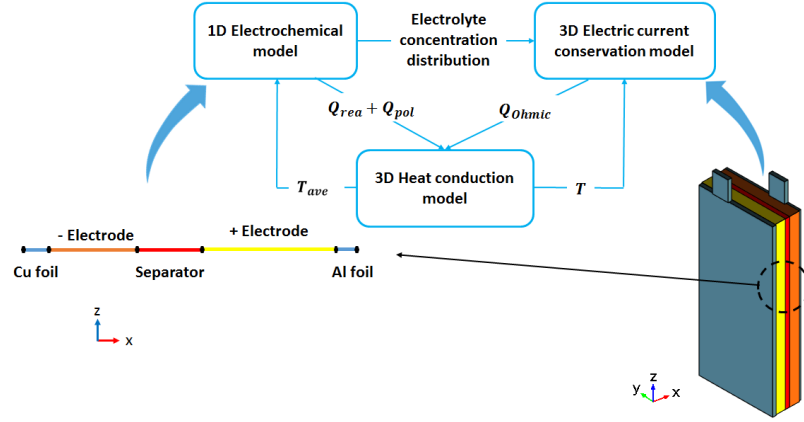


Figure 2.34: One of proposed electrochemical-thermal coupling possibilities. Source: [29]

The electrochemical model along with the distributed energy balance of the cell claims to be the perfect compromise between degree of complexity and fast-time computation. They show good agreement with the experimental data.

Lai et al. [51], used this approach to couple the average heat sources, coming from the electrochemistry, in a 3D heat transfer model for a 10Ah LFP pouch battery cell. They prove that the battery temperature can rise by 18 K under 5C current. The cell temperature goes above 50°C making necessary the existence of a cooling system.

Another example is proposed by Maheshwari [24], with a model for a 6Ah LFP battery cell, coupling the P2D model with a 3D heat equation in COMSOL Multiphysics®. His works proves the asymmetry of heat generation during charge and discharge as well as classifies the Ohmic heat generation as the main component at high discharge rates. He discovers that the negative electrode is the component producing more heat. Similar approaches are adopted by Bahiraei [29], and Ghalkhani [50], for LCO and NCA pouch cells of low capacity (from 4Ah to 16Ah). In addition, they solve the current distribution in 3D. [29] proves that the reversible heat contribution can be both exothermic or endothermic over time. The maximum temperature is found to be near the positive electrode and positive current collector interface, this is caused by the higher current density [29, 50]. [29] presents how electrochemical parameters like particle size, porosity and cathode thickness influence heat generation.

Wu et al. [123], in their derivation for an LMO cell studied the effects of six sets of temperature dependence variables, like the diffusion coefficients and reaction rates

under different conditions up to 12C. At that value, the temperature rise can reach 60°C . The reduction of the thickness of battery components and reducing the active material particle radius improve battery utilization.

Basu et al [45], developed a coupled P2D electrochemical and 3D thermal model for an entire Li-NCA battery pack, with its cooling system. Conduction aluminum elements links the battery cells with the cooling circuit. This system keeps the maximum temperature rise to 7K at high discharge rates.

The example provided by Hosseinzadeh et al. [52] is the state of the art of this modelling approach, studying a high capacity 53Ah NMC cell for automotive applications. Their P2D and 3D thermal coupled model captures the temperature distribution at cell scale and fully explains the variation of cell performance in terms of capacity reduction under different C-rates and temperatures. The thermal gradient can reach up to 35°C at 5C. They are one of the few researchers that fully provide the electrochemical parameters employed.

Chapter 3

Analytical Model

3.1 P2D Electrochemical Model

In this study a pseudo 2D model (P2D) is applied to describe the electrochemical behaviour of the battery. Good accuracy is demonstrated in literature [24, 51, 52], for many battery operating conditions with reasonable computational time. The parametrization is the main challenge however, it offers the ability to capture the main dynamic phenomena taking place in a Li-ion battery cell hence, it is a valuable tool due to its flexibility and modularity that allow the inclusion of thermal and aging models.

The model consists of two interconnected dimensions as represented in Figure 3.1. One dimension is the cell thickness, x , and the additional dimension is r , the particle radius. The main dimension models the charge and mass transport in the electrodes and the electrolyte, as well as the reaction transferring the charge at the electrode-electrolyte interface. The additional dimension allows to solve the diffusion equations inside the particle material, with spherical coordinates.

The model (also called DFN model) and some of its main assumptions are deriving from the electrochemical studies of Newman et. al. [105, 106, 107]. Then some additions have been made through the years (Section 2.4.2). The derivation here will follow the logic scheme of Hariharan et. al. [124], where it is possible to find the complete demonstration of all terms.

Model Assumptions:

- Porous electrode theory [106]: models electrode and electrolyte as a continuous homogeneous media; both liquid and solid phases exist at same time in every point,

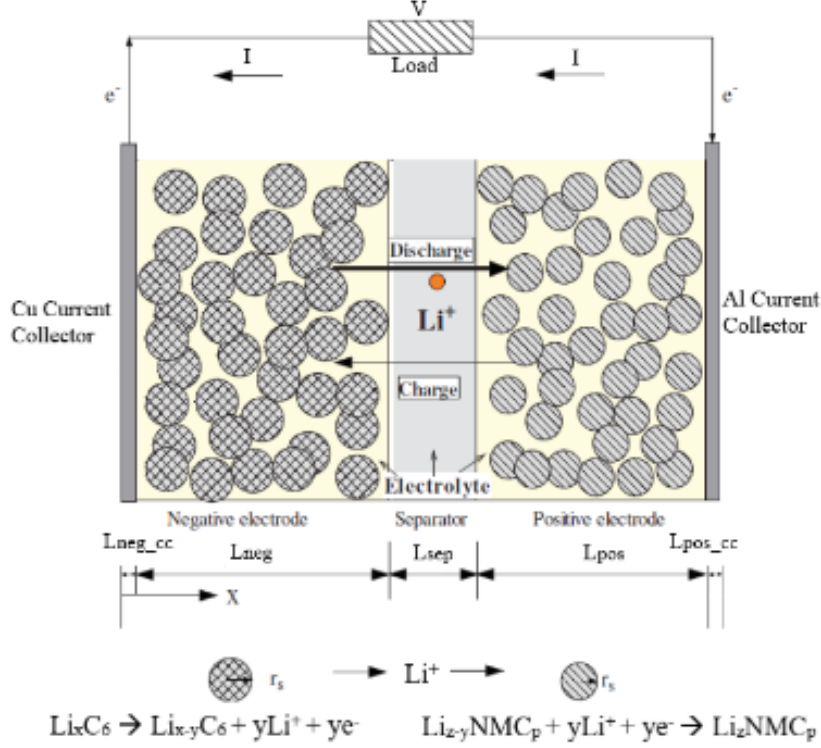


Figure 3.1: P2D electrochemical model geometry scheme, adapted from [30]

- The particles are assumed spherical, due to the adoption of concentrated and porous electrode theory which use spherical coordinates to solve some equations, [25, 105, 107],
- The Li-ions diffuse (mass transport) and migrate (charge transport) hence, mass and charge are conserved simultaneously since the cell is a closed system,
- Concentrated solution theory [105]: the interactions between species of ions, incorporated using their electrochemical potential, includes interactions among all species present in the solution. Furthermore, the activity coefficients of species and solvent are not unity in the multi-component diffusion equation,
- Battery electrochemical description is captured in one dimension, equation variables will be both function of time and of cell thickness (direction x of Figure 3.1). The additional dimension, the particle radius r will be used to solve conservation equations in the solid phase.

As result of the modelling approach, each electrode region is represented by five

equations:

- Mass conservation in solid electrode and liquid electrolyte phase,
- Charge conservation in electrode and electrolyte,
- Coupling charge transfer reaction at the interface between the solid phase of electrode and the liquid electrolyte.

The separator region is represented by two equations: mass conservation and charge conservation for the only present liquid electrolyte.

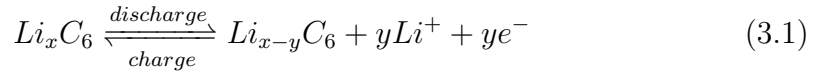
The total set of twelve fully coupled PDE equations characterize the macroscopic electrochemical model of the cell hence, due to the complexity, a numerical approach is necessary to solve the problem.

The model solves for the following variables:

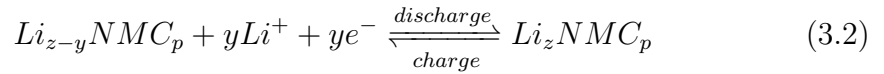
- ϕ_l [V] electrolyte potential,
- ϕ_s [V] electric potential of electrodes,
- c_l [mol/m³] electrolyte salt concentration,
- c_s [mol/m³] solid state Lithium concentration in porous electrodes.

The battery cell under study is a high capacity large pouch cell with NMC/graphite chemistry with $LiPF_6$ salt in EMC solvent. The chemical reactions at the positive and negative terminals are represented as:

- Anode:



- Cathode (generic NMC composition):



3.1.1 Mass Conservation in Solid Electrode

Diffusion in spherical particles takes place after the Li-ion is gained by the solid phase, from the electrode-electrolyte interface charge transfer reaction, becoming neutral. This happens during charge and discharge processes. This phenomenon is described

by Fick's second law of diffusion in spherical particles. Equation 3.3 captures how the Li-ion concentration in the active particles changes over time:

$$\frac{\partial c_{s,i}}{\partial t} = \nabla \cdot (-D_{s,i} \cdot \nabla c_{s,i}) \quad (3.3)$$

Where:

- $c_{s,i}$ [mol/m³], is the concentration of lithium in the solid particles, function of both of time and location,
- $i = p, n$ specifies whether the equation is solved for the positive or negative electrode (notation used in all the thesis document),
- $D_{s,i}$ [m²/s], is the solid phase diffusion coefficient, which is found according to the Stokes–Einstein relation 3.4:

$$D_{s,i} = \frac{k_B T}{6\pi r_{p,i} \eta_{solv}} \quad (3.4)$$

Where:

- $r_{p,i}$ [m], is the positive or negative electrode particle radius,
- η_{solv} [kg/(m · s)] is the solvent viscosity,
- $k_B = 1.38 \cdot 10^{-23}$ [J/K], is the Boltzmann constant,
- T [K], is the absolute temperature.

Expressing the particle radius $r_{p,i}$, Equation 3.3 becomes:

$$\frac{\partial c_{s,i}}{\partial t} = \frac{1}{r_{p,i}^2} \frac{\partial}{\partial r_{p,i}} \left(-D_{s,i} r_{p,i}^2 \frac{\partial c_{s,i}}{\partial r_{p,i}} \right) \quad (3.5)$$

Boundary conditions for this equation are:

- Spherical symmetry at the center of each active material particle results in Equation 3.6:

$$\left. \frac{\partial c_{s,i}}{\partial r} \right|_{r=0} = 0 \quad (3.6)$$

- A continuity condition applies for the concentrations of the solid and the electrolyte phases. At the surface, the flux of Li is given by the pore wall flux (mass

flux, j_i [$mol/m^2 \cdot s$]), given by the charge transfer reaction:

$$-D_{s,i} \frac{\partial c_{s,i}}{\partial t} \bigg|_{r=r_p} = j_i = -\frac{\nabla \cdot i_{s,i}}{F \cdot a_{s,i}} \quad (3.7)$$

Where:

- $i_{s,i}$ [A/m^2] is the solid phase current density, which derives from the diffusion (mass) flux. The fundamental relation between mass flux and current density is the Faraday's Law [105]:

$$n \cdot F \cdot a_{s,i} \cdot j_i = -\nabla \cdot i_{s,i} \quad (3.8)$$

This equation gives the current density due to n electrons flowing through a unit area during a unit time interval. An additional assumption is that no interaction between spherical particles is taken into account, since it is justified by the large distance between them compared to their length scale.

- $a_{s,i}$ [$1/m$] is the specific surface area per unit volume coefficient:

$$a_{s,i} = \frac{4\pi r_p^2 N}{4/3\pi r_p^3 N} \epsilon_{s,i} = \frac{3 \cdot \epsilon_{s,i}}{r_p} \quad (3.9)$$

- $\epsilon_{s,i}$ [–] is the volume fraction occupied by the solid phase of the porous electrode,
- $F = 96485.33289$ [C/mol], is the Faraday constant.

3.1.2 Mass Conservation in Liquid Electrolyte

Starting from the mass flux expression, coming from the solution thermodynamics [124], the mass flux embeds the current flux since the ions are charged particles. Applying the conservation equation to an electrolyte volume fraction and expressing the reaction term through Faraday Law. The total current density is obtained, Equation 3.10, which allows expressing variation of Li-ion concentration in the cell thickness direction:

$$\epsilon_{l,i} \frac{\partial c_l}{\partial t} = \nabla \cdot (D_l \cdot \nabla c_l) - \nabla \cdot \left(\frac{i_l \cdot t_i}{F} \right) + \frac{\nabla \cdot i_l}{F} \quad (3.10)$$

where:

- c_l [mol/m³], is the instantaneous concentration of lithium in the solution phase,
- $\epsilon_{l,i}$ [–], is the electrolyte phase volume fraction (called also porosity), different for positive, negative electrode and separator,
- D_l [m²/s], is the electrolyte diffusivity,
- t_i [–] Li-ion transference number, or transport number which accounts the fraction of the total electrochemical species by a given ionic species and of concentration gradients arising under loads,
- i_l [A/m²], is the current density in the liquid phase.

The first terms on the left of Equation (3.10) accounts for the diffusion phenomena while the right part accounts for the migration effect. In any section of either of the electrodes, the local accumulation of Li-ions concentration and transport due to diffusion is balanced by the rate of formation/dissipation of the charge transfer reaction [125].

To account for the composite nature of the electrode region, the effective diffusivity of the electrolyte is computed from the bulk value in the following manner:

$$D_{l,eff,i} = D_l \cdot \epsilon_{l,i}^b \quad (3.11)$$

Where b is the Bruggeman factor [126], assumed to be 1.5 for both electrodes and the separator [24, 52].

Boundary conditions in this case are:

- Equation 3.36, the charge transfer reaction by itself. It gives the required current density which is the source term, i_l , the Li-ion quantity through solid-liquid interface,
- No Li-ions flux is existing at cell boundaries:

$$\left. \frac{\partial c_l}{\partial x} \right|_{x=L_{neg,cc}} = 0 \quad \left. \frac{\partial c_l}{\partial x} \right|_{x=L_{cell}-L_{pos,cc}} = 0 \quad (3.12)$$

- Continuity of concentrations at negative electrode-separator and separator-positive electrode interfaces:

$$\left. \frac{\partial c_l}{\partial x} \right|_{x=L_{neg,cc}+L_{neg}} = \left. \frac{\partial c_l}{\partial x} \right|_{x=L_{cell}-(L_{pos,cc}-L_{pos}-L_{sep})} \quad (3.13)$$

$$\left. \frac{\partial c_l}{\partial x} \right|_{x=L_{neg,cc}+L_{neg}+L_{sep}} = \left. \frac{\partial c_l}{\partial x} \right|_{x=L_{cell}-L_{pos,cc}-L_{pos}} \quad (3.14)$$

This conservation Equation 3.10, must be solved for the positive and negative electrode. The equation can be simplified for the separator, because the term linked with the charge transfer reaction vanishes and the equation becomes:

$$\epsilon_{l,sep} \frac{\partial c_l}{\partial t} = \nabla \cdot (D_l \cdot \nabla c_l) \quad (3.15)$$

3.1.3 Charge Conservation in Solid Electrode

Current solid phase conservation is ruled by the generalized Ohm's law:

$$i_{s,i} = -\sigma_{s,i} \cdot \nabla \phi_s \quad (3.16)$$

Where $\sigma_{s,i}$ [S/m], is the solid phase electrode (electrical) conductivity, which can be corrected to the effective value, considering porosity effects, with the Bruggeman coefficient:

$$\sigma_{s,eff,i} = \sigma_{s,i} \cdot \epsilon_{s,i}^b \quad (3.17)$$

Faraday's law, Equation 3.8, links the rate of consumption/production of Li-ions with the equivalent current generated. For example, during discharge Li-ions are produced at the negative electrode and consumed at the positive one. Combining Faraday's law with Ohm's law, the solid phase potential can be computed:

$$-\sigma_{s,i} \cdot \nabla^2 \phi_s = F \cdot a_{s,i} \cdot j_i \quad (3.18)$$

Boundary conditions:

- It is assumed that at electrodes-current collectors interface, all current applied i_{app} [A] leaves the cell through the solid particles that are coating the current collector:

$$\left. -\sigma_{s,n} \nabla \phi_s \right|_{x=L_{neg,cc}} = i_{app} \quad \left. -\sigma_{s,p} \nabla \phi_s \right|_{x=L_{cell}-L_{pos,cc}} = i_{app} \quad (3.19)$$

- Instead, at electrodes-separator interface the charge must be transported by the

liquid electrolyte:

$$-\sigma_{s,n} \nabla \phi_s \Big|_{x=L_{neg,cc}+L_{neg}} = 0 \quad -\sigma_{s,p} \nabla \phi_s \Big|_{x=L_{cell}-L_{pos,cc}-L_{pos}} = 0 \quad (3.20)$$

This equation is solved for both electrodes and leads to cell voltage calculation:

$$V_{cell} = \phi_s \Big|_{x=L_{cell}} - \phi_s \Big|_{x=0} \quad (3.21)$$

3.1.4 Charge Conservation in Liquid Electrolyte

The adoption of the concentrated solution theory [105], and mass flux expressions [124] allows to calculate the current balance in case of a binary electrolyte:

$$i_{l,i} = -\sigma_l \cdot \nabla \phi_l + \frac{2 \cdot \sigma_l \cdot R \cdot T}{F} \cdot \left(1 + \frac{\partial \ln f_i}{\partial \ln c_l}\right) \cdot (1 - t_i) \cdot \nabla \ln c_l \quad (3.22)$$

where:

- σ_l [S/m], is the electrolyte solution conductivity, whose effective value can be expressed through the Bruggeman coefficient:

$$\sigma_{l,eff,i} = \sigma_{l,i} \cdot \epsilon_{l,i}^b \quad (3.23)$$

- f_i [-], is the mean molar activity coefficient of the selected domain, which accounts the voltage polarization, (i.e. difference from equilibrium voltage), resulting from gradients of concentration [127]. The quantity $\left(1 + \frac{\partial \ln f_i}{\partial \ln c_l}\right)$, is the thermodynamic factor,
- $R = 8.3145$ [$J/mol \cdot K$], is the universal gas constant.

Boundary conditions pertaining to the electrolyte potential are:

- At electrodes-current collectors interface an insulation boundary condition is imposed, since it is assumed that all current leaves the cell through the solid particles that are coating the current collector:

$$\frac{\partial \phi_l}{\partial x} \Big|_{x=L_{neg,cc}} = 0 \quad \frac{\partial \phi_l}{\partial x} \Big|_{x=L_{cell}-L_{pos,cc}} = 0 \quad (3.24)$$

The above equation is valid for both electrodes whereas in the separator region, all the current goes through the liquid electrolyte (it is the same applied at the cell level) and the equation becomes:

$$I = -\sigma_l \cdot \nabla \phi_l + \frac{2 \cdot \sigma_l \cdot R \cdot T}{F} \cdot \left(1 + \frac{\partial \ln f_i}{\partial \ln c_l}\right) \cdot (1 - t_i) \cdot \nabla \ln c_l \quad (3.25)$$

3.1.5 Charge Transfer Reaction and Thermodynamics Connect

Li-ions are transferred in porous electrodes between the liquid phase (electrolyte) and solid phase (electrodes). Following the full demonstration, which can be found in [124], this reaction is expressed in two components:

- *The equilibrium component*: which relates the open circuit potential (OCP) to the concentration through the Nernst equation,
- *The dynamic component*: ruled by the Butler-Volmer kinetics, which controls the actual reaction, linking the rates with the current (charge) transferred.

The second one is the fundamental relation of battery electrochemistry working principle because it regulates the cell behavior.

Equilibrium Component

The fundamental quantity, linking electrochemistry to thermodynamics, is the Gibbs energy, defined as:

$$G = H + TS \quad (3.26)$$

Substituting the enthalpy definition and applying the second law of thermodynamics for a constant temperature and pressure process, the following is obtained:

$$\Delta G = \Delta H - \Delta(TS) = P\Delta V - \Delta W_{rev} \quad (3.27)$$

Analyzing the right side of the equation, the meaning of Gibbs energy represents the net non-expansion work, which in a Li-ion battery cell, it is the electrical work. Hence, the relation between equilibrium potential and Gibbs energy is obtained:

$$G = -nFV_0 \quad (3.28)$$

In which, V_0 [V] is the equilibrium potential value, and n [-] is the number of transferred electrons.

In addition, for electrochemical systems, the change in concentration affects the Gibbs energy, through:

$$\Delta G = \Delta G(0) + RT \ln \frac{c_P}{c_R} \quad (3.29)$$

where P stands for products and R for reactants.

Combining Equation 3.28, and Equation 3.29, the Nernst expression is obtained:

$$V_0 = V_0(0) + \frac{RT}{nF} \ln \frac{c_P}{c_R} \quad (3.30)$$

This fundamental relation between the open circuit potential with the concentration is necessary to obtain the dynamic component expression.

Dynamic Component

Li-ions intercalate or de-intercalate from the liquid to the solid phase of the porous electrode. The reactant is reduced and the product is oxidized hence, the net rate of reaction determines if the overall process is oxidation or reduction, resulting in the net current density:

$$i = Fk_a c_p - Fk_c c_r = Fj_a - Fj_c = i_a - i_c \quad (3.31)$$

where:

- i_a, i_c [A/m^2], are the anodic and cathodic current densities,
- k_a, k_c [m/s], are the anodic and cathodic reaction rates constants.

The reactions are triggered by thresholds of internal energy, at a given temperature, embedded in the reaction constants so, Equation 3.31 is modified and becomes:

$$i = Fk_{0,a} \exp\{-\Delta G_a/RT\} c_P - Fk_{0,c} \exp\{-\Delta G_c/RT\} c_R \quad (3.32)$$

where the insertion of anodic and cathodic charge transfer coefficients quantifies the extra electrical work, required to reach the Gibbs energy threshold, from the initial energetic state, for forward and reverse reaction [124], ($\alpha_c = \alpha$ & $\alpha_a = (1 - \alpha)$):

$$i = Fk_{0,a} \exp\{(1 - \alpha)F\Delta\phi/RT\} c_P - Fk_{0,c} \exp\{(\alpha)F\Delta\phi/RT\} c_R \quad (3.33)$$

At equilibrium, the net current is zero because both current densities have equal

magnitude. They are termed as exchange current density:

$$i_0 = Fk_{0,a} \exp\{(1 - \alpha)F\Delta\phi/RT\}c_{P,EQ} - Fk_{0,c} \exp\{(\alpha)F\Delta\phi/RT\}c_{R,EQ} \quad (3.34)$$

Substituting in here the Nernst equation, Equation 3.30, to account concentration differences as potential varies, and considering a local equilibrium, the final Butler-Volmer kinetics expression is obtained for the current density flux:

$$\nabla \cdot i_i = a_{s,i} \cdot i_0 \left[\exp\left(\frac{\alpha_a \cdot F \cdot \eta}{R \cdot T}\right) - \exp\left(\frac{-\alpha_c \cdot F \cdot \eta}{R \cdot T}\right) \right] \quad (3.35)$$

The equation is solved for both electrodes such that:

- i_i [A/m^2], is the current density passing through the solid-liquid interface,
- $\alpha_a = (1 - \alpha)$ $[-]$ and $\alpha_c = \alpha$ $[-]$ are the anodic and cathodic charge transfer coefficients respectively, which express the preference of the overall reaction balance toward the anode or the cathode [24],
- $\eta = \phi_s - \phi_l - E_{eq}$ $[V]$, is the surface over-potential which captures the difference of the actual voltage from the equilibrium one,
- i_0 [A/m^2], is the exchange current density, which could be expressed as:

$$i_0 = Fk_c^{\alpha_a} k_a^{\alpha_c} \cdot (c_{s,max,i} - c_{s,i})^{\alpha_a} \cdot c_{s,i}^{\alpha_c} \cdot c_{l,i}^{\alpha_a} \quad (3.36)$$

in which $(c_{s,max,i} - c_{s,i})$ [mol/m^3], expresses the variation of unoccupied sites with respect to the maximum possible, $c_{s,max,i}$, that regulates the reaction.

The charge transfer equation, Equation 3.35, is the fundamental relation to explain the electrochemical nature of the battery cell. The charge transfer coefficients, along with the reaction rates are ruling the overall battery kinetics. They are one of the most influencing parameters, together with diffusion coefficients so, attention is dedicated to them in the model calibration. In simulation environment, adopted by several works, the reaction rates are tuned to match the experimental results.

3.2 3D Distributed Thermal Model

A 3D distributed energy balance is adopted to distinguish between the various sources of heat generation inside the battery components. The lumped balance captures only

the temperature rise, omitting its origin. The input volumetric heat sources are coming from the battery P2D model then only a spatial thermal balance is required to obtain the temperature distribution. The derivation presented in this thesis is close to the ones in [27, 58, 124], but summing up, and defining the key aspects that may create confusion, obtaining a clear division of the different heat sources. Following the demonstration in [124], the initial focus is on the charge transfer reaction at solid electrode/liquid electrolyte particle interface, which produces most of the heat. The total heat generated at the interface, called Butler-Volmer Heat is expressed in both electrodes by:

$$q_{BV} = Fj_i [\eta_i + \Pi_i] \quad (3.37)$$

where:

- The first term is the product of the current density by the overpotential, (difference between solid and liquid phase potential from the equilibrium), driving the reaction. This is an exothermic reaction, hence an irreversible heat contribution,
- The second term represents the Peltier effect, for which, when there is a change of current conducting material, heat can be generated or retrieved. This is termed reversible contribution and it will depend whether the cell is charging or discharging. With the applications of nonequilibrium thermodynamics concepts (Onsager-DeGroot method) it is possible to link the Peltier coefficient Π_i [V], with entropy, and through Gibbs energy, arrive to potential variations. For this reason, this term is also called Entropic heat.

Therefore, the following equation is obtained:

$$q_{BV} = Fj_i \left[\eta_i + T \frac{\partial V_{0,i}}{\partial T} \right] \quad (3.38)$$

with:

$$\Pi_i = T \frac{\Delta S_i}{nF} \quad \Delta S_i = nF \frac{\partial V_{0,i}}{\partial T} \quad (3.39)$$

Hereafter, to obtain volumetric heat generations (heat generation per unit volume Q_i [W/m³]), all the heat sources in q_i [W/m²] needs to be multiplied by the surface to volume ratio coefficient $a_{s,i}$ [1/m].

The second component is obtained in its final form after applying Faraday's equation to account for the current:

$$Q_{rev} = Fa_{s,i}j_iT \frac{\partial V_{0,i}}{\partial T} = -\nabla i_s T \frac{\partial V_{0,i}}{\partial T} \quad (3.40)$$

This term includes reversible entropy changes depending on the open circuit potential derivative with temperature, also known as entropy coefficient. This contribution can switch from exothermic or endothermic during the same discharge [24, 29, 50]. Beyond the charge transfer reaction, the second contribution is the Ohmic heat generation due to the current conduction in solid electrodes and liquid electrolyte. Ohmic heat is another part of the irreversible heat. Starting from the mass flux conduction equation, applying the Gibbs-Helmholtz equation:

$$\Delta H = nFT^2 \frac{dV_{0,i}}{dT} \quad (3.41)$$

$$H = -T^2 \frac{\partial}{\partial T} \left(\frac{\mu}{T} \right) = \mu - T \frac{\partial \mu}{\partial T} \quad (3.42)$$

Substituting the value of the chemical potential μ [V] gives the final form of the Ohmic heat, where the gradient of the potential is multiplied by the current density:

$$Q_{Ohm} = -i_{l,i} \cdot \nabla \phi_l - i_{s,i} \cdot \nabla \phi_s \quad (3.43)$$

The separator will include the only contribution due to the liquid phase. Furthermore, the tabs Ohmic contribution is added analytically to the thermal balance, since these components are not included in the 1D electrochemical model but they provide a non-negligible contribution in the total cell heat generation:

$$Q_{Ohm,tab,i} = \frac{(R_{tab,i} + R_{c,i}) \cdot i_{app}^2}{V_{ol,tab,i}} \quad (3.44)$$

where:

- i_{app} [A] is the total current applied to the cell during its discharge,
- $V_{ol,tab,i}$ [m^3] is the volume either of the positive or negative tab,
- $R_{c,i}$ [Ω] is the contact resistance, which accounts both internal tab-cell contact and external-internal tab contact resistances,
- $R_{tab,i}$ [Ω] is the tab resistance, obtained as:

$$R_{tab,i} = \frac{\rho \cdot L}{A_{\perp}} = \frac{\rho_{tab,i} \cdot w_{tab}}{L_{i,cc} \cdot h_{tab}} \quad (3.45)$$

– $\rho_{tab,i}$ [S/m] is the resistivity either of the positive or negative tab material,

- $w_{tab} [m]$ is the length of the tab in the current conduction direction,
- $L_{i,cc} [m]$ is the thickness of the tab of the positive or negative tab material which is taken as the current collectors thickness,
- $h_{tab} [m]$ is the base of the cross section that along with $L_{i,cc}$ is crossed by the current entering or exiting the cell.

Some positive electrodes have the possibility to undergo a phase transition. The heat generated is quantified through the enthalpy difference of the two phases undergoing the reaction. This is called equivalent enthalpy approach [124]:

$$Q_{pt} = \Delta H_{\alpha\beta} \cdot \dot{\eta}_{\alpha\beta} \quad (3.46)$$

$$\dot{\eta}_{\alpha\beta} = \frac{\dot{r}_i^{\alpha \rightarrow \beta}}{r_{p,i}} = \frac{1}{r_{p,i}} \frac{dr_i^{\alpha \rightarrow \beta}}{dt} \quad (3.47)$$

where:

- $r_i [m]$ quantity is the interface position that is expressed through the moving boundary model [128], in the equation,
- $\Delta H_{\alpha\beta} [J]$ is the equivalent enthalpy obtained through calorimetry experiments. NMC positive electrode has the tendency to develop phase transitions phenomena, but due to the required knowledge of the exact complex reaction, to quantify the material changing phase and lack of experimental data to characterize $\Delta H_{\alpha\beta}$, this term is neglected in this study.

The last contribution is the heat of mixing, that accounts molecular fluxes, generating heat due to concentration gradients [105]:

$$Q_{mix} = -j_i \cdot \left(-F \frac{E_{eq,therm}}{dc_{s,i}} \nabla c_{s,i} \right) = \frac{\nabla \cdot i_s}{Fa_{s,i}} \cdot \left(-F \frac{E_{eq,therm}}{dc_{s,i}} \nabla c_{s,i} \right) \quad (3.48)$$

Finally, the complete energy conservation equation for the battery cell is obtained:

$$\rho C_p \frac{\partial T}{\partial t} = Q_{cond} + Q_{conv} + Q_{irrev} + Q_{rev} + Q_{mix} + Q_{Ohm,tab} \quad (3.49)$$

In which:

$$Q_{cond} = k \nabla^2 T \quad (3.50)$$

$$Q_{cond} = -\nabla h(T - T_{amb}) \quad (3.51)$$

$$Q_{irrev} = -i_s \nabla \phi_s + -i_l \nabla \phi_l - \nabla i_s (\phi_s - \phi_l - V_0) \quad (3.52)$$

$$Q_{rev} = -\nabla i_s T \frac{\partial V_{0,i}}{\partial T} \quad (3.53)$$

$$Q_{mix} = \frac{\nabla \cdot i_s}{F a_{s,i}} \cdot \left(-F \frac{E_{eq,therm}}{d c_{s,i}} \nabla c_{s,i} \right) \quad (3.54)$$

$$Q_{Ohm,tab} = \frac{(R_{tab,i} + R_{c,i}) \cdot i_{app}^2}{V_{ol,tab,i}} \quad (3.55)$$

Where:

- The first term in Equation 3.49 is the net energy rate of the battery cell,
- k [$W/m \cdot K$], is the thermal conductivity of the pouch battery cell,
- ρ [kg/m^3], is the composite density of the pouch battery cell,
- C_p [J/kgK] is the composite cell heat capacity under constant pressure,
- The heat transfer modes are conduction inside the battery cell, since the cell is made by porous materials. Convection with the external environment boundary condition is applied, because the cell is the only object in a test chamber, and not in contact with other cells. h [$W/(m^2 \cdot K)$], the heat transfer coefficient will vary case by case.

This equation is both space and time dependent. Boundary conditions will be discussed first in the coupling paragraph and then in the application section.

3.3 Electrochemical-Thermal (ECT) Coupling

As constantly stressed out, it is necessary to capture the electrochemical as well as thermal components of the battery nature to achieve a proper thermal prediction and guarantee the battery optimal temperature range. The approach used in this study is reported in Figure 3.2. Initially the different volumetric heat sources are computed in the 1D P2D electrochemical model, they are classified by typology as presented in the previous paragraph and also by geometrical domain (electrode, separator, current collectors). For every time instance these heat sources are given as input variables to the 3D energy balance, which solves the heat transfer study to obtain simultaneously

the temperature magnitude and distribution of the battery cell. The fundamental distinction from the previous research approaches is that, in this work all the different heat sources are not summed and averaged over the total battery volume, but kept distinguished by typology and spatially also in the 3D model. The contribution of current collectors is also inserted. The strong temperature dependency of some battery physio-chemical properties must be included to obtain a fully coupled thermal model. The average value of the temperature on the battery volume is sent as feedback to the temperature dependent (non-isothermal) electrochemical model, to allow the update of these parameters, prior to recalculate the heat generation of the following instants. In this work these properties are:

- Reaction rate constants,
- Diffusion coefficient of solid electrode phases,
- Diffusion coefficient of the electrolyte phase,
- Electrolyte ionic conductivity,
- OCP vs Temperature derivative of anode and cathode materials (entropy coefficient),
- Thermodynamic factor (anion transference number), which accounts the fraction of the total electrochemical species by a given ionic species.

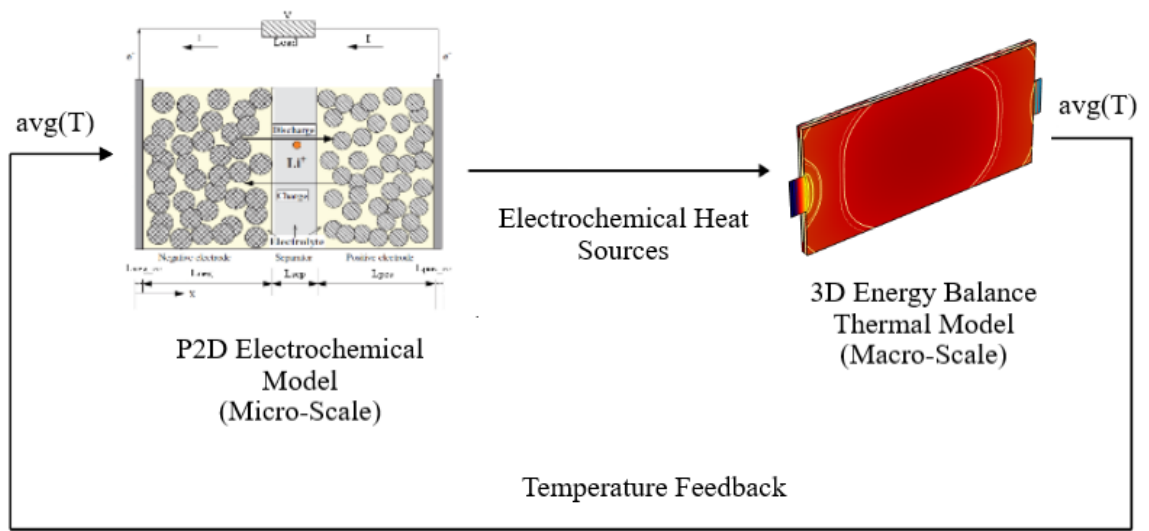


Figure 3.2: Coupling scheme and enabling quantities between the modeling dimensions

Chapter 4

Parametrization and Model implementation in COMSOL Multiphysics [®]

The coupled P2D electrochemical-3D thermal model developed has the objective to describe the physical laws of Li-ion battery cells being flexible, reliable and accurate with respect to the empirical approaches. The simplification and division of the two parts allows faster computational times with lower CPU requirements with respect to a fully 3D electrochemical-thermal model. The complexity of the equations still requires numerical techniques such as finite element analysis (FEA) with volume averaging technique. The actual implementation details of the model in COMSOL Multiphysics[®] v5.5 and some important aspects regarding electrochemical and thermal parameters are explained in this chapter. There are approximately 30 input parameters, (Appendix A), for the electrochemical model, so this parametrization activity requires significant effort that will be reflected in the final model. The temperature dependency of some key electrochemical parameters is investigated. The cell under study is a high capacity large pouch cell with NMC/Graphite chemistry with $LiPF_6$ salt in EMC solvent. The following model's initial development is fine-tuned to match the experimental data coming from an OEM's tests on the cell. Note that for reasons of confidentiality all the plots with sensible data have the values in the axes and values of parameters removed. The electrochemical part is validated with the experimental data regarding the cell isothermal discharge curves at different C-rates and temperatures. The thermal part is also reproducing the test conditions of non-isothermal discharge for a cell in a controlled temperature chamber. The choice for every detail worthy of explanation is backed up by literature and company data,

for each specific section in the following. Some starting values are modified during the calibration process.

4.1 Cell Materials

Cell materials are known but their specific properties are not always available from manufacturers, the actual cell materials are reproduced with materials available in COMSOL Multiphysics[®] library and the known specific properties are substituted in COMSOL Multiphysics[®] to fit the experimental data, always double-checking with the available literature as explained later for each specific parameter. The positive electrode is made with NMC chemistry, standard NMC 1/3 ($LiNi_{1/3}Mn_{1/3}Co_{1/3}O_2$) proportion is used due to lack of information company-wise and from the limited literature. The exact chemical composition is pretty difficult to reproduce often for the presence of binders, additives, to enhance the conductivity and to favor the power configuration of this cell. The phase change of positive electrode material can also occur but here is not included for the lack of quantitative data. The anode is reproduced by a standard Li_xC_6 graphite anode from COMSOL Multiphysics[®] material library. Also, in this case, secret additives from the manufacturer can be used to enhance the high power configuration of this cell. The liquid electrolyte is represented by standard $LiPF_6$ salt in EMC, PC, EC solvent, available in the software. The positive current collector and internal tab as well as the negative internal tab and current collector are made of different electrically and thermally conductive materials. The same applies for the external tabs. Properties of these materials are widely known, being highly conductive materials with low resistance. The current collectors distribute the current to the active cell materials whereas the tabs are the external links for the electrical connections of the cell.

4.2 Electrode Balancing

A reverse engineering procedure with an optimization study is adopted for the electrode balancing, to compute the amount of active Li-ion material necessary in the cell. The full explanation and the COMSOL Multiphysics[®] application used to do this can be found in [129]. In a battery cell, the amount of active material at anode and cathode must be the same, to not add dead weight to the battery or to limit the performance of the electrode. When starting from a balanced situation the proper cell OCV can be obtained because there is no way to compensate it with diffusion

coefficients, reaction rates and conductivities. This application is implemented for charge behavior and the Author has adapted it for discharge electrode balancing. At start of discharge, the negative electrode is fully lithiated while the positive electrode is unlithiated, while at complete discharge the situation will be reversed. The important remark is that the electrodes are containing more Li than the strict necessary, for safety reasons. The extra material is used for situation of high C-rates or for some phenomena like the initial SEI layer formation on the anode, during the first discharge cycles. Over time, as the battery ages, the amount of cyclable lithium is reduced.

Four parameters are needed to define the balancing model:

1. $Y_{host,pos}$ [—], is the dimensionless amount of positive electrode host material. Dimensionless parameters are defined with respect to the nominal capacity of the cell Q_{cell} [Ah]:

$$Y_i = \frac{Q_{Li,i}}{Q_{cell}} \quad (4.1)$$

2. $Y_{host,neg}$ [—], is the dimensionless amount of negative electrode host material,
3. $Y_{Li,tot}$ [—], is the dimensionless amount of Li in the battery cell,
4. $SOL_{neg,0,DOD}$ [—], is the electrode state of lithiation (SOL), at the start of the discharge (i.e. depth of discharge $DOD = 0$). It is called also local SOC when is defined with concentrations:

$$SOL_i = \frac{Q_{Li,i}}{Q_{host,i}} = \frac{c_{s,i}}{c_{s,max,i}} \quad (4.2)$$

These four values are starting from a standard set of numbers known and common for cells, which are known as function of SOL. Moreover, additional info are required:

- OCV experimental curve of the cell during discharge,
- OCV experimental curve of the ositive electrode (NMC) during discharge,
- OCV experimental curve of the negative electrode (Graphite) during discharge.

These curves are available for the specific cell in consideration. The COMSOL Multiphysics[®] optimization solver estimates the final value of the four initial parameters with a least squares method minimizing the objective function, which is the

difference of the computed cell OCV (positive electrode OCV – negative electrode OCV) with respect to the experimental wanted OCV:

$$O = \sum (E_{cell,model} - E_{cell,exp})^2 \quad (4.3)$$

The results for this specific cell are the four optimized values with Figure 4.1 and Figure 4.2, from where it is possible to obtain the amount of active Li-ion material in the cell:

$$SOL_{pos,0,DOD} = \frac{Y_{Li,tot}}{Y_{host,pos}} - \frac{SOL_{neg,0,DOD} \cdot Y_{host,pos}}{Y_{host,neg}} \quad (4.4)$$

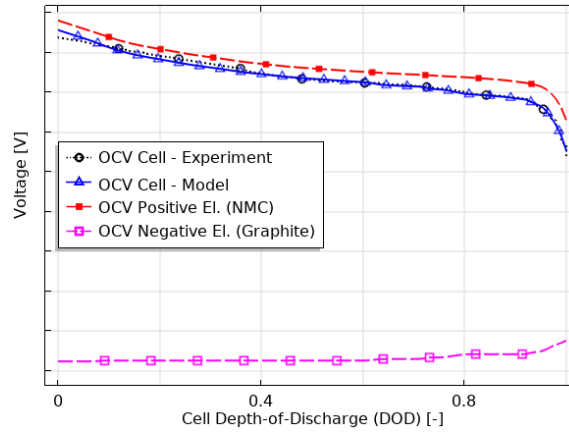


Figure 4.1: Electrode balancing equilibrium voltage curves for the cell under study

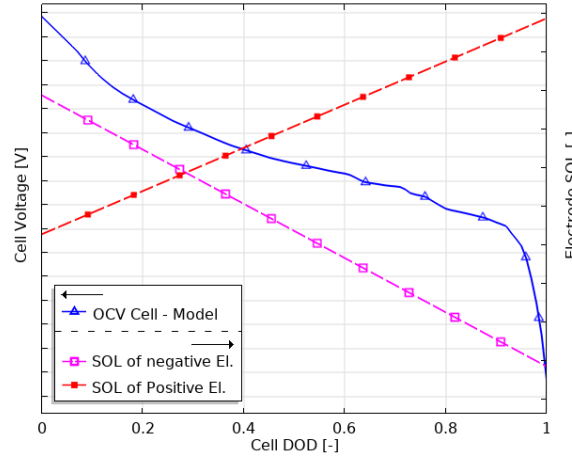


Figure 4.2: SOL of electrodes during discharge for the cell under study

The excess capacity necessary, in the negative electrode to avoid Li-plating, leading

to cell short circuit, is:

$$f_{loss} = \frac{1 - SOL_{neg,0,DOD}}{SOL_{neg,0,DOD} - SOL_{neg,100,DOD}} \quad (4.5)$$

The initial lost capacity in the negative electrode due to initial SEI formation reactions is:

$$f_{excess} = \frac{Y_{host,pos} - Y_{Li,tot}}{Y_{host,neg}} \quad (4.6)$$

The initial Li-ions concentrations in the solid electrodes at the start of discharge are also obtained:

$$c_{s0,neg} = SOL_{neg,0,DOD} \cdot c_{s,max,neg} \quad (4.7)$$

$$c_{s0,pos} = SOL_{pos,0,DOD} \cdot c_{s,max,pos} \quad (4.8)$$

where the maximum amount of Li-ions in the electrodes is $c_{s,max,pos} = 49000 \text{ [mol/m}^3\text{]}$ and $c_{s,max,neg} = 31507 \text{ [mol/m}^3\text{]}$ from the software material library. Similar values can be found in [52, 130, 131].

In addition, the solid phase volume fractions of the electrodes can be calculated, leading to obtain the hosted capacity of each electrode:

$$\epsilon_{neg} = \frac{Y_{host,neg} \cdot Q_{cell}}{F \cdot c_{s,max,neg} \cdot L_{neg} \cdot A_{cell}} \quad (4.9)$$

$$\epsilon_{pos} = \frac{Y_{host,pos} \cdot Q_{cell}}{F \cdot c_{s,max,pos} \cdot L_{pos} \cdot A_{cell}} \quad (4.10)$$

$$Q_{host,neg} = F \cdot \epsilon_{neg} \cdot c_{s,max,neg} \cdot L_{neg} \cdot A_{cell} \quad (4.11)$$

$$Q_{host,pos} = F \cdot \epsilon_{pos} \cdot c_{s,max,pos} \cdot L_{pos} \cdot A_{cell} \quad (4.12)$$

where $A_{cell} \text{ [m}^2\text{]}$ is the electrode active material cross sectional area. The anode area is used as cell reference, as it is the lowest value, hence limiting the performance of the whole cell. $L_{neg} \text{ [m]}$ and $L_{pos} \text{ [m]}$ are the thicknesses of the electrodes. To verify, the host capacity is multiplied by the SOL range of each electrode, hence obtaining the actual capacity corresponding to Q_{cell} :

$$Q_{actual,i} = Q_{host,i} \cdot (SOL_{i,0,DOD} - SOL_{i,100,DOD}) \quad (4.13)$$

This method uses an interpolation based on the OCP curves of the materials and the wanted OCV of the cell, leading to the values of local state of charge inside the electrodes (local amount of Li that gives the desired voltage, which is not arriving to 0% or 100%) and the porosity of electrodes (amount of active material of solid and liquid phase). No electrochemistry is involved here, so all these values will be fine-tuned in the P2D model calibration.

4.3 Physio-Chemical Properties

All the model parameters, are experimental results coming from the cell teardown or obtained from studying the literature for similar cell configurations, as presented for each value. More sources are compared to see whether the values were reliable. Some others parameters are usually fine-tuned for each specific cell, to reach a good agreement with the experimental data. Overall, the parameters are double-checked again in the final model calibration, and changed if necessary. The complete list can be found in Appendix A.

Bruggeman coefficient - 1.5 for all domains, which is adopted by several authors [29, 50, 52, 126]. Assumptions for this value will be compensated by diffusivity and conductivity values [24].

Equilibrium potentials (OCP) curves of the electrodes - Experimental data were available both for the positive and negative electrode. The standard interpolation curves of COMSOL Multiphysics® materials were substituted with the real ones (see Figure 4.1). It is worthy to say, that this is a fundamental data for a correct modelling prediction as it has a significant effect on simulation results. The literature regarding the NMC electrode open circuit potential curves is very limited, due to the novelty of the material, so the experimental data coming from the GITT test at 25°C are preferred. However, they are similar to [65] which studies similar materials.

Electrical conductivity - Electrical conductivity is also called electronic conductivity of the material. Graphite negative electrode has a conductivity of 100 [S/m] measured by many studies, [24, 30, 123]. As positive electrode conductivity is taken 100 [S/m] due to the lack of data regarding the NMC chemistry. However, since studies of other chemistries presented lower estimates [24, 30, 123], values from 5 [S/m] to 100 [S/m] were tested with no significant changes. Taking the same value of the

negative electrode assures that this is not a limiting factor as the current rate changes [24, 50]. Electrical conductivities of Aluminum and Copper domains are straightforwardly obtained by the materials, respectively $3.774 \cdot 10^7$ [S/m] and $5.998 \cdot 10^7$ [S/m] [50, 77]. In this study constant values are taken, only the electrolyte ionic conductivity will be temperature dependent.

Particle radius of electrodes - Constant particle radius is adopted in this model, $r_{p,pos}$ & $r_{p,neg}$ [m], as many previous papers were doing with similar values [31, 52, 123]. In reality the particle radius varies in a range like as implemented by [24] but lack of experimental data were preventing this.

4.4 Temperature Dependent Properties

As introduced in previous discussions, to capture the temperature dependency of some key electrochemical properties, the Arrhenius Law is the common mathematical way used to describe this relation. Equation 4.14, is the law for a generic parameter ψ :

$$\psi = \psi_{ref} \exp \left[\frac{E_{act,i}}{R} \left(\frac{1}{T_{ref}} - \frac{1}{T} \right) \right] \quad (4.14)$$

where:

- $E_{act,i}$ [J/mol], is the activation energy, fundamental to regulate the temperature sensibility of the specific parameter,
- ψ_{ref} is the value under study at $T_{ref} = 298.15$ [K]($25^\circ C$), reference ambient temperature, the for this work.

The standard Arrhenius Law is not always enough for capture the temperature dependency of all parameters, so each one needs its specific attention and calibration. Below, all parameters will be listed in the order that it was discovered mostly influencing the model. The parameters with more influence are listed first.

Reaction Rates Constants

Reaction rate constants are needed, as explained in the theory part, to describe the charge transfer reaction. Both the negative and positive electrode reaction rate constants are described by the Equation 4.15:

$$K_i = K_{0,i} \exp \left[\frac{E_{act,K,i}}{R} \left(\frac{1}{T_{ref}} - \frac{1}{T} \right) \right] \quad (4.15)$$

Where:

- $E_{act,K,neg} = 20000 [J/mol]$ [52], $E_{act,K,pos} = 30000 [J/mol]$ [30], are the negative and positive electrode activation energies for the reaction rate constants. They have been tested successfully for the desired working range of the model.
- $K_{0,neg} [m/s]$, $K_{0,pos} [m/s]$ are the negative and positive reaction rates at reference temperature. Their value is obtained fitting the correct exchange current density value to approximate the experimental isothermal discharge curve of the cell at $25^\circ C$.

For both the electrodes this property is temperature dependent as explained in [24, 29, 46, 50, 123]. Advanced concentration dependencies of the positive electrode rate constant with the local SOC and with the exponential elevated at power of 2, [31, 52], are tested here, but not adopted, since they were not providing any benefit to the model.

Values of the reaction rates constants are comparable to the aforementioned literature studies in the order of 10^{-9} or $10^{-10} [m/s]$. It was determined that each specific cell modeled has its own characteristic constants to reach a good approximation of the experimental data. Literature values are a good starting point and reference but they usually require calibration. This consideration is valid also for the following parameters.

Solid Phase Diffusion Coefficient

The electrodes diffusion coefficient has a huge importance on the overall cell behavior, as it rules the cell diffusion mechanism. This coefficient along with the reaction rate constants, which control the charge transfer reaction, is one of the key parameters affecting the cell discharge performances. As a result, the temperature dependence is also fundamental to be correctly captured.

For the negative electrode diffusion coefficient, the temperature variation is expressed through the standard Arrhenius Law: [24, 30, 46, 123]:

$$D_{s,neg} = D_{s,0,neg} \exp \left[\frac{E_{act,Ds,neg}}{R} \left(\frac{1}{T_{ref}} - \frac{1}{T} \right) \right] \quad (4.16)$$

For the positive electrode, the standard Arrhenius expression was not enough to capture the temperature dependency. A correct fitting was found using a square exponential part, like a study with a similar composition [52]. The electrodes diffusion

coefficient is also modeled as concentration independent (opposite as presented by [31]) since this addition is tested to be no more precise:

$$D_{s,pos} = D_{s0,pos} \exp \left[\frac{E_{act,D_{s,pos}}}{R} \left(\frac{1}{T_{ref}} - \frac{1}{T} \right) \right]^2 \quad (4.17)$$

where:

- $E_{act,D_{s,neg}} = 68025.7 [J/mol]$, $E_{act,D_{s,pos}} = 3409 [J/mol]$, are the negative and positive electrode activation energies for the reaction rates, obtained for a correct temperature dependency as temperature changes,
- $D_{s0,neg} = 1.4523 \cdot 10^{-12} [m^2/s]$, $D_{s0,pos} = 8.5 \cdot 10^{-14} [m^2/s]$ are the negative and positive electrodes solid state diffusion coefficients reference temperature. Also, their value is obtained by fitting the correct exchange current density value to approximate the experimental isothermal discharge curve of the cell at $25^\circ C$.

It is worthy to mention that the activation energy of the positive electrode is not valid for all temperatures. For example, it was determined from calibration studies that $E_{act,D_{s,pos}} = 27980 [J/mol]$ is needed to describe the cell discharge voltage under $10^\circ C$ correctly. Due to the complex additional phenomena, rising when the Li-ion batteries work at low temperatures, a dedicated model for low temperature range is needed to capture the proper behavior as in [43, 69, 75].

Liquid Phase Diffusivity

The liquid electrolyte diffusion coefficient (diffusivity) is strongly depending on the electrolyte salt and solvent composition. The main components of the liquid electrolyte are known, namely $LiPF_6$ salt in EMC, PC, EC solvent. However, their exact composition is not known for this application. So, the temperature and concentration dependency of this parameter is approximated, starting with temperature dependence in COMSOL Multiphysics[®] material library. An electrolyte with the same constitutive materials but not the exact volume percentage is selected as follows:

$$D_l = D_{l,0} \cdot \left(10^{\left(-4.43 - \frac{54}{\left(T - 5e^{-3} \cdot \left(\frac{c_2}{c_{ref}} \right) - 229 \right)} - 0.22e^3 \cdot \frac{c_2}{c_{ref}} \right)} \right) \quad (4.18)$$

where:

- $c_{ref} = 1,000,000 \text{ [mol/m}^3\text{]}$ is the reference electrolyte concentration for this quantity,
- $D_{l,0} = 1e^{-3} \text{ [m/s]}$, is the multiplicative constant, which is changed from the original one for a better fit of the experimental data,
- $c_2 = \min(3900, \max(c_l, 7.7e^{-3})) \text{ [mol/m}^3\text{]}$ from the COMSOL[®] definition,

The obtained quantity is concentration and temperature dependent, and similar expression leading to comparable values is found in [31, 127].

Electrolyte Ionic Conductivity

Many authors takes into account both temperature and concentration as variables influencing the ionic conductivity σ_l , [24, 29, 31, 52, 123]. The standard temperature and concentration dependence in COMSOL Multiphysics[®] material library for this parameter is found to be satisfactory, for this study. This is possible since the electrolyte is made with the same material of the real one. The specific composition is unknown as previously explained.

Entropy Coefficient

The entropy coefficient or temperature derivative of the electrode open circuit potential plays a fundamental role in defining the temperature dependency of the electrode potentials OCP, previously explained, especially in a non-isothermal discharge. The relation is expressed by:

$$E_{eq,i}^T = E_{eq,i} - (T - T_{ref}) \cdot \frac{dE_{eq,i}}{dT} \quad (4.19)$$

where

- $E_{eq,i}^T \text{ [V]}$ is the electrode potential at temperature T ,
- $E_{eq,i} \text{ [V]}$ is the reference electrode potential at temperature $T_{ref} = 298.15 \text{ [K]}$, (see 4.1),
- $\frac{dE_{eq,i}}{dT} \text{ [V/K]}$ is the entropy coefficient.

Adopted entropy coefficients are reported in Figure 4.3. Both for the positive NMC and negative graphite electrodes, experimental values of the same chemistry reported in [65] are adopted, due to a lack of specific data on the cell studied. The NMC entropy coefficient is very similar to the standard COMSOL Multiphysics[®] one and the graphite value is near to the one used in [24, 132].

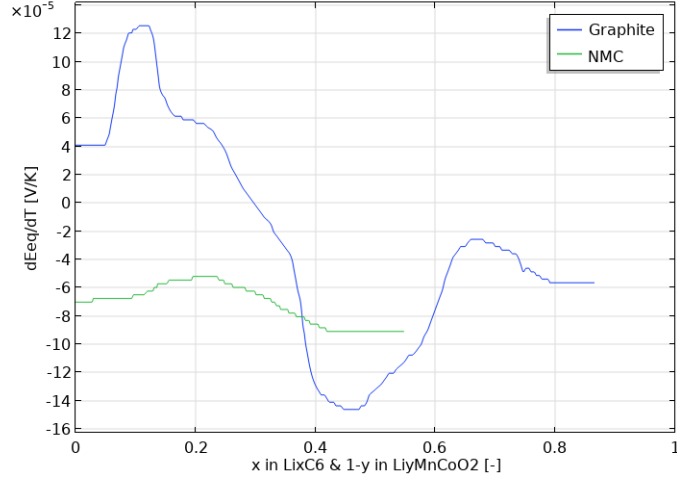


Figure 4.3: Entropy coefficients of electrodes

Activity Dependence of Electrolyte (Thermodynamic Factor)

The standard temperature and concentration dependence in COMSOL Multiphysics[®] material library for this parameter is tested and found to be satisfactory in this study. The electrolyte activity dependence $\frac{\partial \ln f_i}{\partial \ln c_l}$ is part of the thermodynamic factor $\left(1 + \frac{\partial \ln f_i}{\partial \ln c_l}\right)$. In addition to the experimental discharge curve validation, the specific expression is checked, and it is similar to [127] which studies a similar electrolyte. The transport number t , needed in the activity dependence computation (called also Li transference number), is obtained by a concentration dependent function, and for this quantity values are similar to [127].

4.5 Pouch Cell Thermal Parameters Estimation

The simplified 3D energy balance gives the possibility of giving lumped thermal properties at cell level. All cell's fundamental units are constantly repeated, obtaining a constant different materials layers' repetition in the total cell. Considering the cell with general properties coming from the single layers is an acceptable assumption that will be also confirmed in the comparison with the full 3D model, where each layer is kept with its own properties. However, the thermal properties are anisotropic for the three directions of the 3D thermal model, if obtained at the cell level.

Single thermal properties of each domain are not easy to find in literature. A summary for this model is reported in Table 4.1. For additional validation, the calculated values for the pouch cell, reported in Table 4.2, are also compared to the

available literature as follows:

Thermal Conductivity

Thermal conductivity is anisotropic due to the presence of several layers in the cell assembly. In the layers parallel direction this parameter is expressed by Equation 4.20, namely, in-plane thermal conductivity. Instead, the through-plane thermal conductivity is expressed by Equation 4.21:

$$K_{cell,\parallel} = \frac{(L_{neg,cc} \cdot K_{neg,cc} + L_{neg} \cdot K_{neg} + L_{sep} \cdot K_{sep} + L_{pos} \cdot K_{pos} + L_{pos,cc} \cdot K_{pos,cc})}{L_{cell}} \quad (4.20)$$

$$K_{cell,\perp} = \frac{L_{cell}}{\left(\frac{L_{neg,cc}}{K_{neg,cc}} + \frac{L_{neg}}{K_{neg}} + \frac{L_{sep}}{K_{sep}} + \frac{L_{pos}}{K_{pos}} + \frac{L_{pos,cc}}{K_{pos,cc}} \right)} \quad (4.21)$$

where:

- $K_{neg,cc} = 398$ [W/mK] and $K_{pos,cc} = 238$ [W/mK], are the standard thermal conductivities used for copper and aluminum current collectors and tabs, used also in [24, 29],
- $K_{neg} = 4.21$ [W/mK], is used as negative electrode thermal conductivity. A range of values is identified from [123, 133], but is adopted [123], which accounts the mixed nature of LiC_6 soaked in the electrolyte,
- $K_{sep} = 1.21$ [W/mK], for the separator value is also used [123] value which considers the electrolyte presence. Similar value is used in [133],
- $K_{pos} = 0.95$ [W/mK], starting from the specific measurements of [134, 135], is estimated as positive electrode thermal conductivity, comparing the values for the total cell $K_{cell,\parallel}$, $K_{cell,\perp}$ (Table 4.2) to the available studies. Values obtained here are similar to [24, 52, 77, 131, 133], remarking the reliability of the study presented.

Density

The cell density is obtained from the values of its components available in Table 4.1 and it is reported in Table 4.2. The value is obtained through:

$$\bar{\rho}_{cell} = \frac{\sum_i \rho_i \cdot L_i}{L_{cell}} = \frac{(L_{neg,cc} \cdot \rho_{neg,cc} + L_{neg} \cdot \rho_{neg} + L_{sep} \cdot \rho_{sep} + L_{pos} \cdot \rho_{pos} + L_{pos,cc} \cdot \rho_{pos,cc})}{L_{cell}} \quad (4.22)$$

where:

Table 4.1: Thermal Properties of Different Layers

Property	Unit	Negative Current Collector	Negative Electrode	Separator	Positive Electrode	Positive Current Collector
Thermal Conductivity	$[W/(mK)]$	398	4.21	1.21	0.95	238
Density	$[kg/m^3]$	8700	1861	1043	1428.34	2700
Heat Capacity	$[J/(kgK)]$	385	845	1688	900	900

Table 4.2: Pouch Cell Thermal Properties

Pouch Properties	Value	Unit
Cell Thickness	10	$[mm]$
In-plane Thermal Conductivity	30.043	$[W/mK]$
Through-plane Thermal Conductivity	1.697	$[W/mK]$
Density	1853.2	$[kg/m^3]$
Heat Capacity	987.01	$[J/kgK]$

- $\rho_{neg,cc} = 8700 [kg/m^3]$ and $\rho_{pos,cc} = 2700 [kg/m^3]$, are the densities of copper and aluminum current collectors and tabs, respectively, also used in [24, 29],
- $\rho_{neg} = 1861 [kg/m^3]$, for the negative electrode. Density values ranges from 1247 $[kg/m^3]$ to 5000 $[kg/m^3]$ [29, 50, 123]. [123] is chosen since it considers the electrolyte contribution,
- $\rho_{sep} = 1043 [kg/m^3]$, for the separator is also used in [123], which considers the electrolyte presence. Similar value is used in [133],
- $\rho_{pos} = 1428.34 [kg/m^3]$, is estimated as positive electrode density, comparing the values for the total cell ρ_{cell} , (Table 4.2) to the available studies. The values available for the single material were mainly referring to NMC electrode powders [136, 137, 138], with higher values, not accounting the electrolyte presence. However the cell density is in accordance with [24, 52, 130] and checked also with the battery tear-down data at the cell level (Table 4.2).

Heat capacity

The last of the cell main thermal properties is also computed, starting from the layers materials, Table 4.1, and compared with literature data both at material and cell level, following:

$$\overline{C}_{p,cell} = \frac{\sum^i C_{p,i} \cdot L_i}{L_{cell}} = \frac{(L_{neg,cc} \cdot C_{p,neg,cc} + L_{neg} \cdot C_{p,neg} + L_{sep} \cdot C_{p,sep} + L_{pos} \cdot C_{p,pos} + L_{pos,cc} \cdot C_{p,pos,cc})}{L_{cell}} \quad (4.23)$$

where:

- $C_{p,neg,cc} = 385 [J/kgK]$ and $C_{p,pos,cc} = 900 [J/kgK]$, are the heat capacities of copper and aluminum current collectors and tabs, respectively, used also in [24, 77],
- $C_{p,neg} = 845 [J/kgK]$, for the negative electrode heat capacity. Values range from 845 [J/kgK] to 1437 [J/kgK] [29, 50, 123, 139]. Value in [123] is chosen because it accounts the electrolyte contribution in this case,
- $C_{p,sep} = 1688 [J/kgK]$, for the separator, is also used [123], which provides the electrolyte effect. Similar value is used in [51],
- $C_{p,pos} = 900 [J/kgK]$, estimated starting from 700 [J/kgK] to 950 [J/kgK] range [24, 123], comparing the values for the total cell $C_{p,cell}$, (Table 4.2) to the available studies [24, 52, 77, 131, 140, 141].

4.6 P2D Electrochemical Modelling Details in COM-SOL Multiphysics®

Prior to start, attention must be paid to the geometry approach of the model. Several investigations [29, 41, 46, 50, 93, 130] include the study of battery modules and packs, but as the reader will see in the following, even the model of a single cell is not easy to understand.

The P2D electrochemical model describes a fundamental unit of the cell in its thickness direction, the highlighted part in Figure 4.4. With this term, called also stack, is described an assembly consisting of half of negative current collector, negative electrode (one anode side, because the electrodes are double coated), separator, positive electrode (one side) and half of positive current collector. Clearly, as explained in the introduction and literature review, only one stack cannot satisfy the cell capacity

nent two, which is just the battery geometry with its heat sources.

The electrochemical model is developed independently for its better control and trouble-shooting, hence, an error in the thermal balance will not affect the validity of the electrochemical model. The model is developed to work in a temperature range from 10°C above. Isothermal discharge curves will firstly have obtained to validate the model against the experimental data of the single cell tests. The model is validated at three temperatures and for each temperature, four different C-rates are simulated, to reproduce nominal, slow and fast discharge behaviors. After adding the thermal component, the coupled model is tested during non-isothermal discharges at different rates and with different heat transfer boundary conditions.

The electrochemistry is implemented through the Lithium-Ion Battery interface of COMSOL Multiphysics[®] which allows to take into account all the modelling details explained in the theoretical part. It is a pre-build environment with all the parts of the P2D model developed by Newman et al. [25, 107]. The list of required parameters for the coupled model is available in Appendix A. The electrochemistry description falls under the *Component one* as can be seen by COMSOL Multiphysics[®] model builder, where all the nodes referring to the electrochemistry are included 4.5. This is a 1D model, solving the electrochemical variables, defined in the theory part, along the cell thickness and over time. The additional dimension inside the particle, is discretized to fully solve the diffusion law in the electrode solid phase, as the DFN model requires. However, the cross sectional area of the cell A_{cell} [m^2] is given as a fixed parameter to the software so the volumetric heat generations can be computed. Equations are solved in one direction only, which is the battery thickness z , so variation of EC variables in the other two directions are not captured. This is due to the hypothesis that the battery thickness z is the main direction in where the reactions are occurring. This hypothesis will be validated through the results analysis. Materials of the model are the one included in the Section 4.1.

The important nodes as presented in Figure 4.5 are:

- **Porous electrodes** is where the intercalation and charge transfer reaction takes place. All the main electrochemical parameters are assigned while distinguishing between the electrodes and electrolyte (e.g. reference concentrations, local SOC, reference exchange current densities and others). The particle dimension is discretized in 10 elements along the radial direction. The exchange current density, here, is referred to a reference concentration, so Equation 3.36

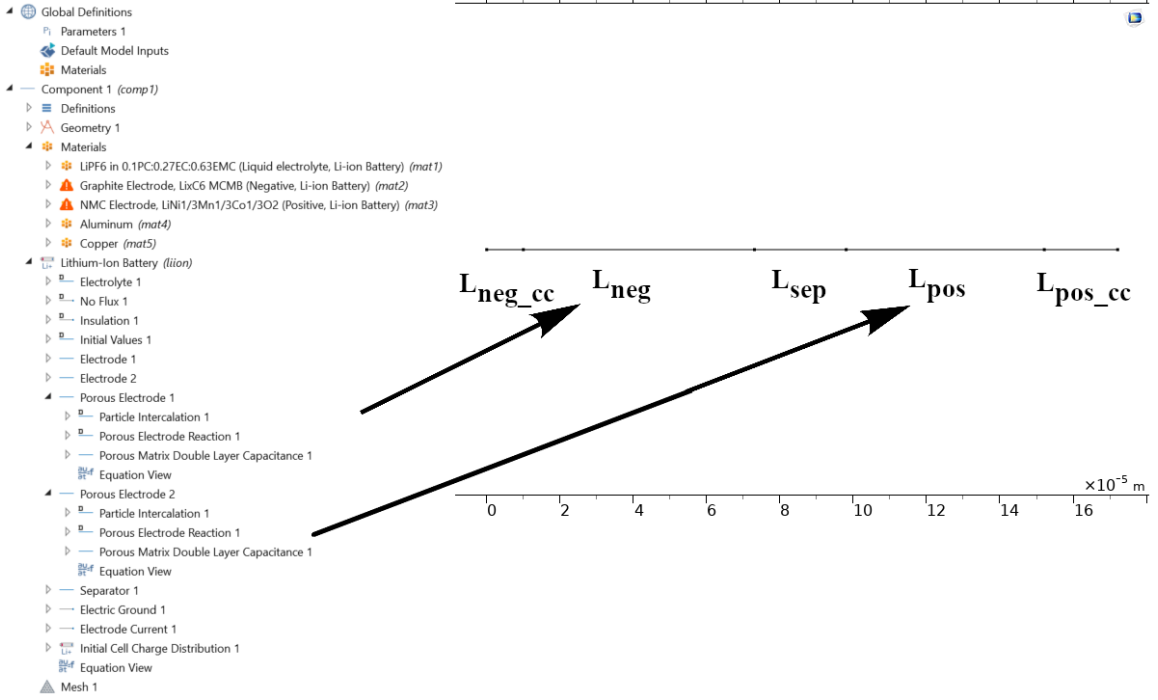


Figure 4.5: *Component one* model builder and geometry in COMSOL Multiphysics®

is modified in:

$$i_0 = i_{0,ref}(T) \left(\frac{c_{s,i}}{c_{s,i,ref}} \right)^{\alpha_c} \cdot \left(\frac{c_{s,max,i} - c_{s,i}}{c_{s,max,i} - c_{s,i,ref}} \right)^{\alpha_a} \cdot \left(\frac{c_{l,i}}{c_{l,i,ref}} \right)^{\alpha_a} \quad (4.24)$$

in which:

- $c_{s,i,ref} = \frac{c_{s,max,i}}{2}$ [mol/m³] taken as reference concentration,
- The reference exchange current density is usually obtained by experimental procedures, which in this case are missing, it is approximated as:

$$i_{0,ref,i} = K_i \cdot F \cdot \frac{c_{s,max,i}}{2} \quad (4.25)$$

This is possible since the underestimation or overestimation of this value, is corrected by the calibration of the temperature dependent reaction rate constant K_i , which is a parameter that requires specific fine-tuning for each cell, but its order of magnitude can be compared with previous studies found in the literature [24, 52], as explained in section 4.4.

- **Electrode nodes** are identifying the current collectors (they are also electrodes

but not porous with active Li inside) with their material properties.

- **Boundary conditions** are the implementation of the theoretical boundary conditions explained in the analytical model (see Figure 4.6):
 - No flux at the boundaries: since Li-ions are not travelling in the current collectors because the charge is carried by the electrons there,
 - Electric Ground: where the negative current collector is grounded,
 - Electrode Current: where the discharge current i_{app} [A] is applied to the battery cell,
 - Initial values and Initial Cell Charge Distribution are required nodes to give the initial potential, the starting SOC and the cell capacity to the software. The cyclable Lithium lost f_{lost} , and the lithium in excess f_{excess} , of the negative electrode calculated through the electrode balancing are inserted here.

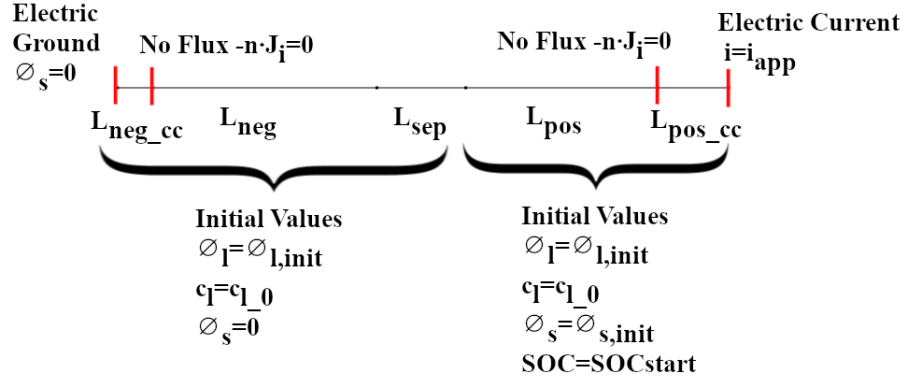


Figure 4.6: EC boundary conditions for the 1D cell model in COMSOL Multiphysics®

4.7 Thermal Model Implementation and Details in COMSOL Multiphysics®

The component two in this modelling approach, Figure 4.7, is the one that represents the external cell geometry. Different approaches are used to study this thermal part while the electrochemistry will be always the same. These different models, presented hereafter, will be still considered simplified approaches (with respect to the fully

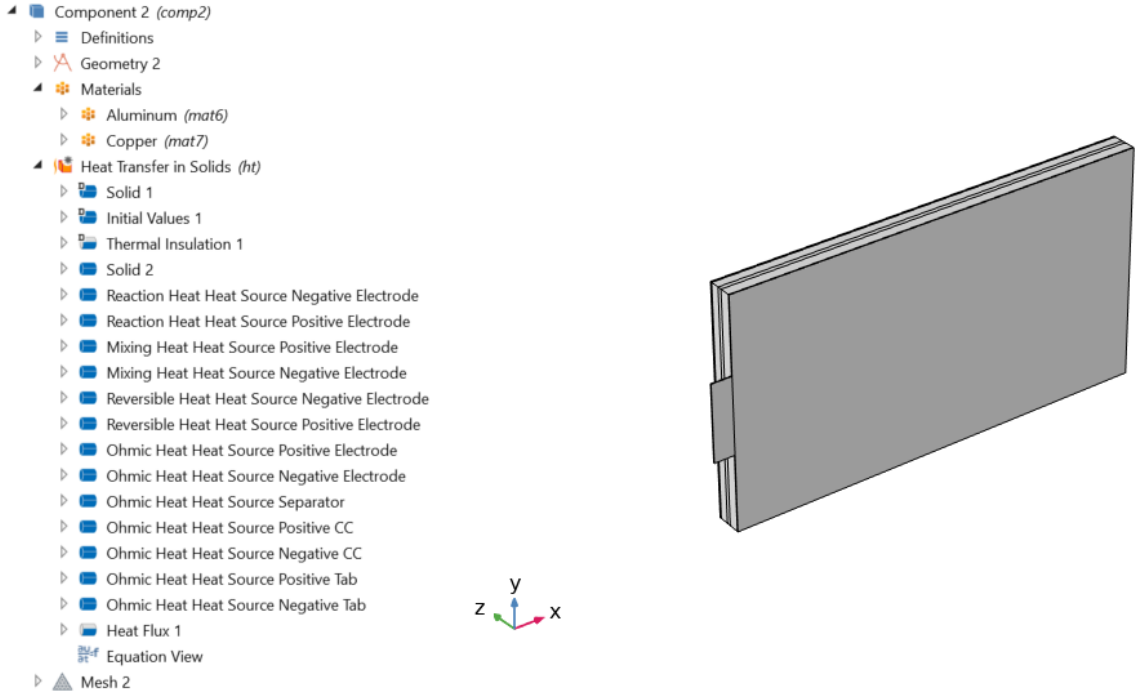
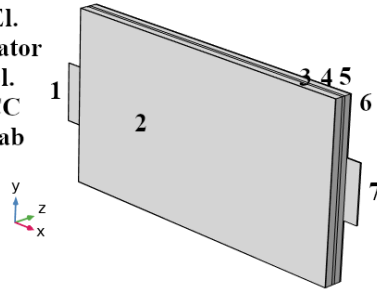


Figure 4.7: *Component two* model builder and geometry in COMSOL Multiphysics®

coupled 3D ECT model), because they represent the cell with the use of two coupled but distinguished components, one for the electrochemistry and one for the thermal balance which is different in each case:

1. **Cell fundamental unit model:** one stack of the cell is considered from the thermal point of view, as shown in Figure 4.8. The layered frame has the different heat sources coming from the electrochemistry calculations, keeping them separate domain by domain and by heat typology (reversible, irreversible and Ohmic), as categorized in the theory 3.2 part: e.g. the reversible reaction heat of the positive electrode calculated from the electrochemical model (*Component one*) is given as volumetric heat source to the positive electrode domain, in the *Component two*. The heat generation from internal tabs of the layer and the current collectors are included. The detailed computation procedure is explained in the next section. Thermal properties of each material are assigned to the layers.
2. **Complete cell model with total average heat source and lumped properties:** in this variant, the complete external dimensions of the cell are taken into account as shown in Figure 4.9. The cell envelope is obtained repeating the

1. Neg. Tab
2. Neg. CC
3. Neg. El.
4. Separator
5. Pos. El.
6. Pos. CC
7. Pos. Tab



1. Neg. Ext. Tab
2. Active Material
3. Cover Material
4. Pos. Ext. Tab

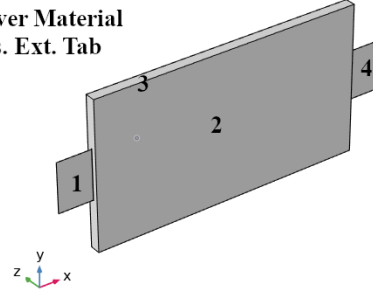


Figure 4.8: 3D model of the funda- Figure 4.9: 3D model of the com-
mental unit geometry in COMSOL[®] plete cell with average heat strategy
in COMSOL[®]

fundamental unit N_{stacks} [—] times, as the complete cell. However, the layers division is omitted due to the hypothesis adopted. Since the repeated single layers are in the order of $[\mu m]$, to approximate their overall thermal properties, only a total active material volume is taken into account, Figure 4.9, with lumped values derived from the single layers as explained in section 4.5. This is done to simplify the computational burden with respect to more complex descriptions as the next model. In this situation only the external cell tabs are included and also the thin layer $[\mu m]$ covering the pouch cell (termed as non-active battery material) is modeled. In this situation, only the average total heat source on the battery active volume is included in the thermal model since the layer domains are no more captured. This is the classical approach used by many researchers [24, 51], because it is the most suitable solution to build battery modules and packs, while assuring an acceptable detail at the cell level.

3. **Complete cell model with distributed heat sources for each layer and lumped properties:** this is the most detailed approach amongst the simplified models. N_{stacks} [—] fundamental units with their layered structure, will be repeated to reproduce the stacked structure of the complete cell resulting in the jellyroll, Figure 4.10. Heat sources will be given as input, analog as the approach number one, but assigned to all the present layers of the same kind (e.g. N_{stacks} [—] positive electrodes, with each its heat source). All the cell internal tabs are connected in parallel through a horizontal connecting element, which in turn is in electrical contact with the two external tabs of the cell.

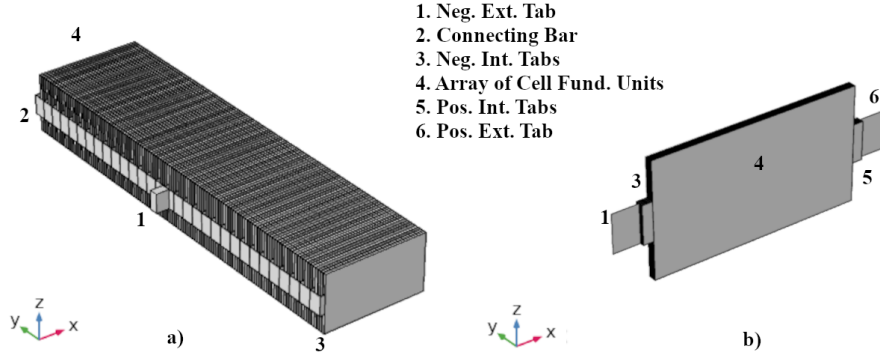


Figure 4.10: 3D complete cell model with all the layers repetition in COMSOL Multiphysics®: a) Scale=100 on y axis b) No scale

All the different heat sources, along with the heat transfer boundary conditions, will enable the 3D thermal balance calculation, obtaining the history of temperature evolution and its gradient on the battery cell. The enabling tool is the heat transfer node of COMSOL Multiphysics®. The boundary conditions for the electrochemical-thermal simulation will be the same for all the three models to have a meaningful comparison between the different approaches. Two C-rates are tested, representing: the non-isothermal discharge under nominal current and fast discharge. The different domains are defined as a solid object with their properties. To do that solid nodes of COMSOL Multiphysics® heat transfer module are used.

Thermal boundary conditions:

- All the electrochemical heat sources are inserted in the solid 3D geometry as volumetric heat sources [W/m^3]. In addition, dedicated heat sources are used for tabs and current collectors,
- Conduction is the mode of heat transfer inside the battery, while convection is the mode of heat transfer between the battery and the surrounding environment. To account for the second phenomena, a convective heat flux node is used. The heat transfer set up is made to reproduce a condition of battery testing for which experimental data is used as guidelines. The cell is inserted in a controlled environment chamber where it is undergoing a constant current discharge, repeated at different rates. The experimental guidelines refer to a constant and controlled ambient reference temperature of 298.15 [K] ($25^\circ C$), which is also the starting temperature of the cell. The battery cell is exposed to the convective flux on all sides. To reproduce it, the first test adopts natural convection, then, a forced

air cooling is simulated on the battery surface. $h = 7 [W/m^2K]$ represents the natural convection regime, usually a range from 5 to 10 $[W/m^2K]$ is used as natural convection heat transfer coefficient [24, 31, 51, 52, 133, 142]. Amongst all, 7 $[W/m^2K]$ is chosen as it is the one that better approximates the reference data regarding the temperature rise of the cell, since the actual experimental data does not provide this value. For forced air cooling $h = 25 [W/m^2K]$ is selected [139, 142, 143, 144, 145].

4.8 Coupling Strategy in COMSOL Multiphysics®

To realize the coupling explained in Section 3.3, it is necessary to manually couple the two components through the linking variables in the software. The principal heat sources of Section 3.2 are automatically embedded and calculated, inside the Li-ion Battery Interface of COMSOL Multiphysics®. The only one which is not computed alone is the Ohmic heat of the different domains, which is manually computed and included inside the local variables node of the *Component one* (the full table describing the variables of the *Component one* is available in the Appendix A). Equation 3.43 is used that translated in COMSOL Multiphysics® language is:

$$Q_{Ohmic,i} = -phil \cdot liion.il - phis \cdot liion.is \quad (4.26)$$

where:

- $phil$ and $phis$ [V] are the derivative of the liquid and solid phase potential respectively: ϕ_l and ϕ_s [V] of Equation 3.43,
- $liion.il$ and $liion.is$ $[A/m^2]$ are current density of the liquid and solid phase respectively: $i_{l,i}$ and $i_{s,i}$ $[A/m^2]$ of Equation 3.43.

In the *second Component*, all the heat sources coming from the electrochemistry are reported in the local variables of component two, to be used as general heat sources through the dedicated nodes of the heat transfer module. They are averaged on the respective domain of the *Component one* and inserted successively as heat source of the *Component two*. To clearly explain the procedure one heat source computation is explained in detail here (the rest is following the same reasoning and they can be found in the Appendix A, which contains all the local variable of the *Component two*):

$$Q_{h,Ohmic,sep} = comp1.aveop3(comp1.Q_{ohmic_sep}) \quad (4.27)$$

Where the COMSOL Multiphysics[®] language finds its mathematical explanation as:

- $Q_{Ohmic,sep}$ [W/m^3] is the Ohmic heat of the separator computed from the component one (inserted in the local variables of *Component one* as explained before) and follows Equation 3.43:

$$Q_{Ohmic,sep} = -i_l \cdot \nabla \phi_l \quad (4.28)$$

- *aveop3* is the COMSOL[®] command which calculates the integral of the selected quantity over the selected domain. In this case Q_{ohmic_sep} over domain $n^\circ 3$ which is the separator itself. After it divides by the domain characteristic dimension:

$$Q_{h,Ohmic,sep} = \frac{\int Q_{Ohmic,sep} dl}{l} \quad (4.29)$$

In this case the characteristic dimension is the length of the domain 3, which is the separator, Figure 4.5. The characteristic dimension is a length because the component is 1D, but can be also an area (2D component) or volume (3D component).

Given the heat sources, the heat transfer module computes the heat balance, thus leading to the temperature distribution on the cell volume. Its average value over the *Component two* (*aveop* on domain 7) is used as model input, in the shared properties of the *Component one* as:

$$T_{input} = nojac(comp2.aveop7(comp2.T)) \quad (4.30)$$

The fed-back average temperature of Equation 4.30, allows the Li-ion battery node of the *Component one* to update the temperature dependent electrochemical variables of section 4.4, to capture the variables evolution for the next time steps.

The mesh of the cell will be a rectangular mapped mesh on one face of the cell which will be swept in the battery thickness direction. For the simpler models, a finer tetrahedral mesh is used, since the memory requirements along with computational time are still acceptable.

After the initial current distribution initialization, a time dependent study is used to solve the non-isothermal electrochemical thermal coupled problem. Due to the presence of two physical phenomena, a segregated approach is adopted by the time dependent solver (direct MUMPS solver with 0.001 relative tolerance). In the same

time step, firstly the EC variables needed for the heat sources computation are solved. Once they are obtained, the heat transfer model is solved, which leads to the temperature value of the *Component two* and its surface distribution. This temperature value will update the electrochemical variables for the next step. Depending on the wanted level of detail the time step can be reduced. Due to the high computational time, 5 [s] time step is adopted, which for this study is tested as good compromise between detailed results and computation time.

Chapter 5

EC Model Validation and Results Discussion

The electrochemical model is validated alone as a first step, made with all the parameters defined in the respective sections. Non-isothermal coupled ECT validation is carried out in the next chapter. Isothermal discharge behavior of the cell fundamental unit is tested against OEM's data collected from experimental tests. The model is designed and tested to work in a range from $10^{\circ}C$ and above, under the hypothesis that the low temperature boundary is kept by a BTMS controlling the cell. The constant current isothermal discharge is performed at three different constant temperatures: low, reference and high temperature, representative of the entire cell operating temperature range, to check if the temperature dependency of the model is correctly captured. Inside each constant temperature, the cell is completely discharged by four different currents, namely: nominal C-rate, low C-rate, high C-rate, and very high C-rate, which is simulating the cell fast discharge (due to company non-disclosure policies their value is not disclosed). The three temperatures and four C-rates give a pattern of twelve tests in which the developed model is validated against the reference experimental data. The simulation is stopped when the battery reaches the lower cut off voltage or there is no more usable SOC.

Errors on the model voltage prediction, against the observed values in the tests, shown in Figure 5.1, are evaluated in two steps: Firstly, the maximum percentage error is obtained for the worst point of each case [52]:

$$max\%_{error} = \frac{|V_{sim} - \hat{V}_{exp}|}{\hat{V}_{exp}} \cdot 100 \quad (5.1)$$

Secondly, in each test the overall discharge root mean square error RMSE is calculated using Equation 5.2:

$$RMSE = \sqrt{\sum_{i=1}^n \frac{(\hat{V}_{exp} - V_{sim})^2}{n}} \quad (5.2)$$

which is the most important, since it is determining the overall goodness of the model fit. Values for all the cases are tabulated in Tables 5.1 and 5.2.

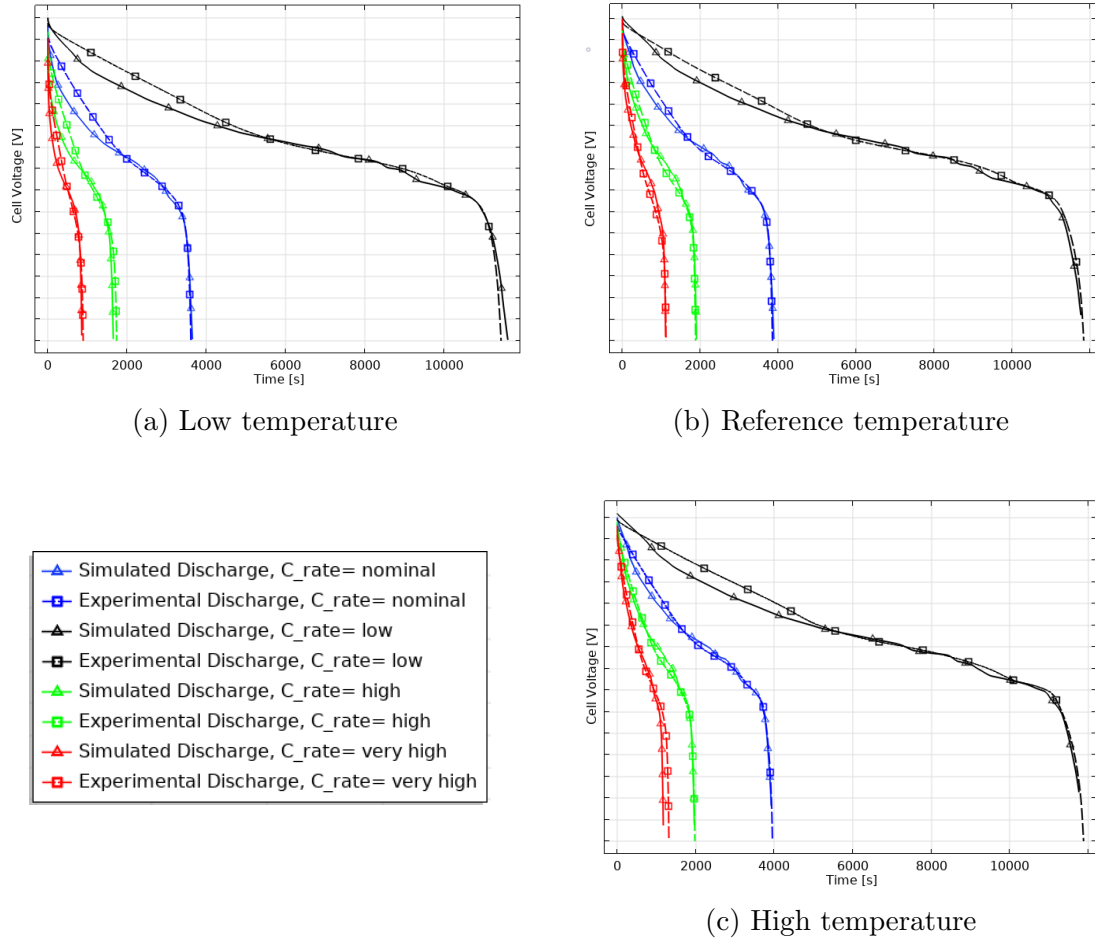


Figure 5.1: Isothermal cell voltage during constant current discharge at different C-rates

From Figures 5.1 and 5.2, good match between experimental data and simulated discharge curves is observed for all cases and tested C-rates. Starting from the nominal situation at reference temperature in Figure 5.1b, the trend of all discharge rates is captured with an acceptable maximum errors of 8.8%. Table 5.1 and low values of RMSE shown in Table 5.2 are again demonstrating the goodness of the overall model.

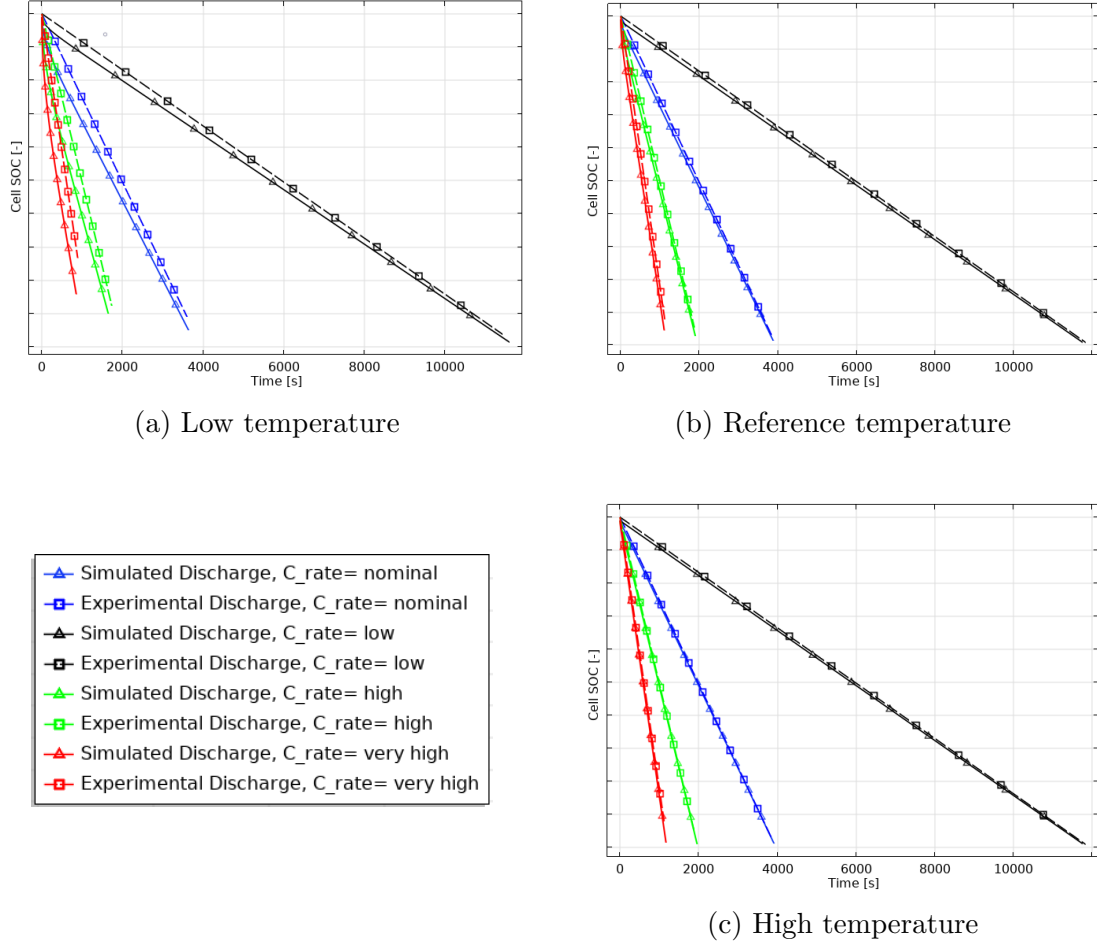


Figure 5.2: Isothermal cell SOC during constant current discharge at different C-rates

As the C-rate increases, both errors increase as well, trend that is noticeable in the plot as there is a higher deviation. From the SOC perspective, Figure 5.2, the error is not investigated because these values were not available in the cell experimental data. It was possible to calculate the value of the cell SOC from capacity data however, no reference starting SOC number with respect to the cell capacity were provided. Uncertainties both in the experimental and model SOC calculations prevent to check the discrepancy in terms of error value. However, from the Figure 5.2, the model SOC trend is near experimental SOC in all cases, presenting a constant offset due to the uncertainty of the SOC computation method rather than the goodness of the model as expressed before. In table 5.1, voltage errors distinguished with * are all detected at low SOC values, so this is an additional proof that higher inaccuracy is linked to the SOC calculation method rather than the voltage prediction of the model. As a result, the RMSE is a more meaningful indicator in this case and overall it is possible to say that the model is valid in the whole selected temperature range.

Table 5.1: EC model voltage maximum percentage errors

C-rate	Low T	Ref. T	High T
Low	9.745%*	3.094%	1.794%
Nominal	6.131%*	6.551%*	1.836%*
High	13.392%*	8.830%*	3.561%*
Very-high	9.629%*	5.145%*	17.58%*

Table 5.2: EC model voltage RMSEs

C-rate	Low T	Ref. T	High T
Low	0.0453	0.0331	0.0364
Nominal	0.0618	0.0346	0.0287
High	0.0918	0.0447	0.0307
Very-high	0.0876	0.0559	0.0767

When the temperature increases to higher values, the model errors are all reduced in all rates, see Tables 5.1, 5.2, except for the highest one which is explained by the SOC difference. As temperature increases, before reaching dangerous limits, reactions are enhanced due to a decrease of battery internal resistance, as explained in Section 2.2. This causes less voltage drop over time, as it can be noticed in a longer discharge time in Figure 5.1, and higher utilization of the cell, visible as lower SOC values at end of the discharge in Figure 5.2, for all C-rates [118]. Also in this temperature value, the trend for which the model highly deviates as the applied current rises is present. This is typical of many of the models presented in literature, [24, 29, 50, 52], which although including temperature dependence properties, have not the specific knowledge to capture phenomena happening as the temperature rises. This can be also a limitation of the P2D approach, which is a detailed EC model but still an approximation of the reality.

As forecasted in the introduction section 2.2, low temperatures, represented by the first test case, are an obstacle for the battery performance, which from the experimental data are visibly reduced. The battery finishes its stored energy when starting

from lower values of voltage, Figure 5.1, and reaching the lower cut off voltage with a poor utilization, visible as high residual SOC amount at the end of the discharge, Figure 5.1. Modelling results struggle as well as the battery itself. All errors in Tables 5.1, 5.2 increase and also graphically the higher difference is noticeable. The maximum errors are in accordance with the previous research available in literature [24, 29, 50, 52], under high discharge rates and low temperatures. In [52], the highest error is at $5^{\circ}C$ which explains the difficulty of low temperature modelling. This is due to the complexity of additional electrochemical phenomena, rising at low temperature, for which a dedicated modelling approach is required. Sluggish reactions and specific phenomena, like Li-plating at negative electrode occur which in this model are not included.

The model suffers an initial underestimation of the voltage value for all the tested situations as seen in Figure 5.1. This is investigated thoroughly on all parameters involved in the model. For example, an additional film resistance R_{film} [Ω], was added to account for the additional SEI resistance in the overpotential in Equation 3.35, similar to [24, 52]. Unfortunately, the issue was not solved. However, there are several physical explanations that can justify that, mainly linked to the material properties. First of all, in the development of this model no exact material properties and characteristics were known hence, values are approximated based on the method explained in the methodology section, with pretty good overall results. The sources of error could be:

- NMC positive electrodes are prone to undergo phase changes, which here are not included in the model not having quantitative data,
- Electrodes and separator are usually filled with unknown binders and additives to enhance their performances like *Ti*, *Si* and ceramic materials which usually are kept secret by the manufacturers,
- Particle radii of the materials vary in a range, some models are including this [24], but in this thesis is taken as a fixed value. This is one of the first add on to the model that can be considered as future work, which accounts for particle size distribution (PSD) and some phenomena as the higher usage of small particles at high C-rates captured [24],
- Particles are approximated as spheres in the P2D model, but in reality they are far from that regular shape.

Chapter 6

ECT Model Application Results Analysis and Discussion

6.1 Single Layer Results and Full 3D ECT Model Comparison

To validate and investigate the so called simplified approach (P2D electrochemical + 3D Thermal Model) a full 3D ECT model is developed. This is a unique component (see Figure 6.1) where both electrochemistry and thermal balance are solved in 3D with 3D temporal and spatial distribution (the cell is halved to speed up the computations). The development of this model follows the same procedure and data of the simplified model however, the coupling is realized by a multiphysics electrochemical heat node, embedded in COMSOL Multiphysics[®] instead of a manual procedure. The development of the full 3D model, which is the nearest to the real phenomena taking place in the cell, is justified by the scarce amount of the experimental data. Only non-isothermal voltage discharge curves and temperature sensors history on the battery cell are available. No information was available regarding the amount of heat generation or temperature distribution of the specific application under study. Hence, the complex model is used for the heat generation comparison and thermal balance validation together with previous results available in the literature. Thermal validation is also an additional check of other temperature dependent properties in the model. Heat sources comparison by domains can be seen in Figure 6.2 for both models under natural convection case and nominal discharge current.

It is observed that the heat generations over time are captured quite similarly by the two models for the most of components, as shown in Figure 6.2a, 6.2b. In

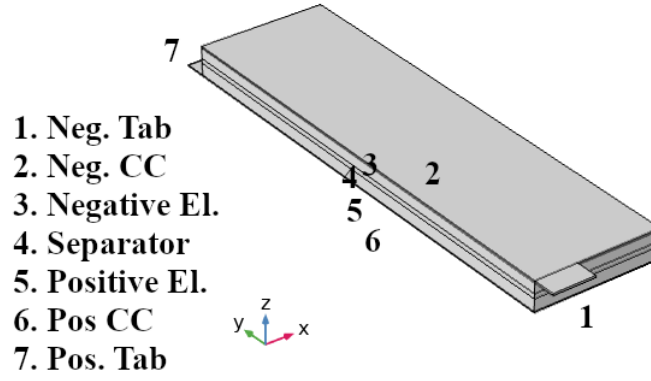


Figure 6.1: Full 3D ECT model of one layer in COMSOL® with Scale=100 on y axis

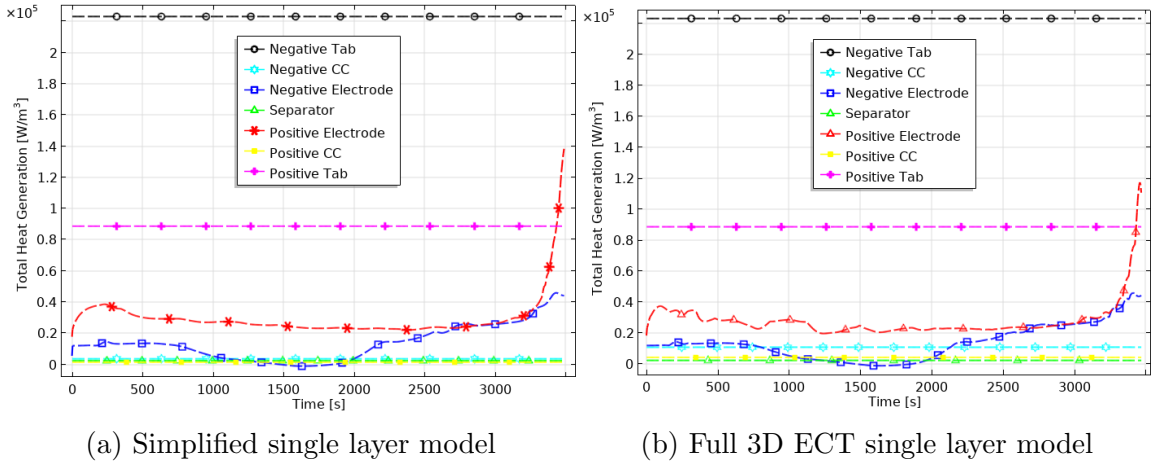


Figure 6.2: Domains heat sources comparison over time under nominal current and $h = 7 [W/(m^2K)]$

particular, both tabs are generating higher volumetric heat due to the total current passing in a narrow area. The negative tab presents more than double the heating contribution (i.e. $2.232 \cdot 10^5 [W/m^3]$) which is the result of a reduced thickness by half with respect to the positive tab, even though the tab is made of copper, a material with a high electrical conductivity. Another interesting remark is that the domains which involve only the Ohmic heating generation (separator, current collectors and tabs) have a constant heat generation since conduction is the main phenomena while in the electrode domains, additional electrochemical reactions results in uneven heat generation over time. The positive electrode produces more heat than the negative electrode during the overall discharge duration and near 3000 [s] the negative electrode heat generation equals the positive one for a limited amount of time. It is interesting

to notice that the volumetric heat of the negative electrode in an interval between 1250 [s] and 2000 [s] is less than zero, meaning an endothermic contribution hence, the component is absorbing heat rather than generating it.

Table 6.1: ECT models integral of volumetric heat sources comparison

$[J/m^3]$	Simplified single layer model	Full 3D ECT single layer model
$Q_{h,tab,neg}$	$7.79 \cdot 10^8$	$7.74 \cdot 10^8$
$Q_{h,neg,cc}$	0.03511	$3.79 \cdot 10^7$
$Q_{h,tot,neg}$	$4.76 \cdot 10^7$	$4.70 \cdot 10^7$
$Q_{h,sep}$	$8.36 \cdot 10^6$	$8.31 \cdot 10^6$
$Q_{h,tot,pos}$	$1.03 \cdot 10^8$	$0.97 \cdot 10^8$
$Q_{h,pos,cc}$	0.05583	$9.67 \cdot 10^7$
$Q_{h,tab,pos}$	$3.09 \cdot 10^8$	$3.08 \cdot 10^8$

The area of the curves has been calculated and reported in Table 6.1, to add a numerical check to the visual comparison. Heat generation integrals are correctly captured by the simplified P2D EC approach coupled with the 3D thermal balance, with respect to the fully coupled 3D ECT model in all the domains. The only difference is regarding the current collectors' domains. To understand this phenomena, it is necessary to explore the approach taken by COMSOL Multiphysics® in computing the equations to capture the difference in the physics of the two models. COMSOL Multiphysics® calculates the heat sources over the domains as current density and potential derivative product for each component over a volume, which in this case is the positive or negative current collector volume $V_{ol,cc,i}$ [m^3]:

$$Q_{Ohmic,cc,i} = \frac{\int -i_s \nabla \phi_s dV_{ol,cc,i}}{V_{ol,cc,i}} \quad (6.1)$$

So the reader may ask themselves why the heat generation of the tabs is correctly captured while the one in the current collectors is not. An explanation is that the integral and the operator ∇ involves the three dimensions x, y and z, and when the streamlines of the current magnitude are analyzed from the full 3D model, Figure 6.3, it is noticeable that the current enters the tab in y direction and goes into the current collectors. In the current collectors it is clearly visible that the current is

travelling and spreading in all three directions x , y and z . Then, when it is conducted in the battery active material (the two porous electrodes and the separator) again the current travels mainly on one direction, the battery thickness z , in this case.

At this point, the initial hypothesis can be verified as the simplified approach has its whole electrochemical model solved in only one special variable which is the battery thickness dimension. This dimension is sufficient to correctly compute the amount of generated heat since all the current travels mainly on one axis, z for the battery active material and y for the tabs domains. The only domains where these are not calculated correctly are the current collectors, where in reality (as seen by Figure 6.4) all three dimensions are contributing to the Ohmic heat generation of the current collecting foils. In all other domains Equation 6.1 can be approximated with a one dimensional derivative instead of using the gradient. In addition, when the conduction can be approximated as one dimensional and the volume is small (which is required to have limited gradients of current density and potential), Ohmic heat generation could be easily approximated with an analytical electrical analogy by applying Equation 3.44, where the product $R \cdot i^2$ obtains a similar result of current density component in the i direction by derivative of the potential in the i direction, Equation 3.43. The limited volume of the tab and the one-dimensional current conduction on y direction, makes this approximation possible. No analytical approach is found to approximate the current collector heat generation due to the presence of gradients of current density and potential partial derivative along each direction, Figure 6.4. A simple constant product $R \cdot i^2$ cannot capture a product of dynamic quantities changing in x , y , z but also inside x , y and z directions, which results in a non-uniform heat generation. Without developing a full 3D electrochemical model is also difficult to obtain numerical values of ϕ and i to approximate the heat generation of these domains. Since this contribution is important, to correctly capture the temperature gradient evolution of the cell during the discharge a difference is obtained from the two models to take into account a value reproducing the correct heat generation also in the simplified approach for the complete cell simulations.

Figure 6.5 classifies all the heat sources that contributes to the total heat production of Figures 6.2a, 6.2b. The heat generation of positive electrode in Figure 6.2a is caused for its major part by the mixing heat (caused by Li concentration change) and reversible heat contribution. Less important are reaction heat and Ohmic heat, the two components of irreversible heat detailed in Section 2.4.3 and 3.2. In the negative electrode, reaction irreversible heat is the main cause of heat generation over the whole discharge but in Figure 6.2a the total is counterbalanced by the reversible heat

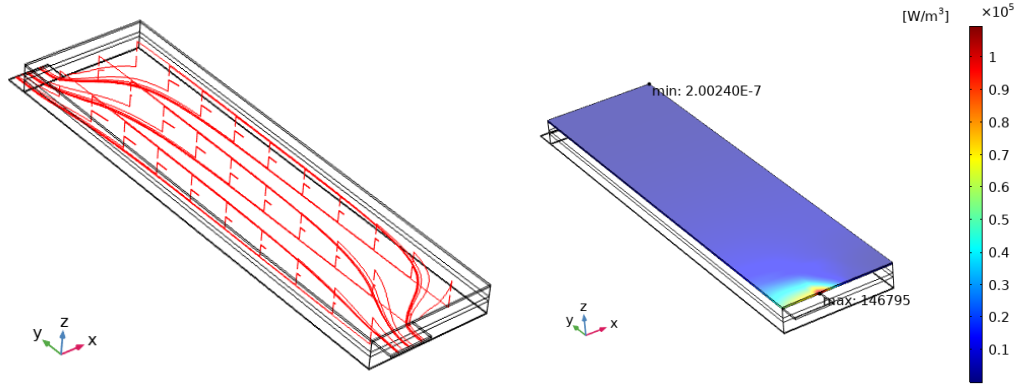


Figure 6.3: Full 3D model current streamlines in the cell

Figure 6.4: Full 3D model uneven Ohmic heat generation in the positive CC domain

which is endothermic until 2500 [s]. This is also shown in Figure 6.5. This is in line with some previous studies that underline the importance of the entropic reversible heating contribution and the fact that it is also frequently endothermic [29, 144, 65]. The reversible heat causes the total heat generation of the negative electrode to be endothermic, as reported in 6.2a. In conclusion, mixing effects are less important in the negative electrode.

The full 3D ECT model can provide distributions of various properties in the fundamental unit 3D geometry, seen in Figures 6.3 and 6.4. Instead the simplified approach has only the possibility of investigating the variables along the thickness of the cell z . As explained before, this is enough and correct for a thermal study while keeping acceptable computational time. It is feasible although not always necessary to study distribution of electrochemical variables, like potential and current density, however, in such approach the full 3D ECT model becomes necessary, which is computationally expensive.

If the C-rate is increased to simulate a fast discharge, the resulting heat generations can be found in Figure 6.6. All the contributions are increased to the order of magnitude of 10^6 , as can be seen from Figure 6.6a. The trends are similar to the nominal current case, Figure 6.2a with the exception of the negative electrode which in this case has no endothermic parts over the discharge. This can be explained from the different typologies of heat sources in Figure 6.6b. In this case, the reaction heat of positive electrode has a contribution similar to the positive electrode reversible heat and not lower as seen previously. In the negative electrode, the reversible contribution is still endothermic for 2/3 of the discharge duration but the reaction's (irreversible)

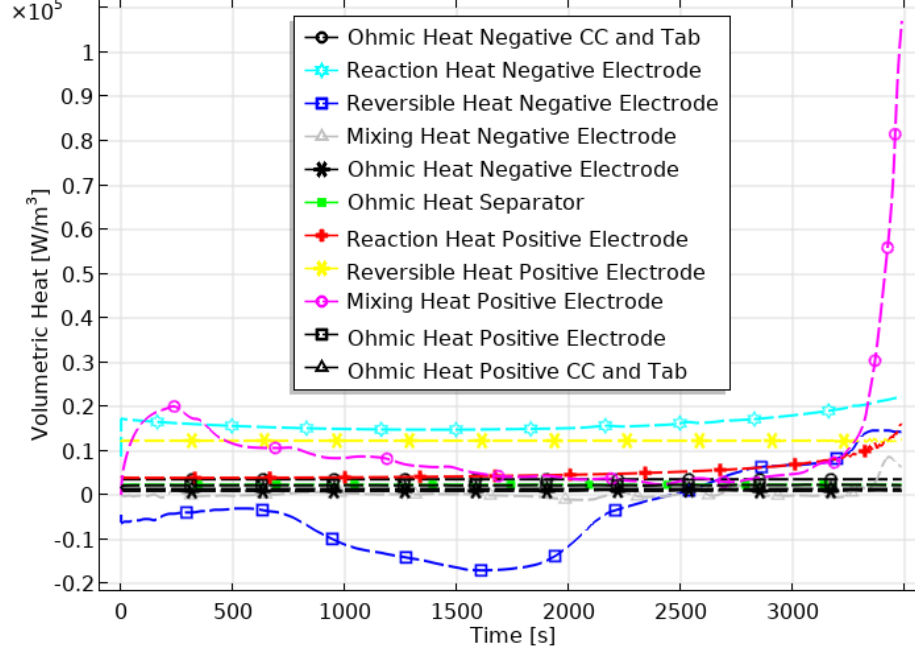


Figure 6.5: Heat sources characterization over time under nominal current and $h = 7 [W/(m^2K)]$

contribution increases by greater extent causing the overall negative electrode heat generation to be exothermic for all the discharge period. Overall, it is possible to say that by increasing the applied C-rate to discharge the cell, the irreversible contributions (reaction and Ohmic heat sources) rise by higher amounts than reversible ones. As the applied current increases the heat generation due to irreversible phenomena becomes dominant (according to [29, 146]).

6.2 Complete Cell Models Results

The final step of this coupled electrochemical-thermal study is to apply the validated electrochemical-thermal model on the complete battery cell to obtain the temperature rise and its distribution under different working conditions. The two cell modelling approaches presented in Figures 4.9 and 4.10, will be discharged at two C-rates: nominal and fast discharge, under natural and forced air convection as described in Section 4.7. Four cases for each model are generated in this way.

In each model, a pattern of temperature sensors is employed as seen in Figure 6.7. Points are not selected casually but crucial zones, as the tab-to-cell connections are individuated to probe the temperature (sensors 1, 2, 12, 13). In the cell center the

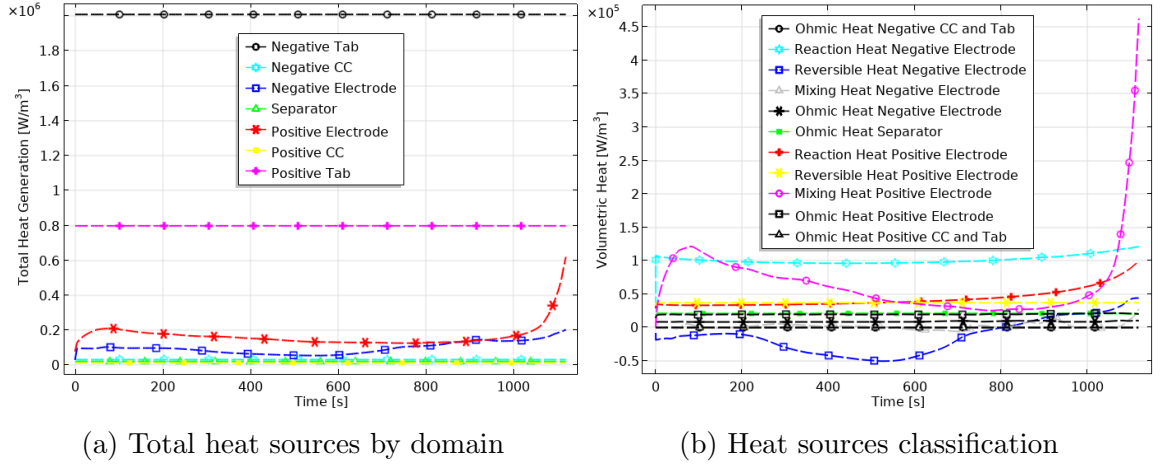


Figure 6.6: Domains heat sources and classification over time under fast discharge and $h = 7 [W/(m^2K)]$

temperature is measured on the half thickness plane (central sensor 6) as well as on the two side surfaces (sensors 7 and 8). In the following discussions in this thesis, if the sensor is not specified, the cell temperature is considered the average of the total cell.

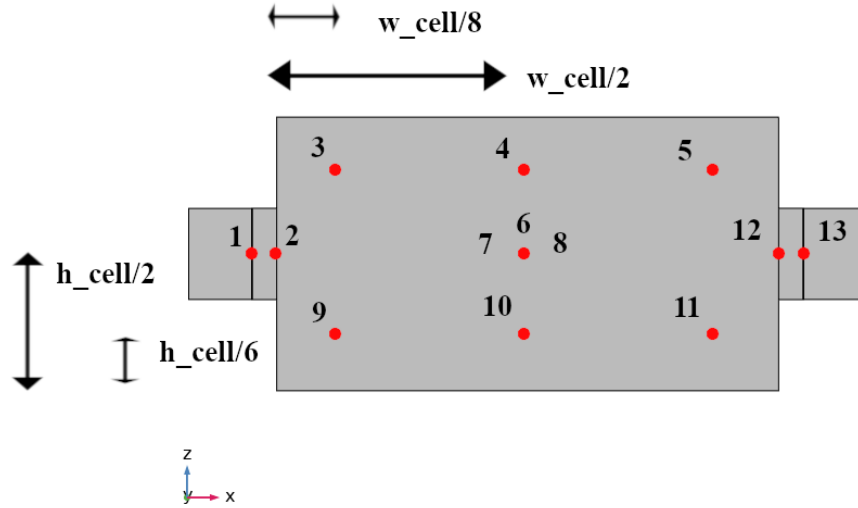


Figure 6.7: Temperature sensors positioning in the cell geometry

6.2.1 Case A: Nominal Discharge C-rate and Natural Convection

Temperature sensors

The results of the temperature sensors are reported in Figure 6.8. For the average heat source model, Figure 6.8a, it is possible to note that until 750 [s] circa all the different points in the battery cell have a similar rise, tabs have just 0.3°C higher values. From 2500 [s] the external tabs will remain at circa 0.3°C lower for the remaining discharge time, as it is presented in the following Figures 6.10, 6.11, 6.12, 6.13. The point with the highest temperature will be the cell center (Sensor 6). All the measured temperatures have a deflection from 1000 to 2000 [s] due to a lower total heat generation in that time interval due to the negative electrode reversible heat contribution (coming from the single layers analysis, Figures 6.2, 6.5). In the remaining discharge time, the temperature rises till the end, reaching 35.4°C . It is possible to state that during this whole discharge there is no significant temperature difference across the cell. For the model including the internal tabs and the layers division, temperature trends are similar (Figure 6.8b), they include the flex around 2000 [s]. Peak temperature at discharge end is 34.1°C in the cell center, which is slightly lower value than Figure 6.8a, that could be caused by the absence of the pouch cell cover in this model. However, higher gradient is registered by sensors 3, 5, 9, 11, describing the cell external surface, after 250 [s] present a temperature trend 0.35°C lower than the cell center. At the end, internal tabs and external tabs peaks at 3°C and 4°C lower than the cell center respectively.

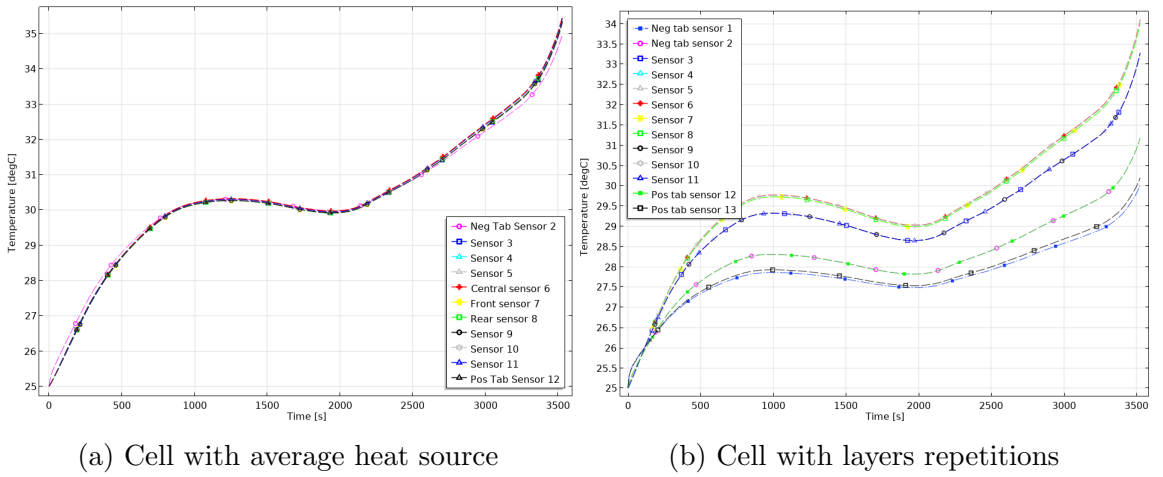


Figure 6.8: Temperature sensors readings through discharge at nominal C-rate and $h = 7 [W/(m^2K)]$

Temperature distribution

Figures in this section present the temperature gradient evolution during the cell discharge. Figures 6.10 and 6.12 plot the cell average heat source model temperature, respectively in: the central plane of the battery cell and on its surface. The same distinction is made for the layered model with distributed heat sources as seen in Figures 6.11 and 6.13. This scheme is used for all the four cases.

Average heat source model: As introduced with the temperature sensors, at the start of the discharge, the hottest zone is represented by the battery external tabs in which the total current is conducted. Near 2280 [s], the hottest point of the battery passes from the external tabs to the battery center, which remains till the end of discharge (Figure 6.10c). This change is reflected in the surface also, however it appears later at 2465 [s] (Figure 6.12c). The hot spot migration is happening due to the effect of convective cooling at the battery tabs (similar as derived in [147]), while the center is protected by the thin pouch cell cover. Maximum temperature is 35.4°C in the center and 35.3°C on the surface. A difference greater than 1°C is not recorded anywhere within the cell.

Layered model: The temperature distribution is in accordance with the cell average heat source model presented, the presence of the internal tabs and connecting elements causes the hot spot migration at 205 [s], from tabs to the cell center, Figure 6.11b, so earlier than the previous model. In addition, the positive external tab presents higher temperature than the negative one until that instant. The heat generation of the external tabs and the thermal boundary conditions (i.e. convection) are the same, hence this difference could be generated by the difference in materials, disposition and heat generation of the adjacent internal tabs. The positive external tab is directly in contact with only one Al internal tab, while the negative tab is in contact with two copper tabs behind the connection bar, Figure 6.9. Although the negative internal tabs generate more heat the copper material is more effective in dissipating heat. Surface images present the same behavior of the central plane, Figure 6.13, with the only difference that the cell exterior becomes colder after 185 [s], Figure 6.13a. The maximum surface temperature is also reached at the cell active material central zone, Figure 6.13d.

6.2.2 Case B: Fast Discharge C-rate and Natural Convection

Temperature sensors

From the temperature probes of the average heat model it is clear that the ex-

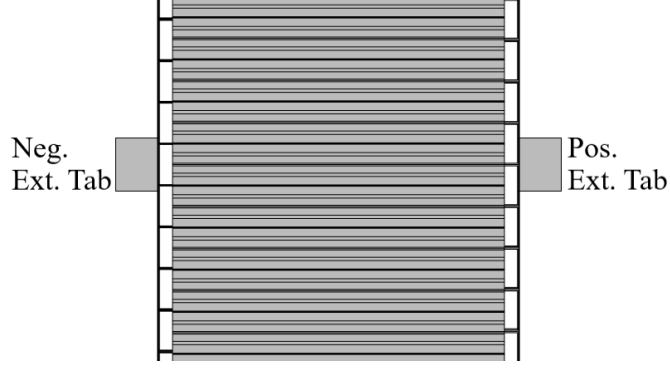


Figure 6.9: Layered cell model tab top view

ternal tabs regions are at higher temperature for the whole discharge duration (see Figure 6.14a). This is explained by the Ohmic heat generation which has a square dependency on the current applied. Hence, as the C-rate increases, the Ohmic heat contribution becomes the main one to the total heat generation, similar situation is verified in [52]. The maximum temperature reached by the tabs is 56.2°C while the cell hottest spots are at 55°C in sensors 3, 5, 9, 11 which is the area closest to the tabs. No temperature gradient over 2°C is registered over the cell. With the layered model (see Figure 6.14b) the tabs are no longer the hottest spot after 200 [s] and instead the central sensors (6, 7, 8) show the highest temperature. At the end of discharge, the maximum temperature is 52.37°C . Also, in this case, the Ohmic heat contribution avoids the temperature decrease at 2000 [s] typical of nominal current cases. Due to different geometry configuration, which has different outcome for the heat transfer solution, cell outer parts (sensors 3, 5, 9, 11) and the tabs (1, 2, 12, 13) are at lower temperature in this case. A possible explanation is the higher exposure to the air flux and the additional internal tabs which can affect the heat transfer mechanisms.

Temperature distribution

Average heat source model: Figures 6.15 and 6.17, expresses graphically the temperature sensors output, both for the central plane of the cell and the surface respectively. Over the total discharge duration, the tabs are the hot spot and inside the cell, the hottest zone is the one adjacent to the external tabs, Figure 6.15, 6.17, whereas the tabs external part reach 57.6°C , as seen in Figure 6.17d.

Layered model: Tabs are the cell hot spot until 400 [s] for the layered model central plane 6.16b, and for the surface 6.18b. As the previous Case, the positive one

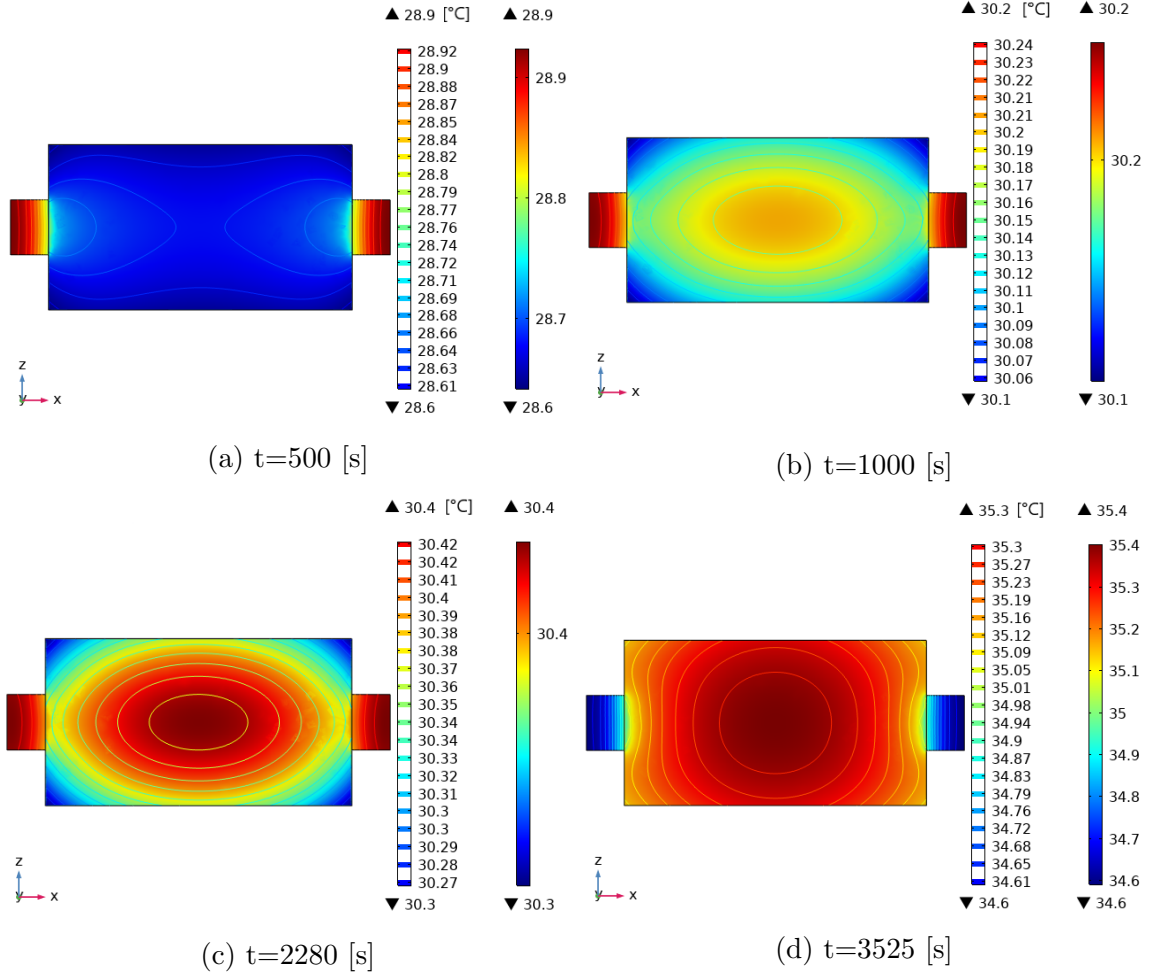


Figure 6.10: Central plane temperature distribution, in the cell with average heat source, during discharge at nominal C-rate and $h = 7$ [$W/(m^2K)$]

is found to be at higher temperature. After this instant, the cell core will be at higher temperature. In this case both in the central plane and on the surface a temperature gradient of $5^\circ C$ is registered, Figure 6.16, 6.18.

6.2.3 Case C: Nominal Discharge C-rate and Forced Convection

Temperature sensors

After a few seconds of discharge, the battery tabs are no longer the hottest spot of the entire cell due to the combined effect of reactions inside the battery and convection cooling, which is proved more effective (see Figure 6.19a). However, around 2000 [s]

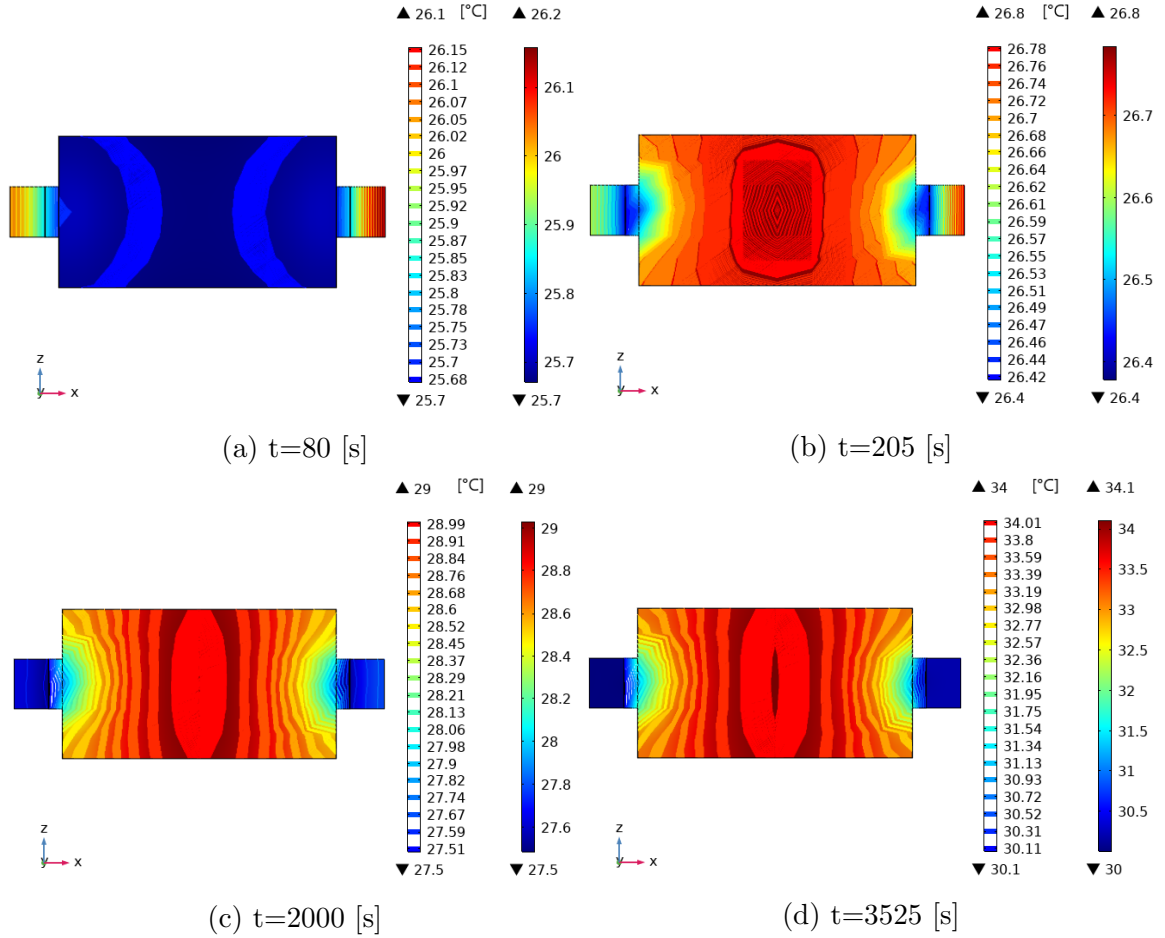


Figure 6.11: Central plane temperature distribution, in the cell with repeated layers, during discharge at nominal C-rate and $h = 7 [W/(m^2K)]$

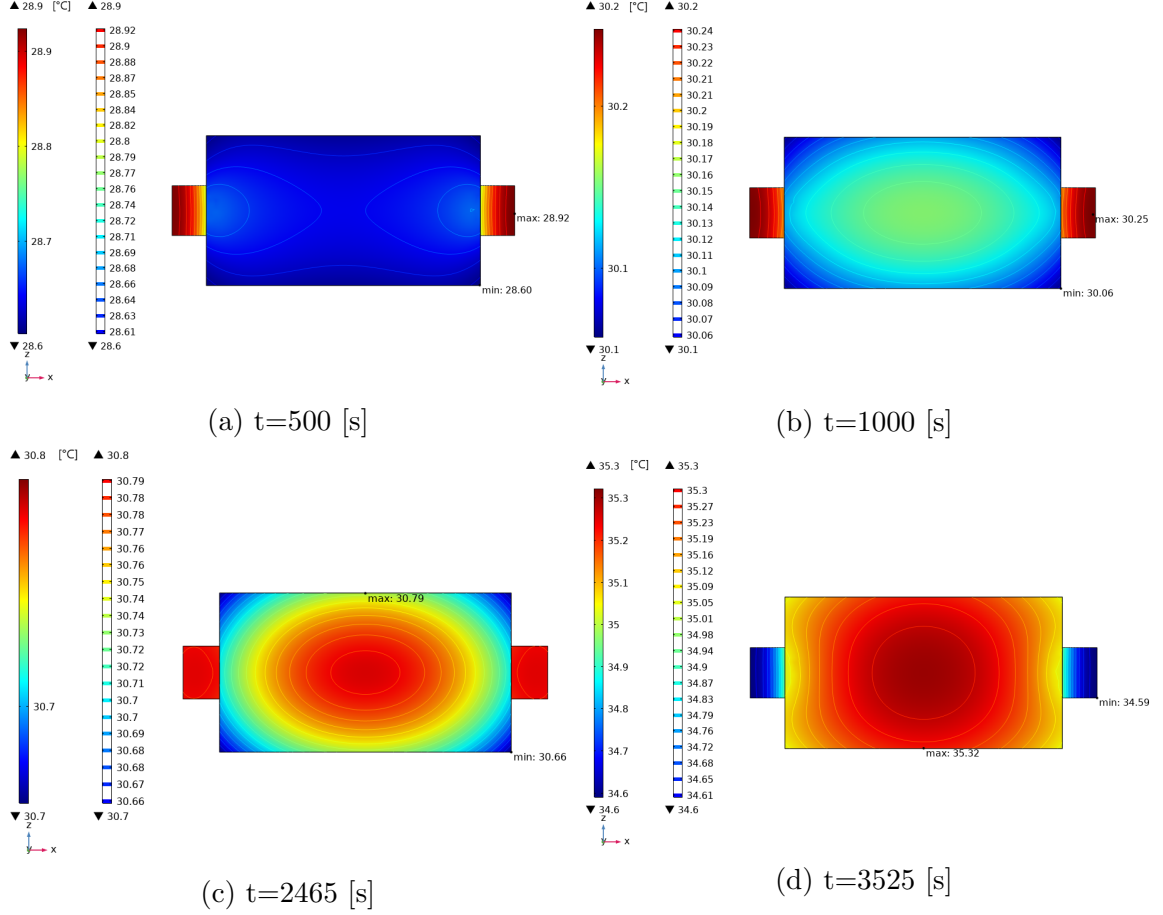


Figure 6.12: Surface temperature distribution, in the cell with average heat source, under discharge at nominal C-rate and $h = 7$ [$W/(m^2K)$]

all temperature readings are relatively close and the tabs become the cell's hottest point for a limited interval. This is clearly seen in Figures 6.20 - 6.23. Globally the temperature is kept inside the suggested optimal working range, [13, 14, 84], over the whole discharge duration and peaking at $30.2^\circ C$ at the cell center. No temperature difference higher than $0.5^\circ C$ is registered between all sensors in the total discharge duration. The layered model, Figure 6.19b, reaches nearly the same top temperature (i.e. $29.95^\circ C$) at the end of the discharge. Cell center is $0.3^\circ C$ hotter than the external part (sensors: 3, 5, 9, 10) through the whole discharge. The tabs are up to $1.66^\circ C$ lower than the core through the simulation.

Temperature distribution

Average heat source model: Past 150 [s], the battery tabs are not the cell's hot spot, compared to the temperature distribution on the central plane, as seen in Figure 6.20a. The hottest point migrates gradually toward the cell center in the period

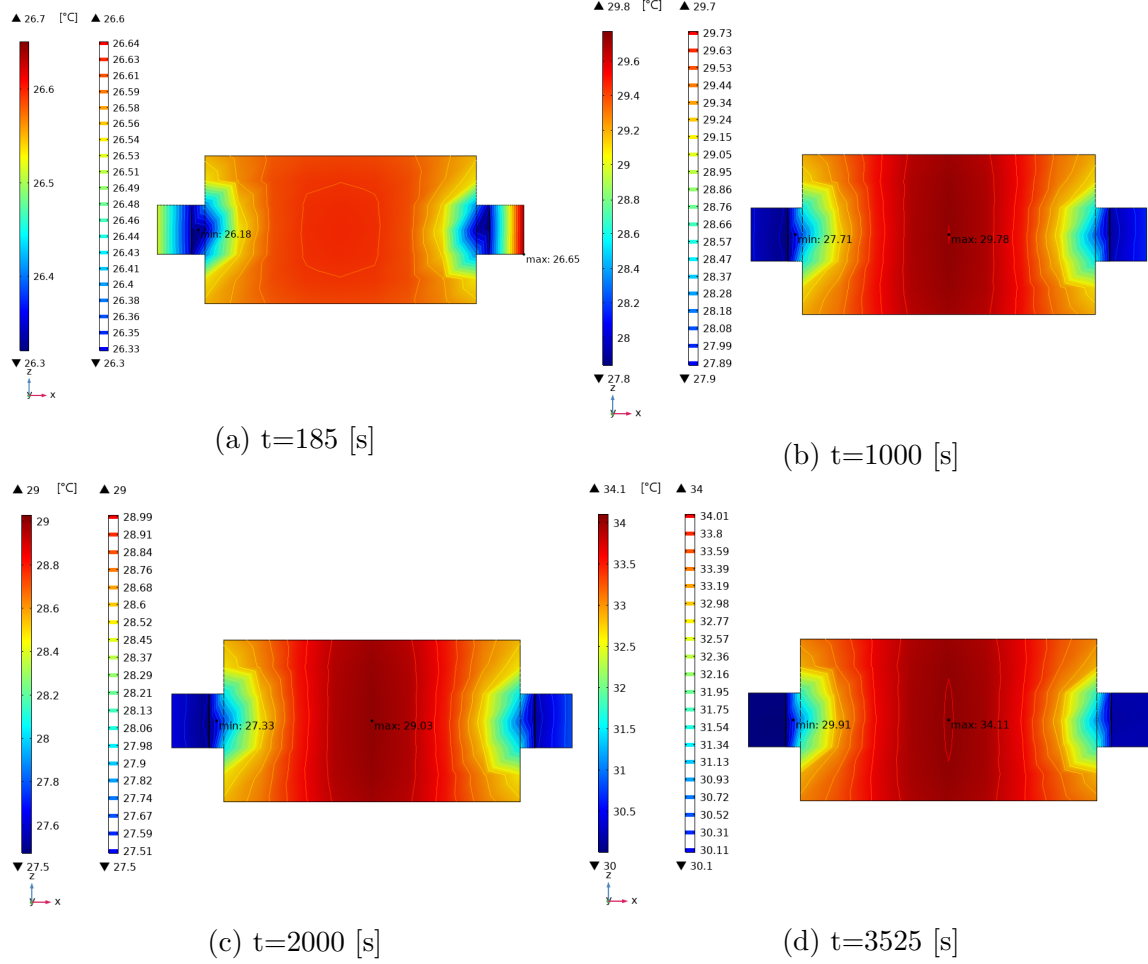


Figure 6.13: Surface temperature distribution, in the cell with repeated layers, under discharge at nominal C-rate and $h = 7$ [$W/(m^2K)$]

between 220 and 1950 [s], Figure 6.20b, 6.20c. In the cell active material, a limited gradient not exceeding $0.6^\circ C$ is observed. Looking at the surface, Figure 6.22c, the cell active material reaches lower temperatures than the tabs near 2000 s from the start of the discharge. This could be explained as in the natural convection case, by considering the negative electrodes reversible heating contribution, which is endothermic around that time interval. Temperature and temperature distribution plots are following the cell heat generation presented in the single layer section, Figures 6.2, 6.5.

Layered model: The layered model (Figure 6.21, 6.23) is not presenting the second tab hot spot near 2000 [s] although the temperature profiles are similar. It is seen that after 85 [s] the tabs are not the Li-ion cell hot spot, as seen in Figure 6.21a, 6.23a. This occurs earlier than Case A, due to the higher convective heat transfer.

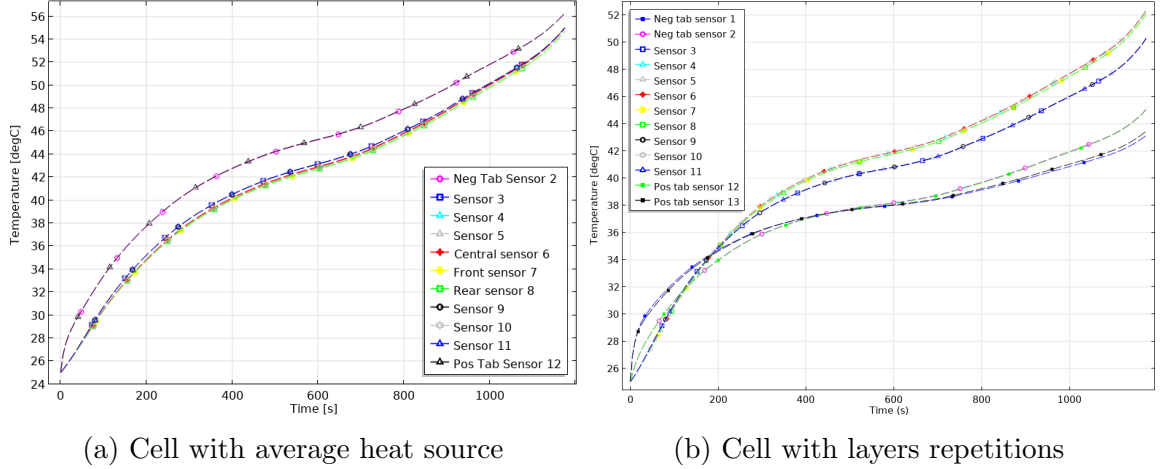


Figure 6.14: Temperature sensors readings through fast discharge and $h = 7 [W/(m^2K)]$

Still, the negative external tab cools faster, as shown in Figure 6.21a, 6.23a. At discharge end, a $2.5^\circ C$ difference is measured as core to side cell temperature difference in both central plane and surface (see Figures 6.21d 6.23d).

6.2.4 Case D: Fast Discharge C-rate and Forced Convection

Temperature sensors

At higher C-rates, tabs are producing higher Ohmic heat, hence they show higher temperature values almost in the entire discharge period, Figure 6.24a. Unlike the natural convection Case B, forced airflow blowing on the cell after 1000 [s] cools the battery external tabs, leaving the hottest spot in battery center, which reaches $41.8^\circ C$. Similar to the previous case the forced convection flux keeps the battery in the safe temperature range with a maximum of $41.8^\circ C$, $14^\circ C$ lower than Case B ($56 - 57^\circ C$ peak). Battery active material temperature gradient is not going above $0.5^\circ C$ during the whole discharge. The layered model sensors, Figure 6.24b, show higher difference in the temperature sensors across the battery cell. Unlike the previous mode battery tabs are at lower temperatures than the cell center at 400 [s] as they present $5.8^\circ C$ lower temperature than the battery core. This difference is kept over time but at the end, (3515 [s]), reaches $10^\circ C$. From 300 [s], the outer areas of the battery register temperature values $1.5^\circ C$ lower than the core, this difference reaches $2^\circ C$ at the end of the discharge period. The maximum temperature for this case is $40.96^\circ C$ in the core sensor 6.

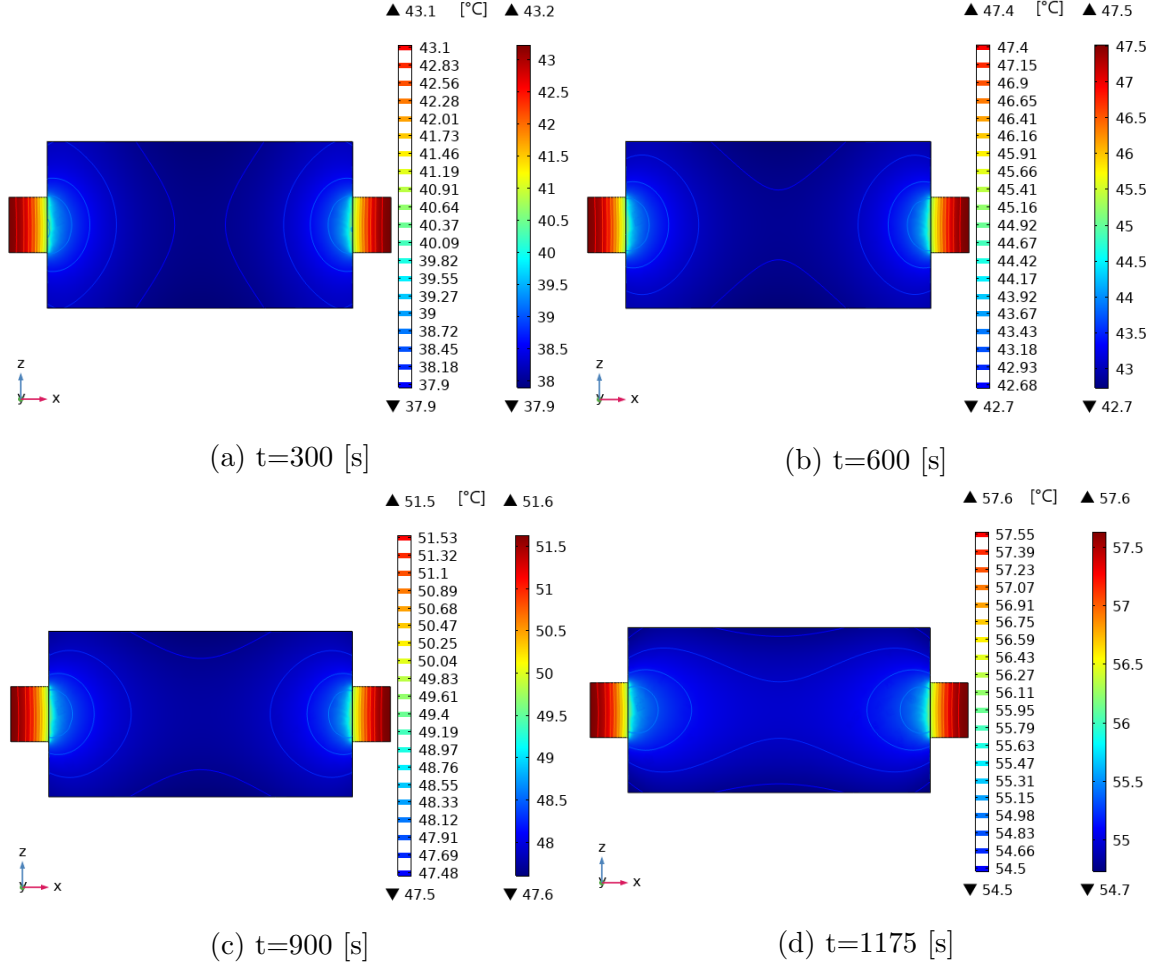


Figure 6.15: Central plane temperature distribution, in the cell with average heat source, during fast discharge and $h = 7$ [$W/(m^2K)$]

Temperature distribution

Average heat source model: Figures 6.25c, 6.27c, define the instant when the battery's active material becomes hotter than battery tabs, 1070 [s] and 1135 [s] for the center plane of the cell and for the surface, respectively. At the end of the discharge, both the center plane, Figure 6.25d, and the surface, Figure 6.27d, reach $41^\circ C$ in the cell core.

Layered model: The trend of faster tabs cooling for the layered model is confirmed also in Figures 6.26, 6.28. The tab to cell hot spot migration is detected at 120 [s] both on the surface and in the central plane (Figure 6.26a, 6.28a), sooner than 1000 [s] as detected in the average heat source model, (Figures 6.25c, 6.27c). Also, the positive tab is the last component to cool. In the active battery material, at 1160 [s] (i.e. end of discharge period), circa $6.5^\circ C$ of difference can be seen from the cell

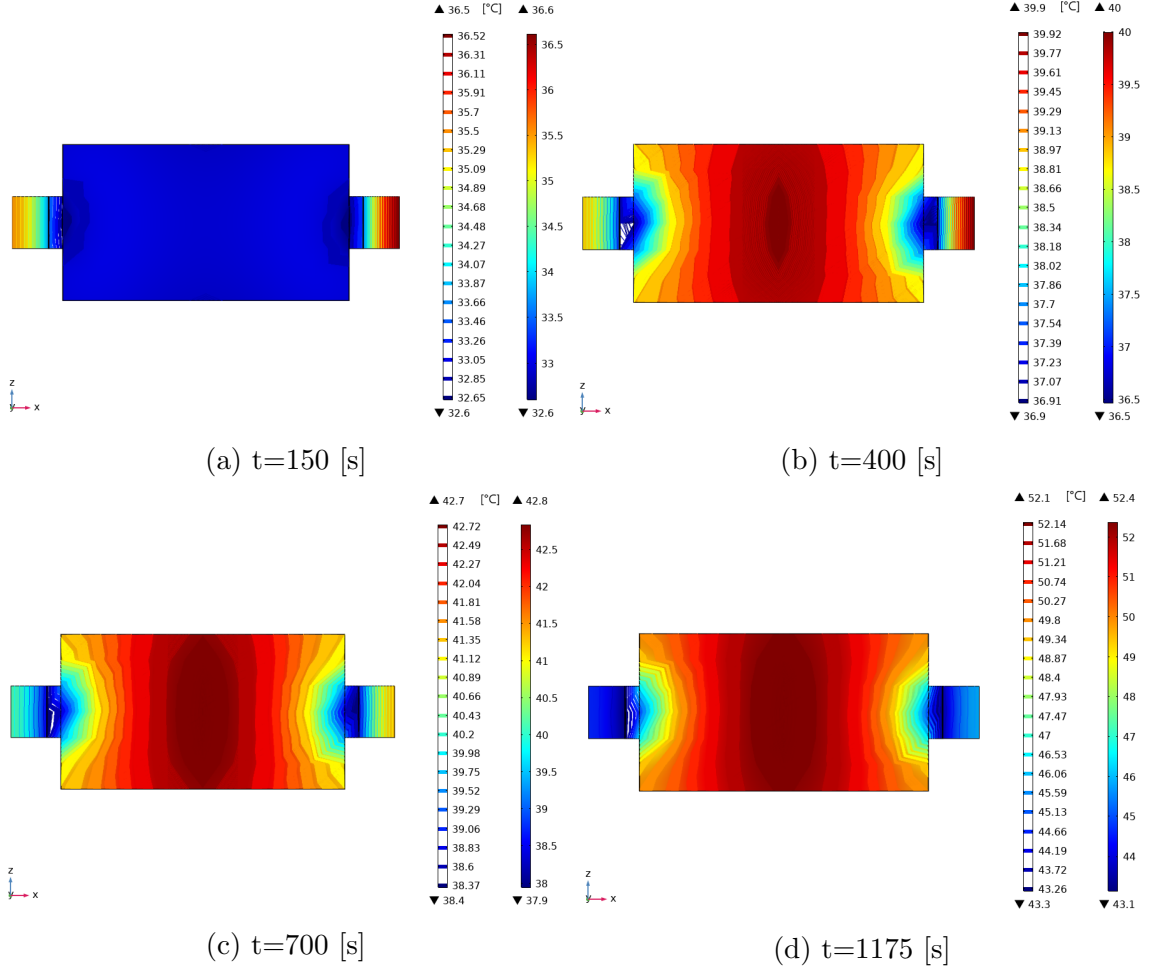


Figure 6.16: Central plane temperature distribution, in the cell with repeated layers, during fast discharge and $h = 7$ [$W/(m^2K)$]

core to the zones adjacent to the battery tabs in the battery central plane (Figure 6.26d). This is also confirmed from the surface plot, Figure 6.28d.

6.3 Overall Comparison and BTMS Recommendations

As seen in Case A, under nominal current and natural convection the temperature gradient is not approaching dangerous limits. However, it is better to monitor the situation because it is near the upper optimal temperature threshold, taken as $35 - 40^\circ C$ depending on the reference [13, 14, 84, 85].

Case B, which is the one with maximum thermal stress for the battery, demonstrates that natural convection cooling is not effective to keep the cell temperature

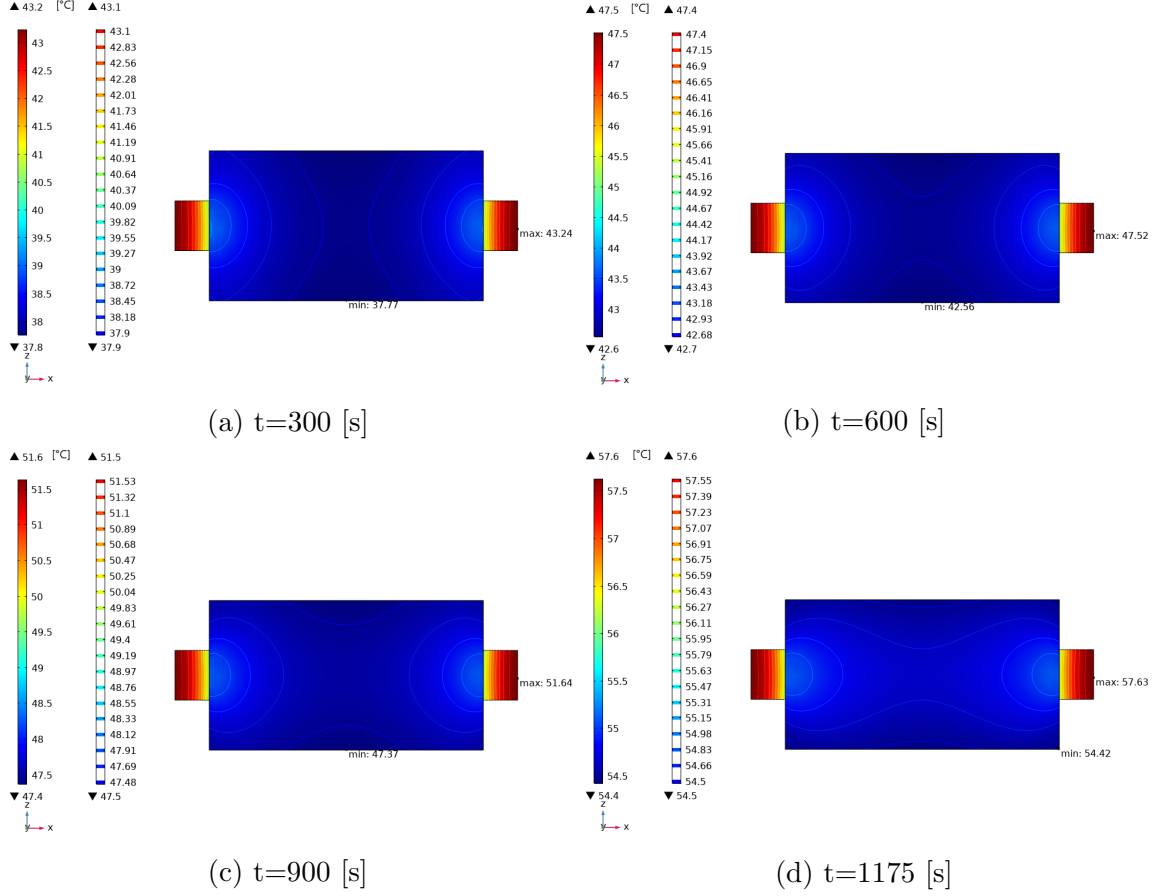


Figure 6.17: Surface temperature distribution, in the cell with average heat source, under fast discharge and $h = 7$ [$W/(m^2K)$]

safe operational range, tabs are near to $60^\circ C$ and the cell active battery material is near $52-55^\circ C$ at the end of discharge, Figures 6.15d, 6.16d, 6.17d, 6.18d. This in-line with values found in [52]. Temperature gradient in the cell active material is near the limit of $5^\circ C$ [13, 84], Figures 6.15d, 6.16d, 6.17d, 6.18d. It is important to note that in a battery module for an EV, the cell is surrounded by other components and the convection is not involving all the cell surface like in this experiment. Moreover, the cell could withstand a maximum admitted C-rate double the value of this tested one, temperature values and temperature gradient are close to dangerous failure events thresholds. References [13, 14, 84, 85] are suggesting $60^\circ C$ as critical temperature limit, from which hazardous side reactions can start and in the worst case lead to thermal runaway.

For a single cell, under nominal discharge current (Case C), forced convection is more effective than natural convection to keep the Li-ion battery in the optimal working range [13, 14, 84], while keeping the cell temperature gradient controlled,

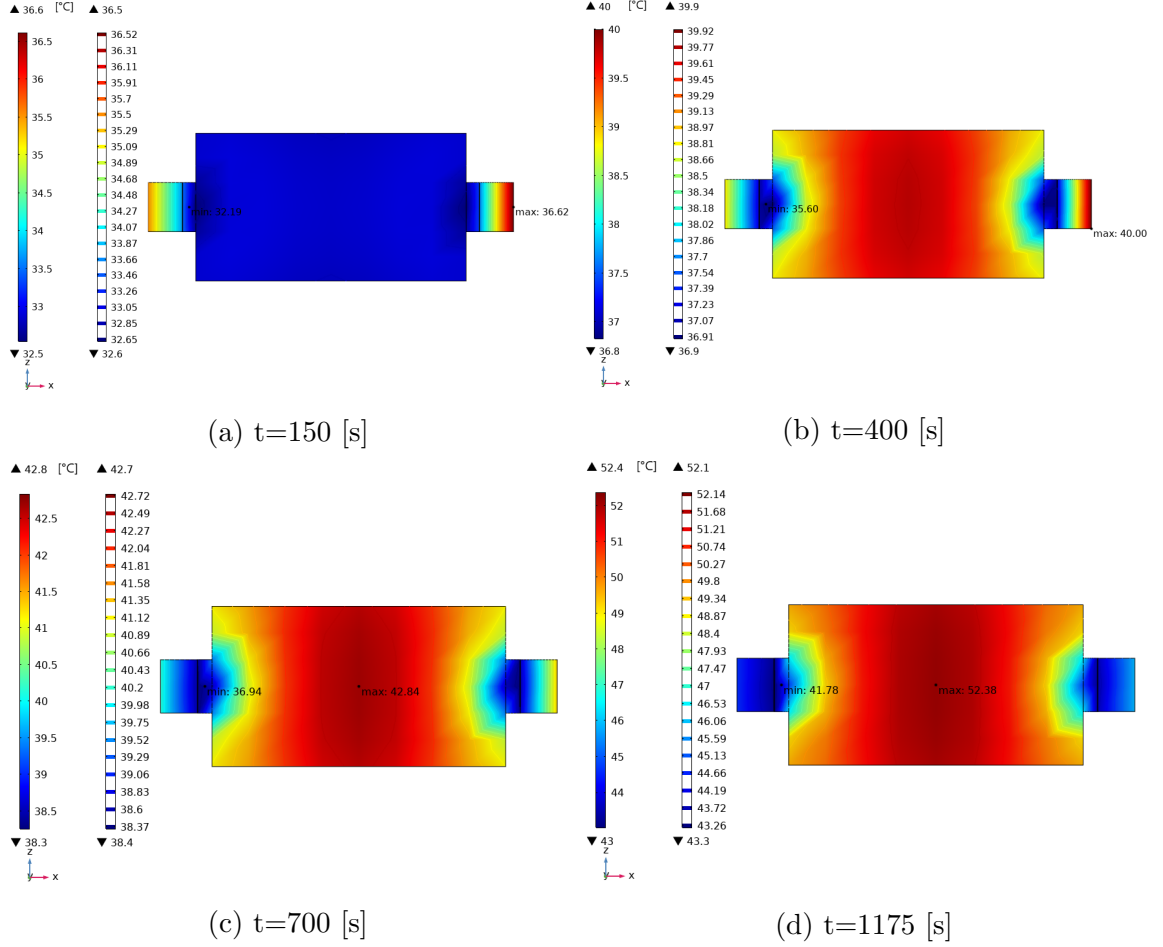


Figure 6.18: Surface temperature distribution, in the cell with repeated layers, under fast discharge and $h = 7 [W/(m^2K)]$

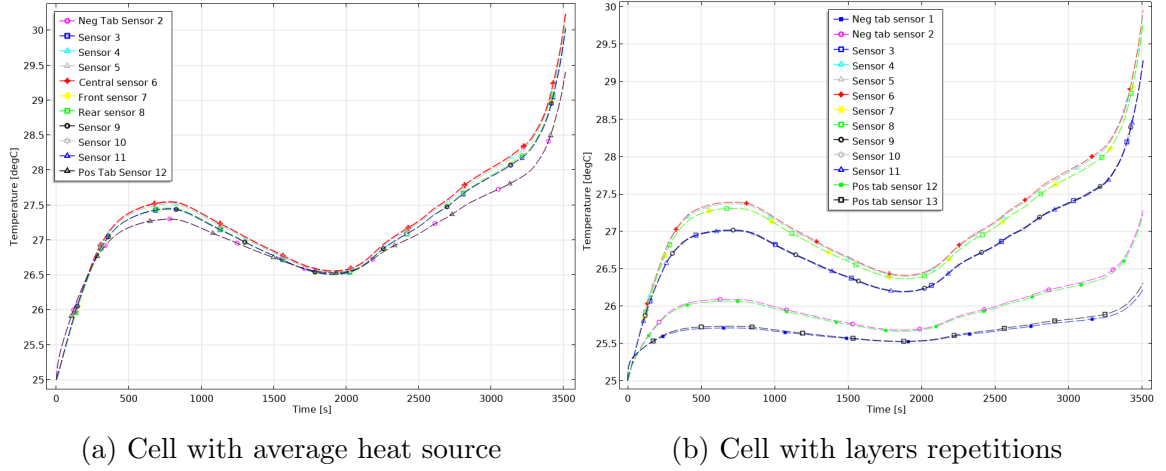


Figure 6.19: Temperature sensors readings through discharge at nominal C-rate and $h = 25 \text{ [W/(m}^2\text{K)]}$

Figures 6.25 - 6.28. However, previous studies at module and pack level suggest that this method causes temperature non-uniformity [24, 29]. Further investigation is required for this problematic on this cell for a proper BTMS design.

In fast discharge Case D, forced air convection proves to be effective to limit the temperature rise under the safe working limits, the peak of 41°C is 15°C less than the 56°C of peak temperature measured in Case B. In this way thermal runaway risk is avoided and the maximum temperature is near to the upper boundary of the optimal temperature range [13, 14, 84], which promises to guarantee long life to the Li-ion cell. However, temperature gradient is exceeding by 1.5°C the suggested 5°C safety limit, [13, 14, 84], at the end of discharge, Figures 6.26d and 6.28d. The actual performance decay and aging effects have to be studied with a dedicated model to fully evaluate the effects of this temperature difference. This is important because in a battery pack the cell is not fully exposed to the air flow hence, higher temperature gradients could take place.

Fast discharge situations (Case B and D) have lower influence on the temperature decrease in the central portion of the discharge, Figure 6.14 and 6.24, caused by the negative electrode reversible heat with respect to nominal C-rate discharge. Its relative contribution to the total heat generation is less, which is due to increased influence of Ohmic heat generation in all domains.

Layered model generally presents lower values of temperature, Figure 6.29, and tabs are not the hottest point in the high C-rate discharge, Figures 6.16d and 6.18d, which be caused by the lack of pouch cell cover in this model. Another cause of this difference is the presence of additional elements made of different materials, namely

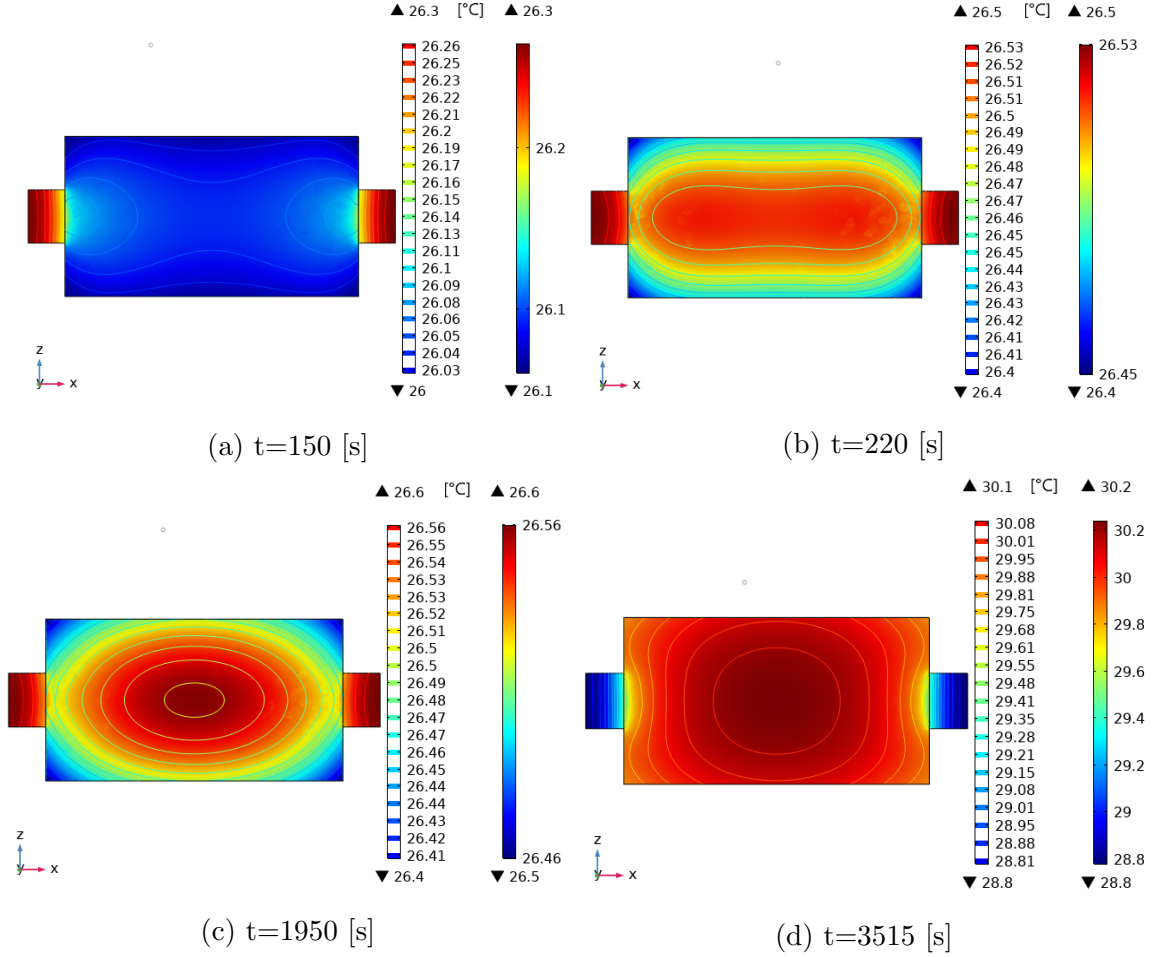


Figure 6.20: Central plane temperature distribution, in the cell with average heat source, during discharge at nominal C-rate and $h = 25$ [$W/(m^2K)$]

the internal tabs and the connection bars. These are made of Cu and Al, and they present different properties leading to various heat generations, thus they can affect the heat transfer evolution in a different manner. This can be also notice by the earlier hot spot migration from tabs to cell center, characteristic of the layered model.

Temperature estimates agrees well with the few experimental data from the industrial partner and with the reference literature [51, 52, 142, 143]. The two different cell modelling approaches gives comparable results. Although this is a widely used verification method by the researchers, the temperature distribution on the cell is often ignored. In this case the two presented models (layered and average heat cell) differ by some details, like the timing of the hot spot migration from the tabs to the cell and the hottest spot location at high C-rate. The average heat model in Case B individuates the tab as hottest point at end of discharge, while the layered model presents the cell core as final hot spot. This needs a proper experimental evaluation

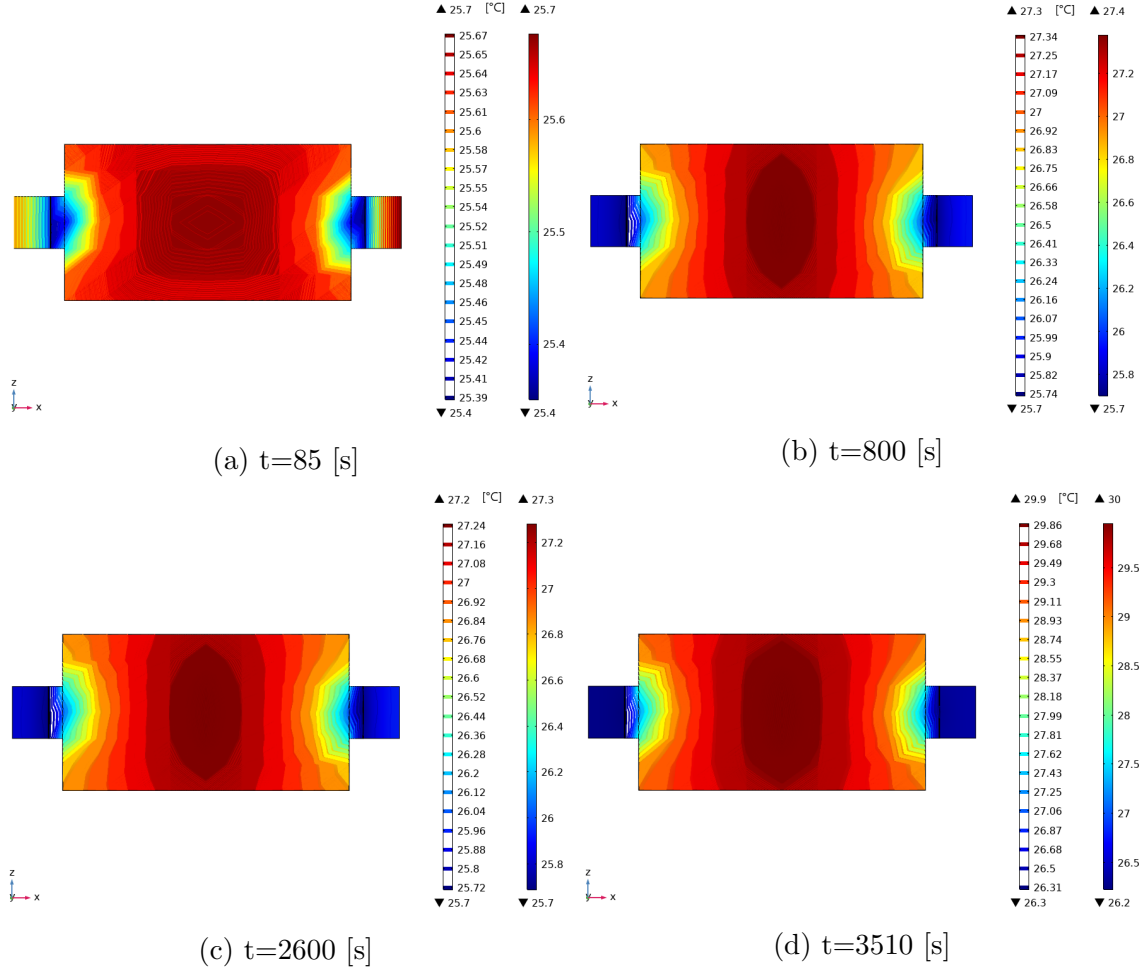


Figure 6.21: Central plane temperature distribution, in the cell with repeated layers, during discharge at nominal C-rate and $h = 25$ [$W/(m^2K)$]

with a thermal imaging camera.

Current collectors as well as tabs geometry and properties gives different outcomes on the heat balance evolution through the discharge as can be seen for the layered and average heat source model in where tabs are different. This is an aspect to study with higher detail for the final model validation. However, this remarks the importance to include these components and their heat contribution to Li-ion battery cells models [50].

The distributed heat balance thermal model adopted here is justified because the cell presents thermal gradient especially at high C-rates (Case B and D). As a consequence, uniform temperature assumption for the whole battery cell adopted in lumped models results to be inaccurate for this study [29, 58, 118] .

Overall these are good results considering that natural convection and forced air

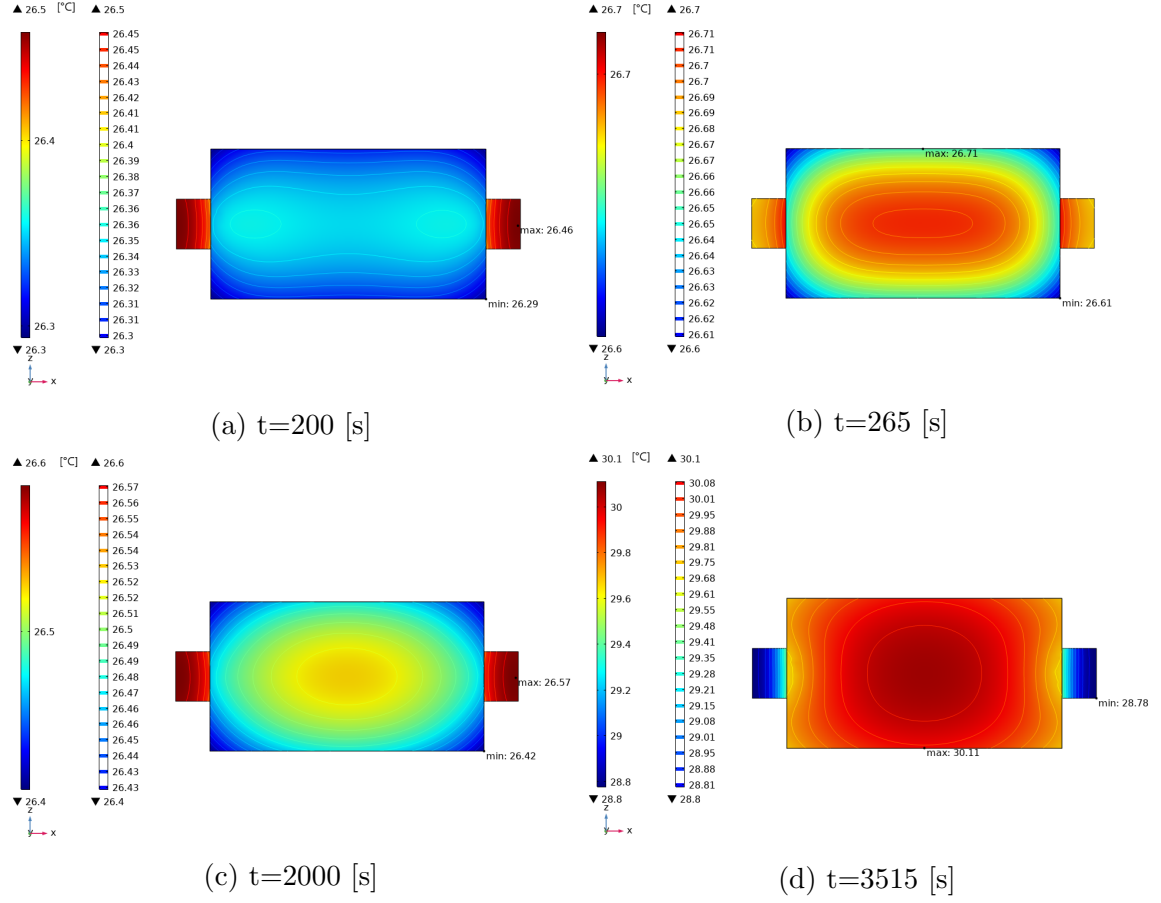


Figure 6.22: Surface temperature distribution, in the cell with average heat source, under discharge at nominal C-rate and $h = 25$ [$W/(m^2K)$]

convection are considered basic BTMS methods. By adopting advanced liquid or refrigerant cooling strategies, the temperature can be precisely controlled, for example, starting to cool the area near the tabs at start of discharge and at high rates and later focusing on the cell core. This guarantees in all situations the optimal temperature range for the specific cell.

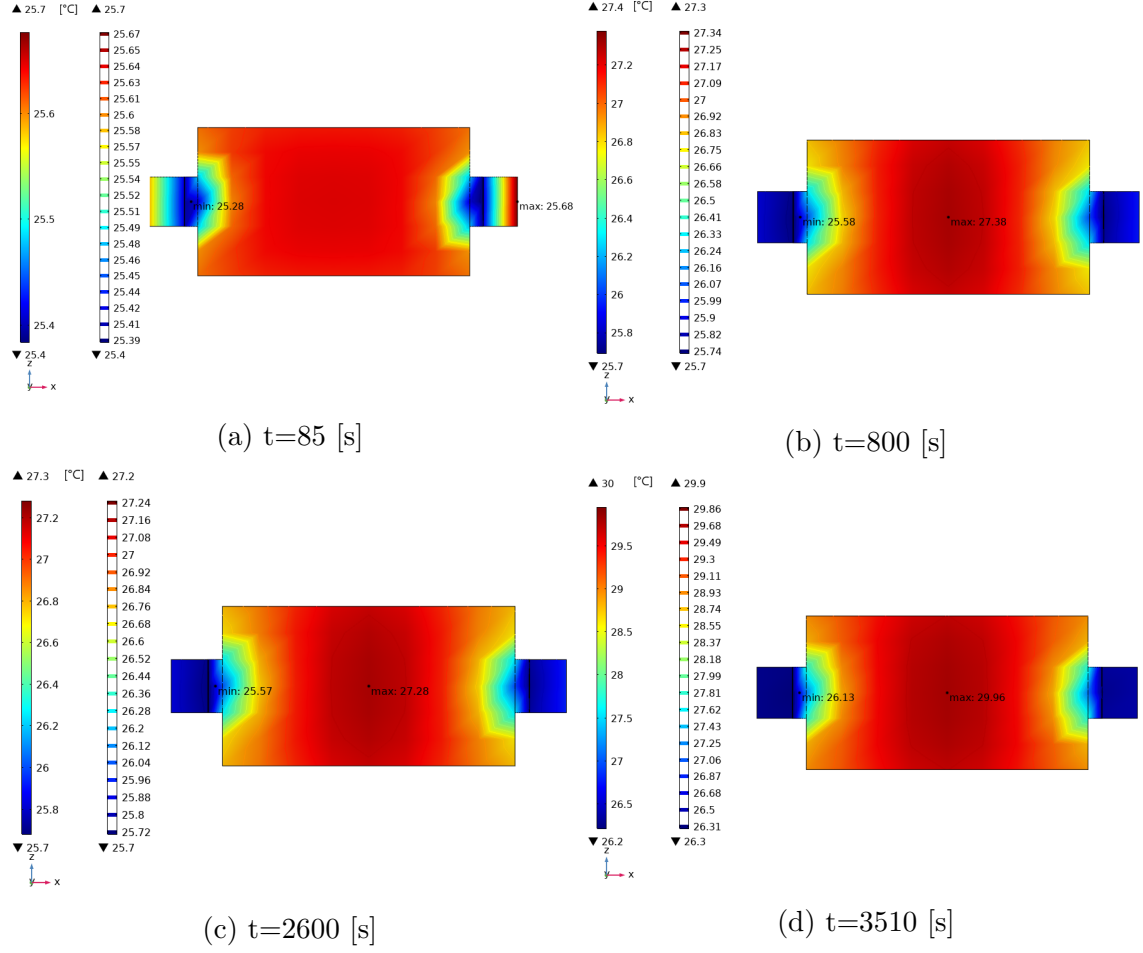


Figure 6.23: Surface temperature distribution, in the cell with repeated layers, under discharge at nominal C-rate and $h = 25$ [$W/(m^2K)$]

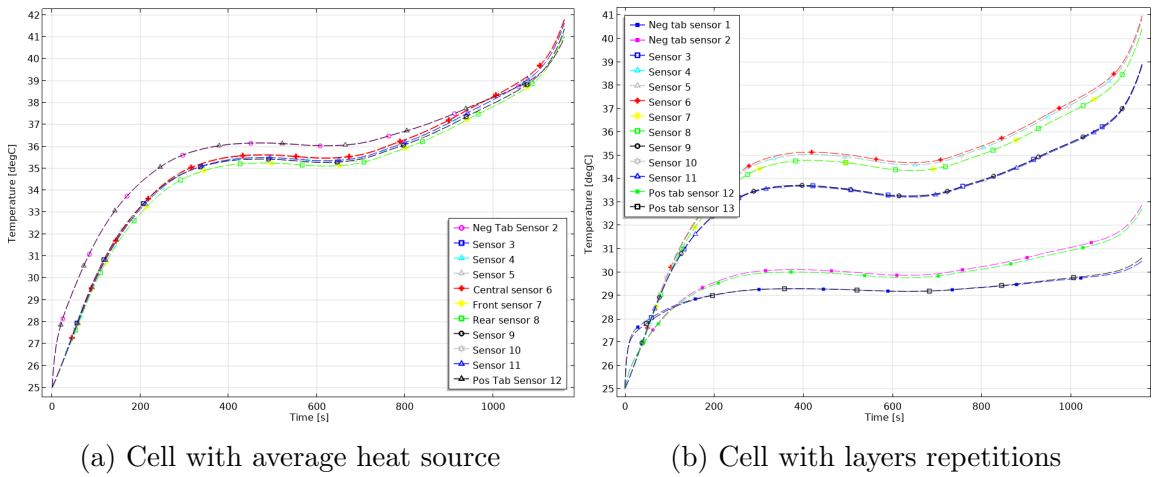


Figure 6.24: Temperature sensors readings through fast discharge and $h = 25$ [$W/(m^2K)$]

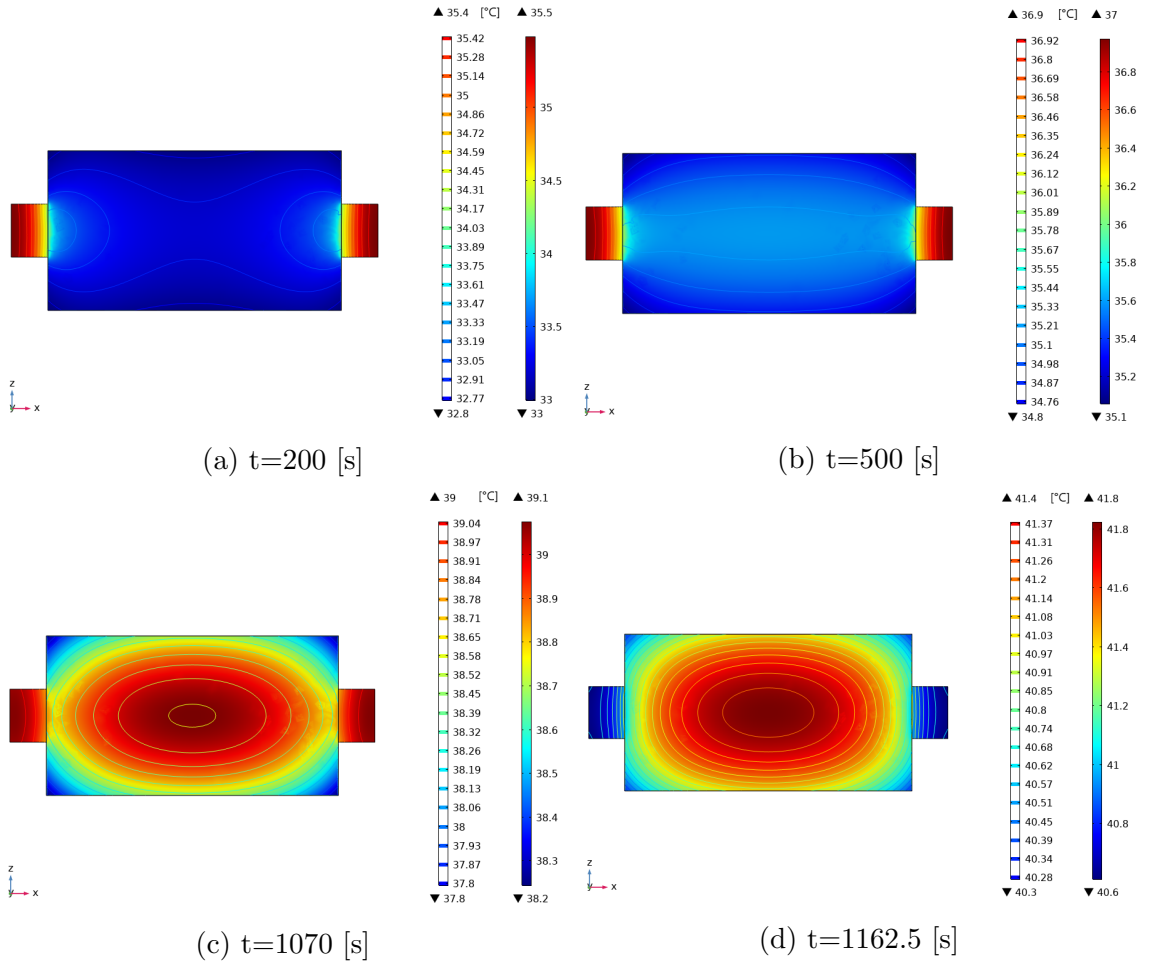


Figure 6.25: Central plane temperature distribution, in the cell with average heat source, during fast discharge and $h = 25$ [$W/(m^2K)$]

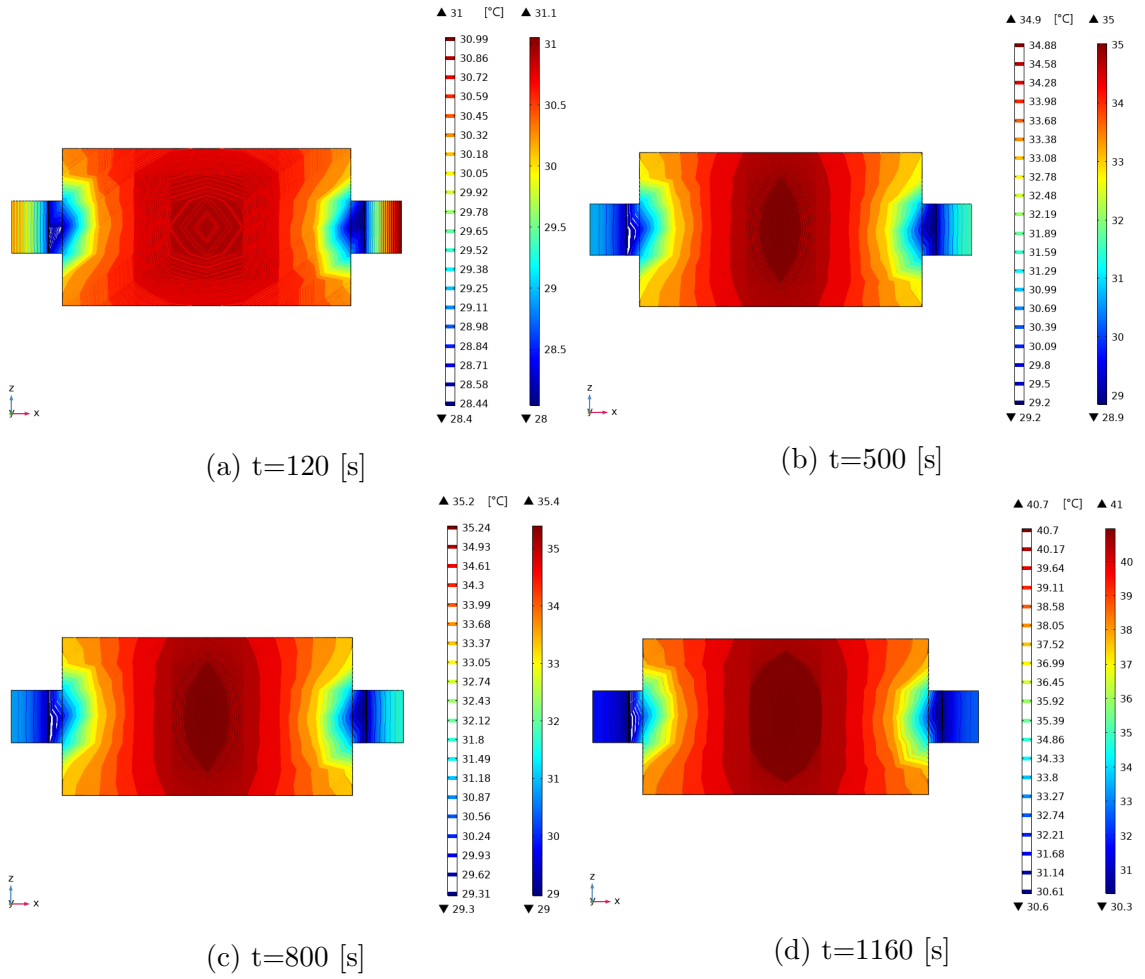


Figure 6.26: Central plane temperature distribution, in the cell with repeated layers, during fast discharge and $h = 25$ [$\text{W}/(\text{m}^2\text{K})$]

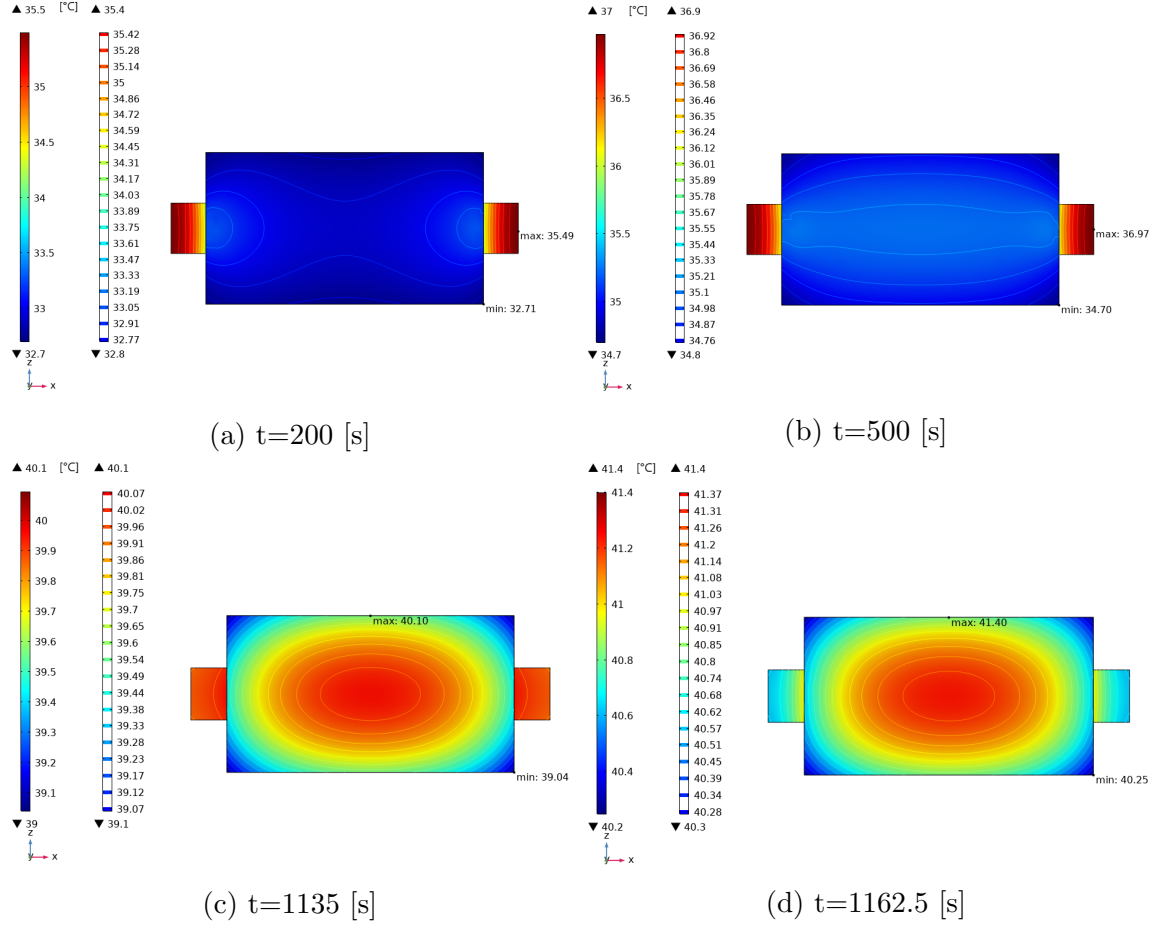


Figure 6.27: Surface temperature distribution, in the cell with average heat source, under fast discharge and $h = 25$ [$W/(m^2K)$]

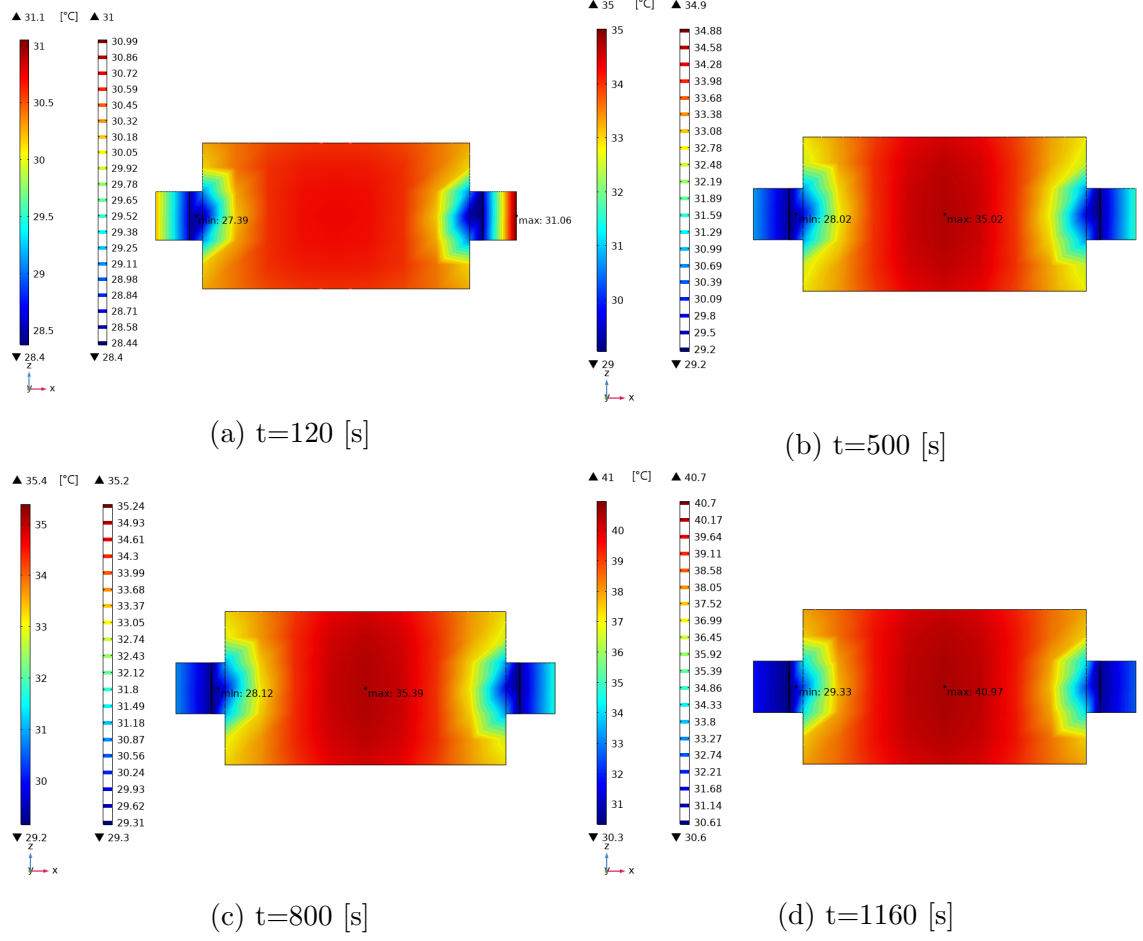


Figure 6.28: Surface temperature distribution, in the cell with repeated layers, under fast discharge and $h = 25$ [$W/(m^2K)$]

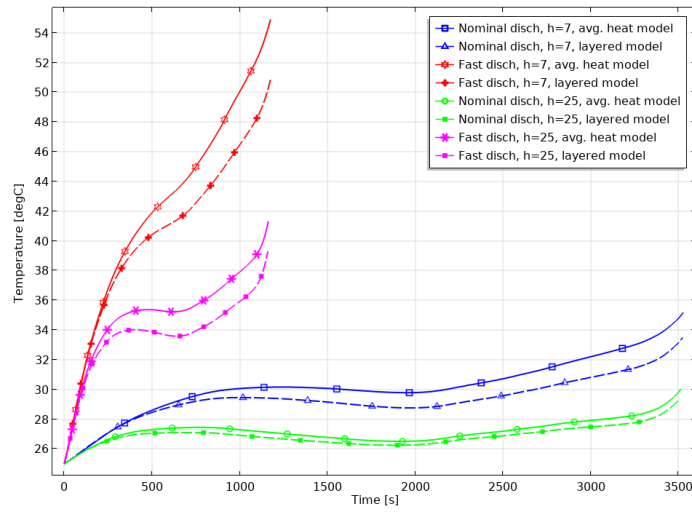


Figure 6.29: Average cell temperature comparison between the four cases and two models

Chapter 7

Concluding Remarks and Future Work

7.1 Summary and Conclusions

Li-ion batteries promise to be the main energy storage adopted in vehicle electrification, however their unique nature present several challenges that must be understood and solved. After the initial introduction, presenting main batteries electrochemical-thermal issues and the state-of-the-art technology, a fully coupled P2D electrochemical and 3D thermal model is developed for a high capacity Li-ion NMC cell for automotive applications. Next, the full parametrization is treated in Chapter 4, as well as practical insights to implement the model in COMSOL Multiphysics[®] v5.5. Missing parameters are obtained with good confidence from the literature or determined through analysis of the available data with mathematical means (Chapter 4). Different cell modelling approaches are presented starting from the constitutional fundamental unit analysis. Firstly, the electrochemical model is validated by itself with the data provided by an OEM showing good agreement under a range of three temperatures and four different applied C-rates. This confirms the goodness of the temperature dependency relations adopted for the most influencing parameters (Section 4.4). For the cell fundamental unit ECT analysis, the heat sources are compared and characterized between the simplified approach presented in this thesis and a full 3D electrochemical-thermal model of the same cell, developed for validation purposes, due to the lack of experimental data. The full 3D model offers the possibility to obtain 3D current and potential distribution as well as other electrochemical variables. These additional information helps the validation of the simplified model, which has

enough accuracy to capture correctly the uniform heat generation in each layer, required for an advanced BTMS design parameters effect. The last step is to analyze the thermal gradient and temperature rise of the complete cell under four different cases of electrical as well as thermal boundary conditions. The results of last models provide useful insights for thermal-electrochemical cell behavior and BTMS design.

The crucial concept that must be clear in mind is the need of capturing electrochemical and thermal nature of the battery together [50, 59, 118]. This study confirms its importance for a correct modelling of Li-ion batteries performance, especially for vehicular applications. Electrochemical nature is temperature sensitive, for example, temperature dependencies presented in Section 4.4, are not valid if the temperature goes near or below 0°C . The electrochemical model is heavily influenced by these quantities, especially: reaction rates constants, and diffusion coefficients. Hence, in developing an electrochemical model, the temperature dependency must be included. Although some adopted materials as well as some parameters were approximated, (especially OCP derivative curves), the electrochemical model is successfully validated with RMSE errors less than 0.1 in all tested situations within 10°C to 50°C temperature range. At low temperatures and higher rates, the model is correctly capturing the battery performance decay [24, 29, 50, 52] in terms of SOC utilization. It is in these conditions where modelling predictions experience higher errors.

Heat sources from non-isothermal analysis on cell fundamental unit models, (Chapter 6), shows that positive electrode is found to be the domain that is generating the highest volumetric heat source in the battery active material. This is caused in the most part by the reversible heat and mixing heat contribution of the cathode. This, underlines the importance of these contributions, which are often neglected in other studies [27, 30, 58]. The importance of reversible heat contribution can be seen in the negative electrode, as it causes the total heat generation of the domain to be endothermic, like found [29, 65, 144]. Outside the battery active area, the negative internal tab generates more than double the heat than the positive one. At high C-rates, irreversible heating (reaction and Ohmic heat) dominates the total heat generation.

Heat generation of current collectors is a term that needs attention in reproducing the cell thermal behavior. The useful comparison with the full 3D model points out that considering only one dimension for Ohmic heating, like for the battery tabs, is not enough for those domains. The difference in the heat sources computation is more than 4000 units, so missing that contributions could cause a wrong temperature evolution estimate. In development of similar models, the current collectors heat

generation must be carefully controlled.

In automotive application, this work remarks that is fundamental to have a battery BTMS. At rates higher than the nominal one the cell experiences temperature values higher than the optimal working range, and in some cases also close to the safety limits, 55°C in case B. When high capacity or high energy batteries are employed for EVs, it is strongly suggested to control the electrical-thermal parameters of the specific battery cells, modules and packs, to not jeopardize performances and life of all the components involved. One possible strategy is the forced air convection, tested in Chapter 6 on the single cell, this cooling technique allows to decrease the peak temperature by 14°C , from case B to case D. In addition, this causes slight temperature non-uniformity, which is the second most used criteria to evaluate good BTMS performances. Considerations at module and pack level need additional studies.

7.2 Future Work

This work produced an enabling scalable virtual engineering tool, namely a validated electrochemical-thermal model for future objective investigations on battery thermal performances and safety evaluations. Two different modelling approaches are presented, the average total heat source Li-ion battery, which is suitable for future battery packs studies and the layered model, which can be employed for specific aging or parametric studies on the single cell with a greater accuracy. Due to the case-specific data required, every cell is different from any other, by geometry, by chemistry and electrical parameters. However, this study provides a detailed procedure to solve this problem, which with the necessary changes, is adaptable for other cells. To complete the full ECT characterization on this specific high capacity NMC Li-battery some future work is required:

- Charge validation is an additional step to accurately reproduce the battery operation for automotive applications, since the energy storage device needs to be charged. It is important because as demonstrated by some studies [24, 29, 65], during charge instants Li-ion batteries can produce more heat than during discharge. This is due to variation of reversible heat contribution,
- Furthermore, sensibility study followed by an optimization can be implemented on the key electrochemical variables that regulate the Li-ion battery cell model and its temperature dependency, such as: diffusion coefficients, reaction rates

constants and initial SOC values as well geometry quantifies like particle radius and thicknesses,

- From the single cell, modules and the battery packs can be build. Then, their electrochemical-thermal performance can be studied applying current profile from a drive cycle simulation to thoroughly reproduce the vehicle on-board behavior,
- Simulations can also be used in static vehicle regimes such as a standing charge situation. Both dynamic and static simulations can be performed adding different cooling system solutions to evaluate the best design choice,
- Simulation of thermal runaway and capacity fade to obtain insight on the effects on the battery cell, modules and pack once the safety thresholds are not respected. Interesting insights can be retrieved to deeply understand this worst case scenario.

Bibliography

- [1] J. M. Tarascon and M. Armand, “Issues and challenges facing rechargeable lithium batteries,” in *Materials for sustainable energy: a collection of peer-reviewed research and review articles from Nature Publishing Group*. World Scientific, 2011, pp. 171–179.
- [2] “Panasonic NCR18650 B li-ion battery.” [Online]. Available: <https://blog.evandmore.com/lets-talk-about-the-panasonic-ncr18650b/>
- [3] “Panasonic prismatic li-ion battery for PHEVs.” [Online]. Available: <https://news.panasonic.com/global/topics/2011/7812.html>
- [4] “A123 systems pouch cell.” [Online]. Available: <http://www.a123systems.com/automotive/products/cells/>
- [5] “We’re going to need more lithium.” [Online]. Available: <https://www.bloomberg.com/graphics/2017-lithium-battery-future/>
- [6] R. Hausbrand, G. Cherkashinin, H. Ehrenberg, M. Gröting, K. Albe, C. Hess, and W. Jaegermann, “Fundamental degradation mechanisms of layered oxide li-ion battery cathode materials: Methodology, insights and novel approaches,” *Materials Science and Engineering: B*, vol. 192, pp. 3–25, 2015.
- [7] J. Garche, C. K. Dyer, P. T. Moseley, Z. Ogumi, D. A. Rand, and B. Scrosati, *Encyclopedia of electrochemical power sources*. Newnes, 2013, vol. 5.
- [8] I. Buchmann, *Batteries in a Portable World*, 4th ed. Cadex Electronics Inc., 2016.
- [9] J. Wang and X. Sun, “Understanding and recent development of carbon coating on LiFePO₄ cathode materials for lithium-ion batteries,” *Energy Environ. Sci.*, vol. 5, pp. 5163–5185, 01 2012.

- [10] Y. Xiao, L. Tongchao, J. Liu, L. He, J. Chen, J. Zhang, P. Luo, H. Lu, R. Wang, W. Zhu, Z. Hu, G. Teng, C. Xin, T. Liang, F. Wang, Y. Chen, Q. Huang, F. Pan, and H. Chen, "Insight into the origin of lithium/nickel ions exchange in layered $\text{Li}(\text{Ni}_x\text{Mn}_y\text{Co}_z)\text{O}_2$ cathode materials," *Nano Energy*, vol. 49, 04 2018.
- [11] Y. Yamada, Y. Iriyama, T. Abe, and Z. Ogumi, "Kinetics of lithium ion transfer at the interface between graphite and liquid electrolytes: Effects of solvent and surface film," *Langmuir : the ACS journal of surfaces and colloids*, vol. 25, pp. 12 766–70, 11 2009.
- [12] K. Mukai and I. Yamada, "High-pressure study of $\text{Li}[\text{Li}_{1/3}\text{Ti}_{5/3}]\text{O}_4$ spinel," *Inorganic Chemistry Frontiers*, vol. 5, 06 2018.
- [13] A. Pesaran, M. Keyser, G.-H. Kim, S. Santhanagopalan, and K. Smith, "Tools for designing thermal management of batteries in electric drive vehicles (presentation)," National Renewable Energy Lab.(NREL), Golden, CO (United States), Tech. Rep., 2013.
- [14] J. T. Warner, *The handbook of lithium-ion battery pack design: chemistry, components, types and terminology*. Elsevier, 2015.
- [15] "PCM enhanced battery pack." [Online]. Available: <https://www.allcelltech.com/>
- [16] "Toyota prius forced air cooling system." [Online]. Available: <http://synergyfiles.com/2016/07/battery-thermal-management-system-review/>
- [17] Z. Rao and S. Wang, "A review of power battery thermal energy management," *Renewable and Sustainable Energy Reviews*, vol. 15, no. 9, pp. 4554–4571, 2011.
- [18] "BEHR, thermal management for hybrid vehicles. technical press day," 2009. [Online]. Available: <https://www.yumpu.com/en/document/read/5806404/thermal-management-for-hybrid-vehicles-behr>
- [19] "Tesla model s battery pack teardown, copper motor via ricardo strategic consulting." [Online]. Available: <http://coppermotor.ppginteractive.com/2014/11/benchmarking-the-tesla-model-s-a-tour-of-ricardo-engineerings-teardown-laboratory/>
- [20] "GM volt inter-cell battery cooling plate." [Online]. Available: <https://gm-volt.com/2016/01/19/129946/>

- [21] R. Manimaran, K. Palaniradja, N. Alagumurthi, and J. Hussain, “Factors affecting the thermal performance of heat pipe—a review,” *Journal of Engineering Research and studies*, vol. 3, no. 2, pp. 20–4, 2012.
- [22] T.-H. Tran, S. Harmand, B. Desmet, and S. Filangi, “Experimental investigation on the feasibility of heat pipe cooling for HEV/EV lithium-ion battery,” *Applied Thermal Engineering*, vol. 63, no. 2, pp. 551–558, 2014.
- [23] Q. Wang, B. Jiang, B. Li, and Y. Yan, “A critical review of thermal management models and solutions of lithium-ion batteries for the development of pure electric vehicles,” *Renewable and Sustainable Energy Reviews*, vol. 64, pp. 106–128, 10 2016.
- [24] A. Maheshwari, “Modelling, aging and optimal operation of lithium-ion batteries,” Ph.D. dissertation, 2018.
- [25] T. F. Fuller, M. Doyle, and J. Newman, “Simulation and optimization of the dual lithium ion insertion cell,” *Journal of the Electrochemical Society*, vol. 141, no. 1, pp. 1–10, 1994.
- [26] S. Santhanagopalan, Q. Guo, P. Ramadass, and R. E. White, “Review of models for predicting the cycling performance of lithium ion batteries,” *Journal of power sources*, vol. 156, no. 2, pp. 620–628, 2006.
- [27] W. Gu and C. Wang, “Thermal-electrochemical modeling of battery systems,” *Journal of The Electrochemical Society*, vol. 147, no. 8, pp. 2910–2922, 2000.
- [28] J. Yi, U. S. Kim, C. B. Shin, T. Han, and S. Park, “Three-dimensional thermal modeling of a lithium-ion battery considering the combined effects of the electrical and thermal contact resistances between current collecting tab and lead wire,” *Journal of the Electrochemical Society*, vol. 160, no. 3, pp. A437–A443, 2013.
- [29] F. Bahiraei, “Thermal management of lithium-ion battery modules for electric vehicles,” 2017.
- [30] W. Fang, O. J. Kwon, and C.-Y. Wang, “Electrochemical–thermal modeling of automotive li-ion batteries and experimental validation using a three-electrode cell,” *International journal of energy research*, vol. 34, no. 2, pp. 107–115, 2010.

- [31] J. Li, Y. Cheng, L. Ai, M. Jia, S. Du, B. Yin, S. Woo, and H. Zhang, “3 D simulation on the internal distributed properties of lithium-ion battery with planar tabbed configuration,” *Journal of Power Sources*, vol. 293, pp. 993–1005, 2015.
- [32] C. C. Chan, “The state of the art of electric and hybrid vehicles,” *Proceedings of the IEEE*, vol. 90, no. 2, pp. 247–275, 2002.
- [33] B. Scrosati, J. Hassoun, and Y. Sun, “Lithium-ion batteries. a look into the future,” *Energy and Environmental Science*, vol. 4, no. 9, pp. 3287–3295, Sep. 2011.
- [34] K. C. Kam and M. M. Doeff, “Electrode materials for lithium ion batteries,” *Material Matters*, vol. 7, no. 4, pp. 56–60, 2012.
- [35] B. Scrosati, J. Garche, and W. Tillmetz, *Advances in battery technologies for electric vehicles*. Woodhead Publishing, 2015.
- [36] C. Hampel, “New battery, old price: updated renault zoe,” Jul 2019. [Online]. Available: <https://www.electrive.com/2019/07/01/new-battery-old-price-updated-renault-zoe-in-germany/>
- [37] U. S. Kim, J. Yi, C. B. Shin, T. Han, and S. Park, “Modeling the dependence of the discharge behavior of a lithium-ion battery on the environmental temperature,” *Journal of The Electrochemical Society*, vol. 158, no. 5, pp. A611–A618, 2011.
- [38] F. Leng, C. Tan, and M. Pecht, “Effect of temperature on the aging rate of Li-ion battery operating above room temperature,” *Scientific reports*, vol. 5, p. 12967, 08 2015.
- [39] M. Smart, B. Ratnakumar, J. Whitacre, L. Whitcanack, K. Chin, M. Rodriguez, and S. Surampudi, “The effect of high temperature exposure upon the performance of lithium ion cells,” in *Seventeenth Annual Battery Conference on Applications and Advances. Proceedings of Conference (Cat. No. 02TH8576)*. IEEE, 2002, pp. 53–58.
- [40] G. Ning, B. Haran, and B. Popov, “Capacity fade study of lithium-ion batteries at high discharge rates,” *Journal of Power Sources*, vol. 117, pp. 160–169, 05 2003.

- [41] A. A. Pesaran, A. Vlahinos, S. D. Burch *et al.*, *Thermal performance of EV and HEV battery modules and packs*. National Renewable Energy Laboratory, 1997.
- [42] X. Feng, M. Ouyang, X. Liu, L. Lu, Y. Xia, and X. He, “Thermal runaway mechanism of lithium ion battery for electric vehicles: A review,” *Energy Storage Materials*, vol. 10, 05 2017.
- [43] S. Zhang, K. Xu, and T. Jow, “The low temperature performance of Li-ion batteries,” *Journal of Power Sources*, vol. 115, no. 1, pp. 137–140, 2003.
- [44] C.-Y. Wang, G. Zhang, S. Ge, T. Xu, Y. Ji, X.-G. Yang, and Y. Leng, “Lithium-ion battery structure that self-heats at low temperatures,” *Nature*, vol. 529, no. 7587, pp. 515–518, 2016.
- [45] S. Basu, K. S. Hariharan, S. M. Kolake, T. Song, D. K. Sohn, and T. Yeo, “Coupled electrochemical thermal modelling of a novel Li-ion battery pack thermal management system,” *Applied Energy*, vol. 181, pp. 1–13, 2016.
- [46] B. Wu, V. Yufit, M. Marinescu, G. J. Offer, R. F. Martinez-Botas, and N. P. Brandon, “Coupled thermal–electrochemical modelling of uneven heat generation in lithium-ion battery packs,” *Journal of Power Sources*, vol. 243, pp. 544–554, 2013.
- [47] R. Sabbah, R. Kizilel, J. Selman, and S. Al-Hallaj, “Active (air-cooled) vs. passive (phase change material) thermal management of high power lithium-ion packs: Limitation of temperature rise and uniformity of temperature distribution,” *Journal of Power Sources*, vol. 182, no. 2, pp. 630–638, 2008.
- [48] M. W. Verbrugge, “Three-dimensional temperature and current distribution in a battery module,” *AIChE Journal*, vol. 41, no. 6, pp. 1550–1562, 1995.
- [49] R. Korthauer, *Lithium-ion batteries: basics and applications*. Springer, 2018.
- [50] M. Ghalkhani, “Thermal modeling and optimization of lithium-ion batteries for electric vehicles,” 2017.
- [51] Y. Lai, S. Du, L. Ai, L. Ai, Y. Cheng, Y. Tang, and M. Jia, “Insight into heat generation of lithium ion batteries based on the electrochemical-thermal model at high discharge rates,” *International Journal of Hydrogen Energy*, vol. 40, no. 38, pp. 13 039–13 049, 2015.

- [52] E. Hosseinzadeh, R. Genieser, D. Worwood, A. Barai, J. Marco, and P. Jennings, “A systematic approach for electrochemical-thermal modelling of a large format lithium-ion battery for electric vehicle application,” *Journal of power sources*, vol. 382, pp. 77–94, 2018.
- [53] N. Nitta, F. Wu, J. T. Lee, and G. Yushin, “Li-ion battery materials: present and future,” *Materials today*, vol. 18, no. 5, pp. 252–264, 2015.
- [54] T. Waldmann, M. Wilka, M. Kasper, M. Fleischhammer, and M. Wohlfahrt-Mehrens, “Temperature dependent ageing mechanisms in lithium-ion batteries – a post-mortem study,” *Journal of Power Sources*, vol. 262, p. 129–135, 09 2014.
- [55] I. Hong, B. Scrosati, and F. Croce, “Mesoporous, si/c composite anode for li battery obtained by ‘magnesium-thermal’ reduction process,” *Solid State Ionics*, vol. 232, pp. 24–28, 2013.
- [56] N. Mahmood, T. Tang, and Y. Hou, “Nanostructured anode materials for lithium ion batteries: progress, challenge and perspective,” *Advanced Energy Materials*, vol. 6, no. 17, p. 1600374, 2016.
- [57] X. Yao, B. Huang, J. Yin, G. Peng, Z. Huang, C. Gao, D. Liu, and X. Xu, “All-solid-state lithium batteries with inorganic solid electrolytes: Review of fundamental science,” *Chinese Physics B*, vol. 25, no. 1, p. 018802, jan 2016.
- [58] D. Bernardi, E. Pawlikowski, and J. Newman, “A general energy balance for battery systems,” *Journal of the electrochemical society*, vol. 132, no. 1, pp. 5–12, 1985.
- [59] G. L. Plett, *Battery management systems, Volume I: Battery modeling*. Artech House, 2015, vol. 1.
- [60] S. Nagpure, R. Dinwiddie, S. Babu, G. Rizzoni, B. Bhushan, and T. Frech, “Thermal diffusivity study of aged li-ion batteries using flash method,” *Journal of Power Sources*, vol. 195, pp. 872–876, 02 2010.
- [61] J. Belt, C. Ho, C. Motloch, T. Miller, and T. Duong, “A capacity and power fade study of li-ion cells during life cycle testing,” *Journal of Power Sources*, vol. 123, pp. 241–246, 09 2003.

- [62] T. Bandhauer, S. Garimella, and T. Fuller, “A critical review of thermal issues in lithium-ion batteries,” *Journal of The Electrochemical Society*, vol. 158, p. R1, 01 2011.
- [63] P. Ramadass, B. Haran, R. White, and B. N. Popov, “Capacity fade of sony 18650 cells cycled at elevated temperatures: Part II. capacity fade analysis,” *Journal of power sources*, vol. 112, no. 2, pp. 614–620, 2002.
- [64] E. Thomas, H. Case, D. Doughty, R. Jungst, G. Nagasubramanian, and E. Roth, “Accelerated power degradation of li-ion cells,” *Journal of Power Sources*, vol. 124, no. 1, pp. 254–260, 2003.
- [65] J. Marcicki and X. Yang, “Model-based estimation of reversible heat generation in lithium-ion cells,” *Journal of the Electrochemical Society*, vol. 161, pp. A1794–A1800, 08 2014.
- [66] D. Aurbach, “A review on new solutions, new measurements procedures and new materials for rechargeable li batteries,” *Journal of power sources*, vol. 146, no. 1-2, pp. 71–78, 2005.
- [67] J. Dahn, E. Fuller, M. Obrovac, and U. Von Sacken, “Thermal stability of Li_xCoO_2 , Li_xNiO_2 and $\lambda\text{-MnO}_2$ and consequences for the safety of Li-ion cells,” *Solid State Ionics*, vol. 69, no. 3-4, pp. 265–270, 1994.
- [68] C. D. Rahn and C.-Y. Wang, *Battery systems engineering*. John Wiley & Sons, 2013.
- [69] G. Nagasubramanian, “Electrical characteristics of 18650 Li-ion cells at low temperatures,” *Journal of applied electrochemistry*, vol. 31, no. 1, pp. 99–104, 2001.
- [70] N. Shidore and T. Bohn, “Evaluation of cold temperature performance of the JCS–VL 41 M PHEV battery using battery HIL,” SAE Technical Paper, Tech. Rep., 2008.
- [71] M. Smart, B. Ratnakumar, and S. Surampudi, “Electrolytes for low-temperature lithium batteries based on ternary mixtures of aliphatic carbonates,” *Journal of the Electrochemical Society*, vol. 146, no. 2, p. 486, 1999.
- [72] E. J. Plichta and W. K. Behl, “A low-temperature electrolyte for lithium and lithium-ion batteries,” *Journal of Power Sources*, vol. 88, no. 2, pp. 192–196, 2000.

- [73] C.-K. Huang, J. Sakamoto, J. Wolfenstine, and S. Surampudi, “The limits of low-temperature performance of Li-ion cells,” *Journal of the Electrochemical Society*, vol. 147, no. 8, p. 2893, 2000.
- [74] H.-P. Lin, D. Chua, M. Salomon, H. Shiao, M. Hendrickson, E. Plichta, and S. Slane, “Low-temperature behavior of Li-ion cells,” *Electrochemical and solid state letters*, vol. 4, no. 6, p. A71, 2001.
- [75] J. Fan and S. Tan, “Studies on charging lithium-ion cells at low temperatures,” *Journal of The Electrochemical Society*, vol. 153, no. 6, pp. A1081–A1092, 2006.
- [76] H. Liu, Z. Wei, W. He, and J. Zhao, “Thermal issues about Li-ion batteries and recent progress in battery thermal management systems: A review,” *Energy Conversion and Management*, vol. 150, pp. 304–330, 10 2017.
- [77] B. Wu, Z. Li, and J. Zhang, “Thermal design for the pouch-type large-format lithium-ion batteries I. thermo-electrical modeling and origins of temperature non-uniformity,” *Journal of The Electrochemical Society*, vol. 162, no. 1, pp. A181–A191, 2015.
- [78] C. Park and A. K. Jaura, “Dynamic thermal model of Li-ion battery for predictive behavior in hybrid and fuel cell vehicles,” SAE Technical Paper, Tech. Rep., 2003.
- [79] R. Spotnitz and J. Franklin, “Abuse behavior of high-power, lithium-ion cells,” *Journal of Power Sources*, vol. 113, pp. 81–100, 01 2003.
- [80] H. Yang, S. Amiruddin, H. Bang, Y.-K. Sun, and J. Prakash, “A review of Li-ion cell chemistries and their potential use in hybrid electric vehicles,” *Journal of Industrial and Engineering Chemistry*, vol. 12, pp. 12–38, 01 2006.
- [81] S. A. Hallaj, H. Maleki, J. Hong, and J. Selman, “Thermal modeling and design considerations of lithium-ion batteries,” *Journal of Power Sources*, vol. 83, no. 1, pp. 1 – 8, 1999.
- [82] G.-H. Kim, A. Pesaran, and R. Spotnitz, “A three-dimensional thermal abuse model for lithium-ion cells,” *Journal of Power Sources*, vol. 170, no. 2, pp. 476–489, 2007.
- [83] T. Cai, A. G. Stefanopoulou, and J. B. Siegel, “Modeling Li-ion battery thermal runaway using a three section thermal model,” in *Dynamic Systems and Control*

- Conference*, vol. 51906. American Society of Mechanical Engineers, 2018, p. V002T28A003.
- [84] A. A. Pesaran, “Battery thermal models for hybrid vehicle simulations,” *Journal of power sources*, vol. 110, no. 2, pp. 377–382, 2002.
 - [85] “Panasonic, notes and precautions,” 2008. [Online]. Available: <https://industrial.panasonic.com/cdbs/www-data/pdf/ACA4000/ACA4000PE1.pdf>
 - [86] F. Ladrech, “Battery thermal management for HEV & EV technology overview,” *Automotive Summit*, 2010.
 - [87] D. Andrea, *Battery management systems for large lithium ion battery packs*. Artech house, 2010.
 - [88] T. M. Bandhauer and S. Garimella, “Passive, internal thermal management system for batteries using microscale liquid–vapor phase change,” *Applied thermal engineering*, vol. 61, no. 2, pp. 756–769, 2013.
 - [89] Q. Wang, P. Ping, X. Zhao, G. Chu, J. Sun, and C. Chen, “Thermal runaway caused fire and explosion of lithium ion battery,” *Journal of Power Sources*, vol. 208, pp. 210–224, Jun. 2012.
 - [90] Z. Rao, S. Wang, and G. Zhang, “Simulation and experiment of thermal energy management with phase change material for ageing LiFePO₄ power battery,” *Energy Conversion and Management*, vol. 52, no. 12, pp. 3408–3414, 2011.
 - [91] S. A. Khateeb, M. M. Farid, J. R. Selmán, and S. Al-Hallaj, “Design and simulation of a lithium-ion battery with a phase change material thermal management system for an electric scooter,” *Journal of Power Sources*, vol. 128, no. 2, pp. 292–307, 2004.
 - [92] J. Yan, Q. Wang, K. Li, and J. Sun, “Numerical study on the thermal performance of a composite board in battery thermal management system,” *Applied Thermal Engineering*, vol. 106, pp. 131–140, 2016.
 - [93] M. Zolot, A. A. Pesaran, and M. Mihalic, “Thermal evaluation of toyota prius battery pack,” SAE Technical Paper, Tech. Rep., 2002.
 - [94] H. Hirano, T. Tajima, T. Hasegawa, T. Sekiguchi, and M. Uchino, “Boiling liquid battery cooling for electric vehicle,” in *2014 IEEE Conference and Expo*

- Transportation Electrification Asia-Pacific (ITEC Asia-Pacific)*. IEEE, 2014, pp. 1–4.
- [95] Z. An, L. Jia, X. Li, and Y. Ding, “Experimental investigation on lithium-ion battery thermal management based on flow boiling in mini-channel,” *Applied Thermal Engineering*, vol. 117, pp. 534–543, 2017.
 - [96] Z. Rao, S. Wang, M. Wu, Z. Lin, and F. Li, “Experimental investigation on thermal management of electric vehicle battery with heat pipe,” *Energy Conversion and Management*, vol. 65, pp. 92–97, 2013.
 - [97] A. Vlahinos and A. A. Pesaran, “Energy efficient battery heating in cold climates,” *SAE Transactions*, pp. 826–833, 2002.
 - [98] K. Leung and J. L. Budzien, “Ab initio molecular dynamics simulations of the initial stages of solid–electrolyte interphase formation on lithium ion battery graphitic anodes,” *Physical Chemistry Chemical Physics*, vol. 12, no. 25, pp. 6583–6586, 2010.
 - [99] S. Garofalini, “Molecular dynamics simulations of li transport between cathode crystals,” *Journal of power sources*, vol. 110, no. 2, pp. 412–415, 2002.
 - [100] B. Pattipati, C. Sankavaram, and K. Pattipati, “System identification and estimation framework for pivotal automotive battery management system characteristics,” *IEEE Transactions on Systems, Man, and Cybernetics, Part C (Applications and Reviews)*, vol. 41, no. 6, pp. 869–884, 2011.
 - [101] A. Fotouhi, D. J. Auger, K. Propp, S. Longo, and M. Wild, “A review on electric vehicle battery modelling: From lithium-ion toward lithium–sulphur,” *Renewable and Sustainable Energy Reviews*, vol. 56, pp. 1008–1021, 2016.
 - [102] H. He, R. Xiong, and J. Fan, “Evaluation of lithium-ion battery equivalent circuit models for state of charge estimation by an experimental approach,” *energies*, vol. 4, no. 4, pp. 582–598, 2011.
 - [103] Y. Hu, S. Yurkovich, Y. Guezennec, and B. Yurkovich, “Electro-thermal battery model identification for automotive applications,” *Journal of Power Sources*, vol. 196, no. 1, pp. 449–457, 2011.
 - [104] V. Ramadesigan, P. W. Northrop, S. De, S. Santhanagopalan, R. D. Braatz, and V. R. Subramanian, “Modeling and simulation of lithium-ion batteries from

- a systems engineering perspective,” *Journal of the electrochemical society*, vol. 159, no. 3, pp. R31–R45, 2012.
- [105] J. Newman and K. E. Thomas-Alyea, *Electrochemical systems*. John Wiley & Sons, 2012.
 - [106] J. Newman and W. Tiedemann, “Porous-electrode theory with battery applications,” *AIChE Journal*, vol. 21, no. 1, pp. 25–41, 1975.
 - [107] M. Doyle, T. F. Fuller, and J. Newman, “Modeling of galvanostatic charge and discharge of the lithium/polymer/insertion cell,” *Journal of the Electrochemical society*, vol. 140, no. 6, p. 1526, 1993.
 - [108] M. Doyle, J. Newman, A. S. Gozdz, C. N. Schmutz, and J.-M. Tarascon, “Comparison of modeling predictions with experimental data from plastic lithium ion cells,” *Journal of the Electrochemical Society*, vol. 143, no. 6, pp. 1890–1903, 1996.
 - [109] P. Ramadass, B. Haran, P. M. Gomadam, R. White, and B. N. Popov, “Development of first principles capacity fade model for Li-ion cells,” *Journal of the Electrochemical Society*, vol. 151, no. 2, pp. A196–A203, 2004.
 - [110] B. S. Haran, B. N. Popov, and R. E. White, “Theoretical analysis of metal hydride electrodes: studies on equilibrium potential and exchange current density,” *Journal of the electrochemical society*, vol. 145, no. 12, p. 4082, 1998.
 - [111] M. Guo, G. Sikha, and R. E. White, “Single-particle model for a lithium-ion cell: Thermal behavior,” *Journal of The Electrochemical Society*, vol. 158, no. 2, pp. A122–A132, 2011.
 - [112] W. Luo, C. Lyu, L. Wang, and L. Zhang, “A new extension of physics-based single particle model for higher charge–discharge rates,” *Journal of Power Sources*, vol. 241, pp. 295–310, 2013.
 - [113] S. K. Rahimian, S. Rayman, and R. E. White, “Extension of physics-based single particle model for higher charge–discharge rates,” *Journal of Power Sources*, vol. 224, pp. 180–194, 2013.
 - [114] C. R. Pals and J. Newman, “Thermal modeling of the lithium/polymer battery: I. discharge behavior of a single cell,” *Journal of the Electrochemical Society*, vol. 142, no. 10, p. 3274, 1995.

- [115] G. G. Botte, V. R. Subramanian, and R. E. White, “Mathematical modeling of secondary lithium batteries,” *Electrochimica Acta*, vol. 45, no. 15-16, pp. 2595–2609, 2000.
- [116] L. Rao and J. Newman, “Heat-generation rate and general energy balance for insertion battery systems,” *Journal of the Electrochemical Society*, vol. 144, no. 8, pp. 2697–2704, 1997.
- [117] L. Song and J. W. Evans, “Electrochemical-thermal model of lithium polymer batteries,” *Journal of the Electrochemical Society*, vol. 147, no. 6, p. 2086, 2000.
- [118] V. Srinivasan and C. Wang, “Analysis of electrochemical and thermal behavior of Li-ion cells,” *Journal of The Electrochemical Society*, vol. 150, no. 1, pp. A98–A106, 2003.
- [119] K. H. Kwon, C. B. Shin, T. H. Kang, and C.-S. Kim, “A two-dimensional modeling of a lithium-polymer battery,” *Journal of Power Sources*, vol. 163, no. 1, pp. 151–157, 2006.
- [120] U. S. Kim, C. B. Shin, and C.-S. Kim, “Effect of electrode configuration on the thermal behavior of a lithium-polymer battery,” *Journal of Power Sources*, vol. 180, no. 2, pp. 909–916, 2008.
- [121] ———, “Modeling for the scale-up of a lithium-ion polymer battery,” *Journal of Power Sources*, vol. 189, no. 1, pp. 841–846, 2009.
- [122] U. S. Kim, J. Yi, C. B. Shin, T. Han, and S. Park, “Modelling the thermal behaviour of a lithium-ion battery during charge,” *Journal of Power Sources*, vol. 196, no. 11, pp. 5115–5121, 2011.
- [123] W. Wu, X. Xiao, and X. Huang, “The effect of battery design parameters on heat generation and utilization in a Li-ion cell,” *Electrochimica Acta*, vol. 83, pp. 227–240, 2012.
- [124] K. S. Hariharan, P. Tagade, and S. Ramachandran, *Mathematical Modeling of Lithium Batteries: From Electrochemical Models to State Estimator Algorithms*. Springer, 2017.
- [125] J. Newman, “Thermoelectric effects in electrochemical systems,” *Industrial & engineering chemistry research*, vol. 34, no. 10, pp. 3208–3216, 1995.

- [126] B. Tjaden, S. J. Cooper, D. J. Brett, D. Kramer, and P. R. Shearing, “On the origin and application of the bruggeman correlation for analysing transport phenomena in electrochemical systems,” *Current opinion in chemical engineering*, vol. 12, pp. 44–51, 2016.
- [127] L. O. Valøen and J. N. Reimers, “Transport properties of LiPF₆-based Li-ion battery electrolytes,” *Journal of The Electrochemical Society*, vol. 152, no. 5, p. A882, 2005.
- [128] A. Khandelwal, K. S. Hariharan, V. S. Kumar, P. Gambhire, S. M. Kolake, D. Oh, and S. Doo, “Generalized moving boundary model for charge–discharge of LiFePO₄ / C cells,” *Journal of Power Sources*, vol. 248, pp. 101–114, 2014.
- [129] H. Ekström, “Electrode balancing of a lithium-ion battery with COMSOL[®],” *COMSOL BLOG*, 2019.
- [130] E. Bergman, “Designing thermal management systems for lithium-ion battery modules using COMSOL,” 2018.
- [131] A. Awarke, S. Pischinger, and J. Ogrzewalla, “Pseudo 3D modeling and analysis of the SEI growth distribution in large format Li-ion polymer pouch cells,” *Journal of the Electrochemical Society*, vol. 160, no. 1, p. A172, 2012.
- [132] A. Eddahech, O. Briat, and J.-M. Vinassa, “Thermal characterization of a high-power lithium-ion battery: Potentiometric and calorimetric measurement of entropy changes,” *Energy*, vol. 61, pp. 432–439, 2013.
- [133] A. Tourani, P. White, and P. Ivey, “A multi scale multi-dimensional thermo electrochemical modelling of high capacity lithium-ion cells,” *Journal of Power Sources*, vol. 255, pp. 360–367, 2014.
- [134] F. Richter, P. J. Vie, S. Kjelstrup, and O. S. Burheim, “Measurements of ageing and thermal conductivity in a secondary NMC-hard carbon Li-ion battery and the impact on internal temperature profiles,” *Electrochimica Acta*, vol. 250, pp. 228–237, 2017.
- [135] F. Richter, S. Kjelstrup, P. J. Vie, and O. S. Burheim, “Thermal conductivity and internal temperature profiles of Li-ion secondary batteries,” *Journal of Power Sources*, vol. 359, pp. 592–600, 2017.

- [136] “Targray NMC powder for battery manufacturers.” [Online]. Available: <https://www.targray.com/li-ion-battery/cathode-materials/nmc>
- [137] “Lithium nickel manganese cobalt oxide, $\text{LiNi}_{0.6}\text{Mn}_{0.2}\text{Co}_{0.2}\text{O}_2$ NMC 622 cathode powder, 500g.” [Online]. Available: <https://www.mseshop.com/products/lithium-nickel-manganese-cobalt-oxide-nmc622-cathode-powder?variant=7141237060>
- [138] J. Kim, H. Cho, H. Y. Jeong, H. Ma, J. Lee, J. Hwang, M. Park, and J. Cho, “Self-induced concentration gradient in nickel-rich cathodes by sacrificial polymeric bead clusters for high-energy lithium-ion batteries,” *Advanced Energy Materials*, vol. 7, no. 12, p. 1602559, 2017.
- [139] S. Chen, C. Wan, and Y. Wang, “Thermal analysis of lithium-ion batteries,” *Journal of power sources*, vol. 140, no. 1, pp. 111–124, 2005.
- [140] X. Liu, “Comprehensive calorimetry and modeling of the thermally-induced failure of a lithium ion battery,” Ph.D. dissertation, 2016.
- [141] A. Lidbeck and K. R. Syed, “Experimental characterization of Li-ion battery cells for thermal management in heavy duty hybrid applications,” *Göteborg, Sweden*, 2017.
- [142] D. H. Jeon and S. M. Baek, “Thermal modeling of cylindrical lithium ion battery during discharge cycle,” *Energy Conversion and Management*, vol. 52, no. 8-9, pp. 2973–2981, 2011.
- [143] S. Chacko and Y. M. Chung, “Thermal modelling of Li-ion polymer battery for electric vehicle drive cycles,” *Journal of Power Sources*, vol. 213, pp. 296–303, 2012.
- [144] R. Zhao, J. Gu, and J. Liu, “An investigation on the significance of reversible heat to the thermal behavior of lithium ion battery through simulations,” *Journal of Power Sources*, vol. 266, pp. 422–432, 2014.
- [145] S. Du, M. Jia, Y. Cheng, Y. Tang, H. Zhang, L. Ai, K. Zhang, and Y. Lai, “Study on the thermal behaviors of power lithium iron phosphate (LFP) aluminum-laminated battery with different tab configurations,” *International Journal of Thermal Sciences*, vol. 89, pp. 327–336, 2015.

- [146] S. Panchal, I. Dincer, M. Agelin-Chaab, R. Fraser, and M. Fowler, “Experimental and simulated temperature variations in a lifepo4-20 ah battery during discharge process,” *Applied Energy*, vol. 180, pp. 504–515, 2016.
- [147] C. Veth, D. Dragicevic, and C. Merten, “Thermal characterizations of a large-format lithium ion cell focused on high current discharges,” *Journal of Power Sources*, vol. 267, pp. 760–769, 2014.

Appendix A

Required Parameters For The COMSOL Multiphysics® Electrochemical-thermal Model

A.1 Model Global Parameters

Table A.1: Model Parameters

Property	Unit	Description
$r_{p,neg}$	$[m]$	Particle radius of negative electrode
$r_{p,pos}$	$[m]$	Particle radius of positive electrode
$L_{neg,cc}$	$[m]$	Length (Thickness) of negative electrode current collector and tab
L_{neg}	$[m]$	Length (Thickness) of negative electrode
L_{sep}	$[m]$	Length (Thickness) of separator

Continued on next page

Table A.1 – continued from previous page

Property	Unit	Description
L_{pos}	$[m]$	Length (Thickness) of positive electrode
$L_{pos,cc}$	$[m]$	Length (Thickness) of positive electrode current collector and tab
$L_{cell} = L_{neg,cc} + L_{neg} + L_{sep} + L_{pos} + L_{pos,cc}$	$[m]$	Cell (Thickness)
W_{cell}	$[m]$	Battery cell width
H_{cell}	$[m]$	Battery cell height
w_{tab}	$[m]$	Battery tab width
h_{tab}	$[m]$	Battery tab height
$x_{tab,neg} = 0$	$[m]$	Battery negative tab coordinate in x direction
$y_{tab,neg} = L_{neg,cc}$	$[m]$	Battery negative tab coordinate in y direction
$z_{tab,neg} = ((H_{cell}/2) - (h_{tab}/2))$	$[m]$	Battery negative tab coordinate in z direction
$x_{tab,pos} = W_{cell}$	$[m]$	Battery positive tab coordinate in x direction
$y_{tab,pos} = L_{pos,cc}$	$[m]$	Battery positive tab coordinate in y direction
$z_{tab,pos} = ((H_{cell}/2) - (h_{tab}/2))$	$[m]$	Battery positive tab coordinate in z direction

Continued on next page

Table A.1 – continued from previous page

Property	Unit	Description
N_{stacks}	$[-]$	Number of stacks (repetitions of the fundamental unit inside the battery cell)
$A_{cell} = W_{cell} \cdot H_{cell}$	$[m]$	Battery cell active cross sectional area
$\epsilon_{s,neg}$	$[-]$	Solid phase volume fraction of negative electrode
$\epsilon_{s,pos}$	$[-]$	Solid phase volume fraction of positive electrode
$\epsilon_{l,neg} = (1 - \epsilon_{s,neg})$	$[-]$	Electrolyte phase volume fraction of negative electrode (Porosity)
$\epsilon_{l,pos} = (1 - \epsilon_{s,pos} - 0.170)$	$[-]$	Electrolyte phase volume fraction of positive electrode (Porosity)
ϵ_{sep}	$[-]$	Electrolyte phase volume fraction of the separator (Porosity)
$b_{pos} = 1.5$	$[-]$	Bruggeman coefficient for tortuosity of positive electrode
$b_{sep} = 1.5$	$[-]$	Bruggeman coefficient for tortuosity of separator
$c_{s0,neg}$	$[mol/m^3]$	Initial Li-ion concentration of negative electrode

Continued on next page

Table A.1 – continued from previous page

Property	Unit	Description
$c_{s0,pos}$	$[mol/m^3]$	Initial Li-ion concentration of positive electrode
$c_{l,0}$	$[mol/m^3]$	Initial electrolyte salt Li-ion concentration
$c_{s,max,neg}$	$[mol/m^3]$	Maximum Li host capacity of negative electrode
$c_{s,max,pos}$	$[mol/m^3]$	Maximum Li host capacity of positive electrode
$SOC_{max,neg}$	$[-]$	Local SOC in negative electrode at 100% cell SOC
$SOC_{min,neg}$	$[-]$	Local SOC in negative electrode at 0% cell SOC
$SOC_{max,pos}$	$[-]$	Local SOC in positive electrode at 0% cell SOC
$SOC_{min,pos}$	$[-]$	Local SOC in positive electrode at 100% cell SOC
SOC_{start}	$[-]$	Initial cell SOC
SOC_{window}	$[-]$	Cell SOC State-of-charge window during simulation
$k_{0,neg}$	$[m/s]$	Reference reaction rate constant of negative electrode
$k_{0,pos}$	$[m/s]$	Reference reaction rate constant of positive electrode

Continued on next page

Table A.1 – continued from previous page

Property	Unit	Description
$E_{a,k,neg}$	$[J/mol]$	Reaction rate constant of negative electrode activation energy
$E_{a,k,pos}$	$[J/mol]$	Reaction rate constant of positive electrode activation energy
$Q_{cell} = W_{cell} \cdot h_{cell} \cdot L_{pos} \cdot c_{s,max,pos} \cdot \epsilon_{s,pos} \cdot F \cdot (SOC_{max,pos} - SOC_{min,pos})$	$[Ah]$	Cell capacity
$i_{1C} = Q_{cell}/(3600[s])$	$[A]$	Cell 1C current for this geometry
C_{rate}	$[A]$	C-rate during simulation
$i_{load} = i_{1C} \cdot C_{rate}$	$[A]$	Charge/discharge current
$cycle_{time} = 3600[s] \cdot SOC_{window}/C_{rate}$	$[s]$	Charge/discharge simulation time
$sim_{time} = (cycle_{time} + 200)$	$[s]$	Total simulation time
$K_{neg,cc}$	$[W/(mK)]$	Negative current collector thermal conductivity
K_{neg}	$[W/(mK)]$	Negative electrode thermal conductivity
K_{sep}	$[W/(mK)]$	Separator thermal conductivity
K_{pos}	$[W/(mK)]$	Positive electrode thermal conductivity

Continued on next page

Table A.1 – continued from previous page

Property	Unit	Description
$K_{pos,cc}$	$[W/(mK)]$	Positive current collector thermal conductivity
$K_{cell,\parallel}$	$[W/(mK)]$	In-plane cell thermal conductivity
$K_{cell,\perp}$	$[W/(mK)]$	Through-plane cell thermal conductivity
$\rho_{neg,cc}$	$[kg/m^3]$	Negative current collector density
ρ_{neg}	$[kg/m^3]$	Negative electrode thermal density
ρ_{sep}	$[kg/m^3]$	Separator density
ρ_{pos}	$[kg/m^3]$	Positive electrode density
$\rho_{pos,cc}$	$[kg/m^3]$	Positive current collector density
ρ_{cell}	$[kg/m^3]$	Cell density
$C_{p,neg,cc}$	$[J/kgK]$	Negative current collector heat capacity
$C_{p,neg}$	$[J/kgK]$	Negative electrode heat capacity
$C_{p,sep}$	$[J/kgK]$	Separator heat capacity
$C_{p,pos}$	$[J/kgK]$	Positive electrode heat capacity
$C_{p,pos,cc}$	$[J/kgK]$	Positive current collector heat capacity

Continued on next page

Table A.1 – continued from previous page

Property	Unit	Description
$C_{p,cell}$	$[J/kgK]$	Cell heat capacity
$T_{initial} = 298.15$	$[K]$	Initial temperature
$T_{ref} = 298.15$	$[K]$	Reference environment temperature
$R_{tab,neg} = \frac{1}{5.998 \cdot 10^7 [S/m]} \cdot \frac{w_{tab}}{(L_{neg,cc} \cdot h_{tab})}$	$[\Omega]$	Negative internal tab Ohmic resistance
$R_{tab,pos} = \frac{1}{3.774 \cdot 10^7 [S/m]} \cdot \frac{w_{tab}}{(L_{pos,cc} \cdot h_{tab})}$	$[\Omega]$	Positive internal tab Ohmic resistance
$R_{tab} = \frac{1}{3.774 \cdot 10^7 [S/m]} \cdot \frac{w_{tab}}{(L_{pos,cc} \cdot h_{tab})} \cdot \frac{w_{tab}}{(L_{neg,cc} \cdot h_{tab})}$	$[\Omega]$	Positive internal tab Ohmic resistance
$R_{c,tab,neg} = 3.73962 \cdot 10^{-5}$	$[\Omega]$	Negative internal tab contact resistance
$R_{c,tab,pos} = 2.97193 \cdot 10^{-5}$	$[\Omega]$	Positive internal tab contact resistance
$Vol_{tab,neg} = w_{tab} \cdot h_{tab} \cdot L_{neg,cc}$	$[m^3]$	Negative internal tab volume
$Vol_{tab,pos} = w_{tab} \cdot h_{tab} \cdot L_{pos,cc}$	$[m^3]$	Positive internal tab volume
h_{transf}	$[W/(m^2 \cdot K)]$	Simulations heat transfer coefficient

A.2 Local Variables of *Component one*

Table A.2: Local Variables of *Component one*

Variable	Unit	Description
$i_{app} = -i_{load} \cdot (rect1(t/(1[s])))$	[A]	Applied current to the battery cell
$K_{neg} = K_{0,neg} \exp\left(\frac{E_{act,K,neg}}{R} \left(\frac{1}{T_{ref}} - \frac{1}{(nojac(comp2.aveop7(comp2.T)))}\right)\right)$	[m/s]	Reaction rate constant of negative electrode
$K_{pos} = K_{0,pos} \exp\left(\frac{E_{act,K,pos}}{R} \left(\frac{1}{T_{ref}} - \frac{1}{(nojac(comp2.aveop7(comp2.T)))}\right)\right)$	[m/s]	Reaction rate constant of positive electrode
$i_{0,ref,neg} = K_{neg} \cdot F \cdot \frac{c_{s,max,neg}}{2}$	[A/m ²]	Reference exchange current density of negative electrode
$i_{0,ref,pos} = K_{pos} \cdot F \cdot \frac{c_{s,max,pos}}{2}$	[A/m ²]	Reference exchange current density of positive electrode
$Q_{cyclneg,load} = intop2((c_{s-surface} - soc_{min,neg} \cdot comp1.mat2.elpot.cEeqref) \cdot \epsilon_{s,neg} \cdot A_{cell}) \cdot F$	[C]	Cyclable charge in negative electrode, at load
$Q_{cyclpos,load} = intop4((c_{s-surface} - soc_{min,pos} \cdot comp1.mat3.elpot.cEeqref) \cdot \epsilon_{s,pos} \cdot A_{cell}) \cdot F$	[C]	Cyclable charge in positive electrode, at load
$SOC_{cell,load} = \frac{Q_{cyclneg,load}}{(Q_{cyclneg,load} + Q_{cyclpos,load})}$	[-]	Cell SOC State-of-charge of cell, at load

Continued on next page

Table A.2 – continued from previous page

Variable	Unit	Description
$Q_{Ohmic,neg} = -i_{s,x} \cdot \frac{\partial \phi_{s,x}}{\partial x} - i_{l,x} \cdot \frac{\partial \phi_{l,x}}{\partial x}$	$[W/m^3]$	Ohmic Heat of negative electrode
$Q_{Ohmic,pos} = -i_{s,x} \cdot \frac{\partial \phi_{s,x}}{\partial x} - i_{l,x} \cdot \frac{\partial \phi_{l,x}}{\partial x}$	$[W/m^3]$	Ohmic Heat of positive electrode
$Q_{Ohmic,sep} = -i_{l,x} \cdot \frac{\partial \phi_{l,x}}{\partial x}$	$[W/m^3]$	Ohmic Heat of separator
$Q_{Ohmic,neg,cc} = -i_{s,x} \cdot \frac{\partial \phi_{s,x}}{\partial x}$	$[W/m^3]$	Ohmic Heat of negative electrode current collector
$Q_{Ohmic,pos,cc} = -i_{s,x} \cdot \frac{\partial \phi_{s,x}}{\partial x}$	$[W/m^3]$	Ohmic Heat of positive electrode current collector

A.3 Local Variables of *Component two*

Table A.3: Local Variables of *Component two*

Variable	Unit	Description
$Q_{tot} = comp1.aveop6$ ($comp1.liion.Qh$)	$[W/m^3]$	Total Heat source from the battery model
$Q_{h,irrev,neg} = comp1.aveop2$ ($comp1.liion.Qirrevv_per1$)	$[W/m^3]$	Irreversible reaction heat source of negative electrode
$Q_{h,irrev,pos} = comp1.aveop4$ ($comp1.liion.Qirrevv_per1$)	$[W/m^3]$	Irreversible reaction heat source of positive electrode
$Q_{h,rev,neg} = comp1.aveop2$ ($comp1.liion.Qrevv_per1$)	$[W/m^3]$	Reversible reaction heat source of negative electrode

Continued on next page

Table A.3 – continued from previous page

Variable	Unit	Description
$Q_{h,rev,pos} = comp1.aveop4$ ($comp1.liion.Qrevv_per1$)	$[W/m^3]$	Reversible reaction heat source of positive electrode
$Q_{h,Ohmic,neg} =$ $comp1.aveop2(Q_{Ohmic,neg})$	$[W/m^3]$	Ohmic heat source of negative electrode
$Q_{h,Ohmic,pos} =$ $comp1.aveop4(Q_{Ohmic,pos})$	$[W/m^3]$	Ohmic heat source of positive electrode
$Q_{h,Ohmic,sep} =$ $comp1.aveop3(Q_{Ohmic,sep})$	$[W/m^3]$	Ohmic heat source of separator
$Q_{h,Ohmic,neg,cc} =$ $comp1.aveop1(Q_{Ohmic,neg,cc})$	$[W/m^3]$	Ohmic heat source of negative electrode current collector
$Q_{h,Ohmic,pos,cc} =$ $comp1.aveop5(Q_{Ohmic,pos,cc})$	$[W/m^3]$	Ohmic heat source of positive electrode current collector
$Q_{h,mix,neg} = comp1.aveop2$ ($comp1.liion.Qmix_tot_pce1$)	$[W/m^3]$	Mixing heat source of negative electrode
$Q_{h,mix,pos} = comp1.aveop4$ ($comp1.liion.Qmix_tot_pce2$)	$[W/m^3]$	Mixing heat source of positive electrode
$Q_{h,tab,neg} =$ $\frac{(R_{tab,neg} + R_{c,tab,neg}) \cdot (comp1.i_{app})^2}{Vol_{tab,neg}}$	$[W/m^3]$	Ohmic heat source of internal negative tab
$Q_{h,tab,pos} =$ $\frac{(R_{tab,pos} + R_{c,tab,pos}) \cdot (comp1.i_{app})^2}{Vol_{tab,pos}}$	$[W/m^3]$	Ohmic heat source of internal positive tab
$Q_{h,tab} =$ $\frac{(R_{tab} + R_{c,tab}) \cdot (comp1.i_{app})^2}{Vol_{tab}}$	$[W/m^3]$	Ohmic heat source of external tab

Vita Auctoris

NAME: Luigi Sacchetti
PLACE OF BIRTH: Borgomanero, Italy
YEAR OF BIRTH: 1996
EDUCATION: Liceo Scientifico, G. Ferrari, Borgosesisa, Italy, 2010-2015
Polytechnic of Turin, B.Sc., Turin, Italy, 2015-2018
Polytechnic of Turin, M.Sc., Turin, Italy, 2018-2020
University of Windsor, M.Sc., ON, Canada, 2019-2020